The Interplay of Waves and Stellar Evolution

Thesis by
Samantha C. Wu

In Partial Fulfillment of the Requirements for the
Degree of
Doctor of Philosophy

CALIFORNIA INSTITUTE OF TECHNOLOGY
Pasadena, California

2024
Defended May 2, 2024

Samantha C. Wu
ORCID: 0000-0003-2872-5153

ACKNOWLEDGMENTS

Thank you to my thesis committee–Konstantin, Phil, Mansi, and Sterl–for all the advice and time you have put in towards my Ph.D. progress. I have learned so much from all of you. Thank you to my advisor, Jim, for the scientific guidance; the research I worked on and learned about in your group was really interesting.

Thank you to Mansi for the support and thoughtful career advice; I gained so much from our conversations. Thank you to Evan Kirby for being an incredible educator, for the opportunity to guest lecture in your class, and for taking the time to talk with me and support me during difficult times. To Enrico: your support has always made astronomy and academia a much kinder and warmer place for me and so many others to exist in. I cannot express how much I appreciate you making time to talk me through difficult times and important decisions, to support my career wherever I am, and to express your faith in me. To all my past and present mentors, including Philipp Moesta and Eric Coughlin, thank you for all you have taught me.

Thank you to the Caltech staff who have been so helpful to me throughout my time here - JoAnn Boyd, Gita Patel, Mika Walton, Nam Ung, to name a few. Thank you to the CTLO/CPET, particularly Jenn Weaver and Jennifer Imamura, for sharing your dedication to and wisdom about pedagogy. Thank you to Cameron Hummels for directing an incredible outreach program and for the advice and inspiration. I am grateful to have worked alongside all my fellow GWIPMA o-comm members, past and present. Thank you especially to Ivey for being an amazing co-president. Thank you to the LAMAT REU and Caltech Connection for the opportunities to be a research mentor, and thank you to my wonderful mentees Rewa and Tuojin for being such wonderful people to work with.

Thanks to my cohort - Evan, Max, Sarah, Viraj, Yashvi, and Zhuyun - it's been great to spend grad school with you! Thanks to the grad students in my group, and the postdocs Daichi and Xiaoshan, for your support. Thank you to all my friends, both at and outside Caltech, for the laughs, deep talks, and good vibes. Special shout-out to the Treatment Sanctuary for all the fun times! Finally, I have experienced such a positive and supportive community with the astrograds. I appreciate you all!

Though words cannot express the depth of my gratitude to my parents, I will simply say thank you to my mother and father for the unconditional love and support that has eased my path in life immensely. To Henry, thank you for everything.

ABSTRACT

In this thesis, I study the evolution of stellar interiors and stellar oscillations in order to address current observational puzzles in astronomy. The thesis focuses on refining physical models for pre-supernova outbursts from massive stars, tidal evolution of planetary architectures, and progenitors of compact neutron star binaries. In order to research these topics, I combine calculations of internal stellar oscillation modes with stellar evolution models, to account for the evolution of the modes across the stars' lives. I begin by introducing some concepts in stellar evolution and internal stellar oscillations which underlie the physical intuition and models present throughout the thesis.

In the second chapter of the thesis, I present a study of tidal dissipation in M-dwarfs hosting nearby exoplanets. I model dynamical tides from normal modes of stellar oscillation across stellar evolution. With my novel methods, I am able to resolve the detailed spectrum of tidal dissipation as a function of stellar age. This empowers our evolutionary calculations to capture the resonance locking phenomenon, in which sustained tidal excitation of modes to large amplitudes over long intervals of stellar evolution produces enhanced dissipation. I find that Earth-mass and Jupiter-mass planets around M-dwarfs experience significant orbital migration under the influence of resonance locking with inertial modes of the star.

In the third and fourth chapters of the thesis, I explore the ability of waves generated by vigorous core convection in massive stars to impart heat to the stellar envelopes. I model the excitation and propagation of waves during phases of energetic nuclear burning in stars to assess the amount of energy that waves transmit to the envelope, as well as the timescale before core collapse when the majority of wave heating occurs. For the most promising models that exhibit elevated wave heating, I simulate the hydrodynamic response of the stellar envelope to wave heating. I find that wave heating is unlikely to independently produce very massive circumstellar material (CSM), but induces large expansion that could trigger interaction with a binary companion and thereby drive the intense mass loss that is expected to precede interacting supernovae.

The fifth chapter explores this very mechanism of binary interaction to produce pre-supernova outbursts. Even without wave heating, stripped stars can expand greatly in the years before core collapse simply as a consequence of stellar evolution. I employ

binary stellar evolution simulations to study how stripped stars with $M_{\rm He} \simeq 2$–$3\,M_{\odot}$ interact with neutron star companions, crucially focusing on the often-omitted stages from oxygen/neon (O/Ne) burning onward. I observe the stripped stars to undergo extremely high rates of mass loss, which can form a distribution of dense CSM around the system. My estimates for the CSM mass and radius are consistent with observed low ejecta-mass, interacting supernovae.

PUBLISHED CONTENT AND CONTRIBUTIONS

Wu, S. C., J. W. Dewberry, and J. Fuller (Mar. 2024). "Tidal Migration of Exoplanets around M Dwarfs: Frequency-dependent Tidal Dissipation". In: *The Astrophysical Journal* 963.1, p. 34. DOI: 10.3847/1538-4357/ad1e54.
S.C.W. participated in the conception of the project, ran the simulations, carried out the analysis, and wrote the majority of the manuscript.

Wu, S. C. and J. Fuller (Nov. 2022). "Extreme Mass Loss in Low-mass Type Ib/c Supernova Progenitors". In: *The Astrophysical Journal, Letters* 940.1, p. L27. DOI: 10.3847/2041-8213/ac9b3d.
S.C.W. participated in the conception of the project, ran the simulations, carried out the analysis, and wrote the majority of the manuscript.

Wu, S. C. and J. Fuller (May 2022). "Wave-driven Outbursts and Variability of Low-mass Supernova Progenitors". In: *The Astrophysical Journal* 930.2, p. 119. DOI: 10.3847/1538-4357/ac660c.
S.C.W. participated in the conception of the project, ran the simulations, carried out the analysis, and wrote the majority of the manuscript.

Wu, S. C. and J. Fuller (Jan. 2021). "A Diversity of Wave-driven Presupernova Outbursts". In: *The Astrophysical Journal* 906.1, p. 3. DOI: 10.3847/1538-4357/abc87c.
S.C.W. ran the simulations, carried out the analysis, and wrote the majority of the manuscript.

TABLE OF CONTENTS

LIST OF ILLUSTRATIONS

Number *Page*

LIST OF TABLES

Chapter 1

INTRODUCTION

1.1 Stellar evolution

The evolution of stars is well described by a set of four differential equations governing the interior structure of the star. By complementing these equations of stellar structure with an equation of state, along with the physics of gas opacity, nuclear reaction networks, and energy transport, state-of-the-art stellar evolution models can calculate the physical properties of stars from birth to death. Single-star evolution is quite well understood, such that numerical simulations of stars are quite competent at reproducing the characteristics of observed stellar populations (Hansen, Kawaler, and Trimble, 2004; Kippenhahn, Weigert, and Weiss, 2013). Through analysis of the equations of stellar structure, along with more detailed modeling, we can understand how properties including the mass, size, color, brightness, and surface abundances of stars are related to each other and change throughout the stellar lifetimes.

Stars with initial masses $M_{\rm init} \gtrsim 0.085\,M_\odot$ form by the collapse of large clouds of gas. They begin the zero-age main sequence (ZAMS) when they ignite hydrogen fusion in the core (Hansen, Kawaler, and Trimble, 2004; Kippenhahn, Weigert, and Weiss, 2013). Throughout the hydrogen burning phase, they remain on the main sequence, which spans a relatively tight correlation on the Hertzsprung-Russell (HR) diagram of luminosity versus effective temperature. In single-star evolution, a star's initial mass determines the size, temperature, and luminosity of the star, and thereby the location of the star on the HR diagram. Low-mass stars are dimmer, smaller, and cooler than higher-mass stars. The stellar mass also governs the age of the star, the internal energy transport mechanisms, and the types of nuclear reactions that occur within the star.

The majority of a star's life is spent fusing hydrogen into helium on the main sequence. This main sequence lifetime is briefer for massive stars, on the order of 10^6–10^8 yr for stars born with initial masses $M_{\rm init} \gtrsim 5\,M_\odot$ (Hansen, Kawaler, and Trimble, 2004; Kippenhahn, Weigert, and Weiss, 2013). Across stellar mass, the type of energy transport within stars also varies due to differences in opacity and nuclear burning rates. The envelopes of hot, massive stars with $M_{\rm init} \gtrsim 1.2\,M_\odot$ on

the main sequence have low internal opacities, allowing for radiation to transport the power. In the center of the star, fusion of hydrogen into helium via the CNO cycle is energetic enough to drive convection in the stellar core. After core hydrogen is exhausted at the end of the main sequence, the cores of these massive stars will contract until they are hot enough to fuse helium, with hydrogen burning in a surrounding shell. For the most massive stars, the cores repeat the cycle of contraction, thereby heating up the stellar center, followed by ignition of heavier elements once the cores are hot enough, which liberates enough energy to support the core against gravitational contraction.

For low-mass stars, their smaller luminosities extend their main sequence lifetimes, which can last longer than the age of the universe for stars $\lesssim 0.8\,M_\odot$ (Hansen, Kawaler, and Trimble, 2004; Kippenhahn, Weigert, and Weiss, 2013). Below $M_{\rm init} \lesssim 1.2\,M_\odot$, stars burn hydrogen via the pp-chain, which depends less steeply on the temperature than the CNO cycle. As a result, the cores of stars from $0.4\,M_\odot \lesssim M \lesssim 1.2\,M_\odot$ remain radiative. For these cooler stars, their lower temperatures increase the opacity and drive convection in the envelopes. After the main sequence, stars in this mass range ignite helium in degenerate cores in the helium flash, but never advance to further nuclear reactions. They end their lives with degenerate cores of carbon and oxygen. Below $M \lesssim 0.4\,M_\odot$, stars are even fully convective throughout their lives. Models of these lowest-mass stars indicate that they will not be able to contract to hot enough temperatures for helium fusion, so they are anticipated to end their lives as helium white dwarfs.

Stars of different masses traverse different paths and encounter a variety of fates throughout their post-main sequence evolution. Effectively single stars with $M_{\rm init} \lesssim$ 6–10 $M_\odot$ lose their envelopes in planetary nebulae and leave behind white dwarfs (Hansen, Kawaler, and Trimble, 2004; Kippenhahn, Weigert, and Weiss, 2013; Postnov and Yungelson, 2014). More massive stars will rapidly burn more massive elements until they build up an iron core. At this point, the core is composed of tightly bound iron nuclei, and fusing heavier elements is no longer energetically favorable - in fact, it would actually require extra energy input to the fusion reaction. The cores of these massive stars therefore proceed to collapse, with no hope of ignition to counterbalance the gravitational contraction. Many of these massive stars will die in core-collapse supernova explosions, leaving behind a neutron star remnant, or instead collapse directly into black holes for some of the most massive stars. Yet whether core collapse leads to a supernova (SN) or failed explosion, or

leaves behind a neutron star or black hole, appears not to be easily predicted from initial stellar mass. Instead, for single stars with $M_{\rm init} \gtrsim 12\,M_\odot$, both black holes and neutron stars can form from overlapping ranges of mass (Ebinger et al., 2019; Boccioli et al., 2023)

Stars are observed to rotate, with equatorial rotation velocities that appear to drop precipitously for main sequence stars $\lesssim 1.5\,M_\odot$ hosting thick convective envelopes (Kawaler, 1987; Agüeros et al., 2011). However, observations of young stellar clusters show that rotation periods are distributed uniformly across stellar mass (e.g., in the ONC, Rodríguez-Ledesma, Mundt, and Eislöffel, 2009), demonstrating a change in the rotation periods of young stars versus older stars. This may be attributed to the effect of magnetic braking, in which material leaving the star as a wind couples to the magnetic field of the star and carries away a large fraction of the star's rotational angular momentum. Though the stellar wind mass loss rate is small in low-mass stars, the lever arm of angular momentum loss extends quite far out to the Alfvén radius for the stellar magnetic field. This allows magnetic fields to amplify a star's loss of angular momentum, and stars which host strong magnetic fields will thereby be efficiently spun down by this magnetic braking phenomenon. Furthermore, it is thought that stars with vigorous envelope convection can produce internal magnetic fields through dynamo actions, e.g., stars $\lesssim 1.5\,M_\odot$. Thus these low-mass stars are likely to rotate slowly in the present, regardless of their initial rotation period. Some observations of stellar magnetic fields support this conjecture, finding that massive main sequence stars with only thin surface convective zones also exhibit weaker magnetic fields (Donati and Landstreet, 2009; Vidotto et al., 2014). Nevertheless, $M = 2$–$8\,M_\odot$ Ap and Bp stars exist with very thin surface convection zones, but also significant magnetic fields of 1–10kG (Moss, 2001; Mathys, 2001). Though rotation and magnetic fields remain challenging to model self-consistently in numerical stellar evolution codes, the effect of magnetic braking on stellar rotation across the stellar lifetime may be approximated via empirically calibrated prescriptions (Skumanich, 1972; Matt et al., 2015; El-Badry et al., 2022).

1.2 Stars influence their environments

Our physical understanding of single star evolution has been very successful in describing the majority of observed stars. However, the deviations from the norm invite us to consider a more detailed picture of stars' lives, in which stars do not exist in a vacuum. The frontiers of stellar astrophysics deal with the interactions of stars with their environments, which influences the evolution of the stars themselves

along with the lives of their companions.

Stellar companions

Most massive stars exist in binaries or multiples, and interactions with their companions via mass exchange dominate their evolution (Sana et al., 2012). The frequency of stellar companions increases from 0.5 ± 0.04 per solar-type MS primary star to 2.1 ± 0.3 per O-type MS primary star (Moe and Di Stefano, 2017).

Sana et al. (2012) find that around a third of massive stars are effectively single. Of the remaining interacting massive binaries, $\approx$ 25% will merge with their companion, $\approx$ 14% will accrete mass transferred from their companion or undergo common-envelope evolution, and a third will lose mass to their companion (Sana et al., 2012). Each of these channels of interaction have significant implications for the subsequent evolution of each binary companion, potentially giving rise to peculiar objects such as luminous blue variables and B[e] supergiants (Podsiadlowski, Joss, and Hsu, 1992; Justham, Podsiadlowski, and Vink, 2014; Podsiadlowski, Morris, and Ivanova, 2006; de Mink et al., 2014), or transient phenomena such as luminous red novae (Kasliwal et al., 2017; Metzger and Pejcha, 2017; Blagorodnova et al., 2017; MacLeod et al., 2017).

Binary interaction is primarily triggered when a star expands, eventually overfilling its Roche lobe so that it loses mass to its companion. This mass transfer has the potential to spin up the secondary star if it accretes the material, or remove angular momentum from the system if the mass loss is non-conservative. In more extreme cases, either the primary star expands so greatly or the orbital separation decreases rapidly enough that the primary star engulfs its companion. This describes the onset of a common-envelope event, in which the two stars spiral inside the shared envelope of the initial primary star towards a smaller orbital separation (Ivanova et al., 2013). If the envelope is ejected, the binary exits the common-envelope in a much tighter orbit; however, the inspiral may also proceed until the stars merge.

As the Roche lobe radius depends on orbital separation, the likelihood of binary interaction decreases with increasing orbital period. Massive stars are far more likely to have nearby companions, with the companion frequency peaking at $P_{\rm orb} \approx 3.5$ day (Moe and Di Stefano, 2017). For massive primary stars, companions residing at these short orbital periods are highly susceptible to interaction once the primary stars leave the main sequence and expand up to $\sim$ 100s of $R_{\odot}$.

Binary interactions that involve one or more phases of Roche lobe overflow can lead

to one or both stars being stripped of the hydrogen-rich envelope (Morton, 1960; Webbink, 1979; Tauris et al., 2017; Laplace et al., 2020). The resulting star is called a stripped star, or sometimes a helium star. The latter name refers to the star's helium envelope, which typically surrounds a compact carbon-oxygen core burning heavier elements. During core helium fusion, these stars remain compact; nevertheless, at late stages on relatively short timescales, stripped stars at certain masses can expand greatly (Habets, 1986; Dewi and Pols, 2003; Yoon, Woosley, and Langer, 2010; Laplace et al., 2020). This late expansion holds important consequences for mass loss in these binary systems, as well as their final fates as progenitors of hydrogen-deficient core collapse SNe and double neutron star systems that may become gravitational wave sources.

Mass loss and supernovae

Massive stars impart momentum and energy to their environments through strong stellar winds and their deaths as core-collapse supernovae (CCSNe), making them an important source of galactic feedback. Due to line opacity from heavy elements in the ultraviolet, these highly luminous stars exert strong radiation pressure that efficiently drives stellar winds with mass loss rates of $\dot{M} \sim 10^{-8}$–$10^{-6}\, M_\odot/\mathrm{yr}$ for $M_{\mathrm{ZAMS}} \sim 15$–$50\, M_\odot$ and velocities of $\gtrsim 10^3\,\mathrm{km/s}$ (Morton, 1967; Lucy and Solomon, 1970; Castor, Abbott, and Klein, 1975; Owocki, Castor, and Rybicki, 1988; Kudritzki and Puls, 2000). Over their $\sim 10^7$ yr main sequence lifetimes, these massive stars can lose a few–10% of the initial mass, or even over half of the initial mass for the most massive stars, which impacts their post-main sequence evolution (Morton, 1967; Hansen, Kawaler, and Trimble, 2004; Kippenhahn, Weigert, and Weiss, 2013). When these stars undergo core collapse, the explosions inject $\sim 10^{51}$ erg of kinetic energy and around a few–10 $M_\odot$ of ejecta into the surrounding interstellar medium (Postnov and Yungelson, 2014). Energetic outflows of material from massive stars throughout their lives and deaths not only provide momentum and energy feedback to galaxies, but also influence their chemical evolution.

Mass loss from massive stars and SNe have been found to relate in another unexpected way through recent advances in transient astronomy. As described in more detail in Chapter 3, many observations of CCSNe show evidence of the SN shock interacting with dense, slow-moving material near the exploding progenitor (see references in Wu and Fuller 2021; Wu and Fuller 2022b). These observations indicate that enhanced mass loss, many orders of magnitude larger than typical stellar winds, has occurred prior to the supernova. Interacting SNe have been observed across the

diversity of supernova types, from hydrogen poor to hydrogen rich, and the interactions vary greatly in duration and brightness as well (Smith, 2017). From early time spectra that capture flash-ionized emission lines in the circumstellar material (CSM), the chemical composition of the CSM has been inferred to be hydrogen rich in some cases; hydrogen poor, but helium rich in others; or even devoid of both hydrogen and helium, but displaying strong emission from other elements such as carbon (Pellegrino et al., 2022; Gal-Yam et al., 2022; Jacobson-Galán et al., 2024).

The prevalence of interacting SNe has increased as high-cadence surveys have captured more transients in the past decade, but typical non-interacting SNe remain the most commonly observed event (Perley et al., 2020). As a result, the mechanism underlying CSM production must be relatively rare, but occur for a wide range of progenitor masses and times before core collapse. Several explanations have been proposed to cause massive pre-SN outbursts, such as the pulsational pair instability (Moriya and Langer, 2015), unstable or explosive burning (Meakin and Arnett, 2006; Meakin and Arnett, 2007a; Arnett and Meakin, 2011; Woosley and Heger, 2015), binary interaction, or wave heating (Quataert and Shiode, 2012; Shiode and Quataert, 2014). Each of these theories for pre-SN outbursts suffers from some difficulties. For instance, pulsational pair instability excels at producing a family of long-duration, high-luminosity events, but it would only occur in a narrow range of very massive stars that are very rare among SN progenitors. The available energy budget of explosive nuclear burning is as yet unclear; similarly for the wave heating phenomenon, which can naturally explain the timing of pre-SN outbursts (Fuller, 2017; Fuller and Ro, 2018), uncertainties in the details of wave deposition and generation call into question whether waves are powerful enough to eject large CSM masses (Wu and Fuller, 2021; Wu and Fuller, 2022b). The varied scenarios that arise under the umbrella of binary interaction explain observed asymmetric CSM and span wide ranges in both progenitor and outburst properties, but currently very little of this parameter space has been explored.

Planetary companions

Evidence of stellar companions in the form of planets exists by virtue of our very own Solar System; around other stars, the number of known planets has grown to over 5500 as of the time of writing this thesis. With stellar hosts ranging from low-mass M-dwarfs, massive A stars, solar-type stars, evolved stars, and white dwarfs, among others, the copious data of discovered exoplanets lends itself to population-level studies of the evolution of star-planet systems. The observational biases of some the

most common methods for exoplanet detection, e.g., transits and RVs, preferentially discover planets nearby their host stars. In terms of size, the planets residing at these distances have been found to be similar to Earth, or even larger than Jupiter. In particular, one key genre of planet that does not exist in our own Solar System is the hot Jupiters, which are massive planets that orbit at short periods $\lesssim 10$ day. Due to the strong gravitational influence they exert at such small separations from their host stars, hot Jupiters are particularly prone to inducing reciprocal evolution between the planet and star via tides.

Tidal interactions play a significant role in the dynamics of many astrophysical systems, including our own Earth-Moon system. Consider a satellite orbiting a primary object, where the most relevant physical example here is a planet-star pair. The relative frequencies of the star's rotation and the planet's orbit give rise to a tidal frequency of the system. To first order, the gravitational potential of the planet applies a differential force across the perturbed star, giving rise to the hydrostatic response known as the equilibrium tide (first derived by Newton and Bernoulli; Zahn, 1966; Goldreich and Nicholson, 1989). This manifests as a tidal bulge and corresponds to the zero-frequency tidal response of the star. More precisely, the displacement of the fluid in the perturbed body requires wave-like corrections whenever the tidal frequency of the system is nonzero in a frame rotating with the star. This oscillatory component of the response is called the dynamical tide, which can be extremely important to the system's dynamics if the tidal frequency resonates with normal modes of oscillation within the star (a dynamic theory of tides was developed by Laplace in 1775; Press and Teukolsky, 1977; Goldreich and Nicholson, 1989; Witte and Savonije, 1999a; Witte and Savonije, 1999b; Ogilvie, 2014). Analogous to the harmonic oscillator, such resonances in the system enhance the tidal response of the star to large amplitudes which enable efficient transfer of energy and angular momentum between the orbit and the perturbed body.

In the example above, the tides were raised inside the star by the planet, which is likely to occur for close-in planets and their host stars. These tidal interactions can cause the planet to migrate inward or outward, and the star to spin more or less rapidly. Furthermore, tidal interactions where the planet is perturbed by the star have also been employed to explain formation of hot Jupiters. In the theory of high-eccentricity tidal migration, after planet-planet scattering or secular interactions drive the planet to a high-eccentricity orbit, strong tidal dissipation within the planet that is induced during close encounters at pericenter can circularize and shrink

the planet's orbit until it reaches day-long periods (Dawson and Johnson, 2018). Quantifying the impact that stars and planets have on each other's evolution via tides is crucial for understanding population-level patterns in exoplanet architectures, as well as the behavior of individual systems.

1.3 Stellar oscillations

The theory of stellar oscillations is rooted in the desire to understand observations of pulsating stars, including our own Sun. Periodic variations in the luminosity of stars have been established as arising from intrinsic oscillations of the star, as seen in Cepheids and other stars residing in the instability strip of the HR diagram (Hansen, Kawaler, and Trimble, 2004; Kippenhahn, Weigert, and Weiss, 2013; Christensen-Dalsgaard, 2016). For the Sun, surface fluctuations have revealed the presence of thousands of individual oscillation modes, which provide insights into the interior structure and differential rotation of the Sun (Schou et al., 1998). Though modes are far more difficult to observe in other stars, a rich spectrum of oscillations is expected to inherently exist within stars of any type, from M-dwarfs to white dwarfs. These modes are excited by various processes that perturb the fluid of the star out of equilibrium. For instance, the time-varying tidal potential of a satellite will excite stellar oscillations, and within the star, vigorous convective motions excite waves that can propagate throughout the star. Several chapters of this thesis rely on modeling stellar oscillations in order to address the theories of wave-heating to produce pre-SN outbursts and dynamical tidal dissipation in exoplanet systems.

The following subsections summarize the properties of some simple examples of waves, where generally the fluid is approximated as adiabatic and the perturbation to the gravitational potential is ignored (for more details, see Christensen-Dalsgaard 2003). Even in the complicated structures of real stars, internal stellar oscillations can usually be understood from a combination of these types of modes.

Gravity modes

An internal gravity wave arises in a layer of gas continuously stratified under gravity, leading to a hydrostatic equilibrium where gravity is balanced by the pressure gradient. Also known as g-modes, these low-frequency waves are restored by the buoyancy force. The dispersion relation for internal gravity waves is

$$\omega^2 = \frac{N^2}{1 + k_r^2/k_h^2} \tag{1.1}$$

where ω is the wave frequency, N^2 is the squared Brunt-Väisälä frequency, k_r is the radial wavenumber, and k_h is the horizontal wavenumber. The Brunt-Väisälä frequency depends on thermodynamic properties of the fluid,

$$N^2 = g\left(\frac{1}{\Gamma_1}\frac{\mathrm{d}\ln p}{\mathrm{d}r} - \frac{\mathrm{d}\ln\rho}{\mathrm{d}r}\right). \tag{1.2}$$

In stellar convective zones, $N^2 \leq 0$. Thus the g-mode frequency is imaginary in convective zones, such that g-modes only propagate in radiative regions of the star, with a maximum frequency of $|\omega| = |N|$.

Surface gravity waves are also restored by buoyancy, but occur at a discontinuity in density, such as at a free surface. Assuming incompressibility and that the fluid layer is infinitely deep, the dispersion relation is $\omega^2 = gk_h$. Here the wave frequency depends only on its wavelength and gravity.

Acoustic modes

For acoustic modes, also known as p-modes because they are restored by pressure, the equilibrium state is assumed to be spatially homogeneous. The dispersion relation comes out to $\omega^2 = c_s^2 |\mathbf{k}|^2$, where the wavevector is $\mathbf{k}$ and c_s is the sound speed. Though in a real star the background is not actually homogeneous with negligible gravity, the approximation is reasonable if the oscillations vary rapidly compared to the background. In stars, p-modes are relatively high-frequency waves.

Inertial modes

In the presence of rotation, stars can also host waves restored by the Coriolis force called inertial modes. When these modes are propagating in neutrally stratified regions, typically corresponding to convective zones in stars, the dispersion relation is

$$\omega^2 = \frac{4\Omega^2 k_z^2}{|\mathbf{k}|^2}, \tag{1.3}$$

where Ω is the angular rotation frequency of the star. Thus the frequencies are restricted to a maximum magnitude of $\omega \leq |2\Omega|$. In the presence of rotation and stable stratification, these waves propagate as so-called gravito-inertial modes. The gravito-inertial wave dispersion relation can be approximated by adding the right hand side (RHS) of Equation 1.1 to the RHS of Equation 1.3 (Mathis, 2009).

Modes of stellar oscillation

The general equations of linear stellar oscillation can be written down from linear perturbations to the Navier Stokes equations. Assuming adiabatic oscillations leads

to a system of ordinary differential equations for the displacement, pressure perturbation, and gravitational potential perturbation, along with the energy equation that expresses the density perturbation. The full equations may be viewed, e.g., in Christensen-Dalsgaard (2003). This system may be solved numerically with the appropriate boundary conditions, with the frequency ω as an eigenvalue of the problem. Each eigenvalue ω represents an oscillation mode, whose spatial variation is described by the corresponding eigenfunction. Each of these modes is a valid solution to the oscillation equations, so they may be excited by perturbations to the stellar fluid. However, each mode is excited to different amplitudes by different types of perturbations.

To qualitatively understand the wave behavior, we can analyze the modes in the highly simplified WKB limit, in which the radial order of the mode is assumed to be large. This is surprisingly applicable to many stellar oscillations, though here rotation too is ignored so this analysis does not account for inertial modes. Again neglecting the perturbation to the gravitational potential (called the Cowling approximation), the equations can be simplified to

$$\frac{\mathrm{d}^2\xi_r}{\mathrm{d}r} = \frac{\omega^2}{c_s^2}\left(1 - \frac{N^2}{\omega^2}\right)\left(\frac{L_\ell^2}{\omega^2} - 1\right)\xi_r. \tag{1.4}$$

Here L_ℓ is the Lamb frequency, $L_\ell^2 = \ell(\ell+1)c_s^2/r^2$. Then the radial wavenumber k_r obeys the following dispersion relation:

$$k_r^2 = \frac{\omega^2}{c_s^2}\left(\frac{N^2}{\omega^2} - 1\right)\left(\frac{L_\ell^2}{\omega^2} - 1\right). \tag{1.5}$$

When the radial wavenumber is real, the solution is oscillatory; when k_r^2 is negative, the solution is exponentially decaying. Both scenarios are described in more detail in Section 3. In brief, the solution oscillates when the frequency is large such that $\omega^2 > N^2, L_\ell^2$, corresponding to p-modes, or for small frequencies $\omega^2 < N^2, L_\ell^2$, which appear as g-modes. Since N^2 and L_ℓ^2 vary inside the star, there are regions where the p-modes and g-modes each cannot propagate. For instance, the p-modes are trapped in the envelopes of solar-type stars above an inner turning point, whereas g-modes are trapped in regions where $\omega^2 \lesssim N^2$ (as mentioned above, these are radiative zones).

1.4 Outline of thesis

The second chapter exemplifies the importance of modeling the interplay of waves and stellar evolution. By resolving the evolution of the spectrum of dynamical tidal

dissipation due to internal stellar oscillation modes over the lifetime of an M-dwarf star, we are able to capture the enhanced tidal dissipation and corresponding orbital migration that planets experience due to a phenomenon called resonance locking. Chapters 3 and 4 also constitute studies of waves within stars and how the wave properties change as the star evolves, this time in the context of oscillations excited in the cores of massive stars. These chapters examine whether convection-driven waves have the potential to deposit enough energy at the surface of supergiant and stripped-envelope stars to cause pre-supernova outbursts and explain interacting supernovae. In Chapter 5, I explore an alternate scenario for pre-supernova outbursts via binary interaction, which is triggered by remarkable expansion during the evolution of stripped stars.

Chapter 2

TIDAL MIGRATION OF EXOPLANETS AROUND M-DWARFS: FREQUENCY-DEPENDENT TIDAL DISSIPATION

Wu, S. C., J. W. Dewberry, and J. Fuller (Mar. 2024). "Tidal Migration of Exoplanets around M Dwarfs: Frequency-dependent Tidal Dissipation". In: *The Astrophysical Journal* 963.1, p. 34. DOI: 10.3847/1538-4357/ad1e54.

2.1 Abstract

The orbital architectures of short-period exoplanet systems are shaped by tidal dissipation in their host stars. For low-mass M-dwarfs whose dynamical tidal response comprises a dense spectrum of inertial modes at low frequencies, resolving the frequency dependence of tidal dissipation is crucial to capturing the effect of tides on planetary orbits throughout the evolutionary stages of the host star. We use non-perturbative spectral methods to calculate the normal mode oscillations of a fully convective M-dwarf modeled using realistic stellar profiles from MESA. We compute the dissipative tidal response composed of contributions from each mode as well as non-adiabatic coupling between the modes, which we find to be an essential component of the dissipative calculations. Using our results for dissipation, we then compute the evolution of circular, coplanar planetary orbits under the influence of tides in the host star. We find that orbital migration driven by resonance locking affects the orbits of Earth-mass planets at orbital periods $P_{\rm orb} \lesssim 1.5$ day and of Jupiter-mass planets at $P_{\rm orb} \lesssim 2.5$ day. Due to resonantly driven orbital decay and outward migration, we predict a dearth of small planets closer than $P_{\rm orb} \sim 1$ day and similarly sparse numbers of more massive planets out to $P_{\rm orb} \sim 3$ day.

2.2 Introduction

Through missions such as Kepler and TESS, thousands of exoplanets with a variety of sizes, masses, and orbital architectures have been discovered to date around stars of spectral types M through A. Due to the observational bias of both the transit and radial velocity methods, a large proportion of exoplanets are detected at short orbital periods, where their proximity to the host star can shape these planetary orbits through tidal effects. Tidal interactions may have modified the orbital inclinations, eccentricities, and semi-major axes across the history of these planetary systems.

In at least one case, tides are suspected to be acting in real time, as the orbit of exoplanet WASP-12b is measurably decaying from its current orbital period of $P_{\rm orb}$ = 1.09 day according to transit-timing analysis over the past decade (Maciejewski et al., 2013; Maciejewski et al., 2018; Patra et al., 2017; Yee et al., 2020). Due to the short decay timescale of ∼3 Myr, it is thought that the influence of the so-called dynamical tide in the late-F star host is accelerating the infall (Weinberg et al., 2017; Bailey and Goodman, 2019; Barker, 2020). In addition to the equilibrium tide (Zahn, 1966a), which represents the hydrostatic response of the star to its exoplanet perturber, the dynamical tide in the star is the oscillatory component of the response. Tidal dissipation within the star occurs as either the quasi-hydrostatic distortion of the equilibrium tide or The oscillation modes of the dynamical tide are damped due to local effects, such as turbulent viscosity in convective zones or radiative damping in stably stratified stellar regions. This process leads to an exchange of energy and angular momentum between the orbit and the stellar interior.

As the majority of stars in the galaxy are low-mass, the characteristics of M-dwarfs as planetary hosts are important for understanding the effects of tides in the most common exoplanet systems. Though the low luminosity of M-dwarfs makes them intrinsically more difficult to observe, short-period exoplanet systems around M-dwarfs are of interest as they are likely to be located in the habitable zone of the M-dwarfs (e.g., Trappist-1, Gillon et al., 2017) and are relatively easy to detect. Statistical analysis of exoplanet detections indicates that close-in exoplanets around M-dwarfs are much more abundant than around other spectral types, and they are also more likely to be small with $R \lesssim R_\oplus$ (Mulders, Pascucci, and Apai, 2015; Hsu, Ford, and Terrien, 2020; Dressing and Charbonneau, 2013; Ment and Charbonneau, 2023). With TESS already contributing dozens of exoplanets with measured masses and radii hosted by M-dwarfs and the Nancy Grace Roman Space Telescope anticipated to yield $\sim 10^3$ small planets around early- and mid-M-dwarfs (Tamburo, Muirhead, and Dressing, 2023), the plethora of observed systems will facilitate tests of theoretical predictions for how planetary architectures are shaped by effects such as tides.

Studies of tidal dissipation in low-mass stellar hosts have accounted for the influential contribution of the dynamical tide, which can provide orders of magnitude larger dissipation than the equilibrium tide (Ogilvie and Lin, 2007; Bolmont and Mathis, 2016). Many also follow how the strength of the tidal dissipation varies during the evolution of the star. In these low-mass stars ($M \lesssim 0.35\,M_\odot$) that are fully

convective during the pre-main sequence and the main sequence for $\sim 10^{11-12}$ yr, inertial modes (i-modes) excited in the stellar convective zone comprise the dynamical tide. Restored by the Coriolis force, i-modes propagate with rotating-frame frequencies $-2\Omega_s < \omega < 2\Omega_s$, where Ω_s is the stellar spin frequency, and may be damped by a convective turbulent viscosity. Stars containing radiative zones also experience dissipation due to radiative damping of internal gravity waves. At larger frequencies, the contribution from fundamental modes (f-modes), also described as surface gravity modes, constitutes the majority of the star's equilibrium tidal response.

Previous works have parameterized the strength of the dynamical tide due to i-modes as a function of the stellar properties in order to study the tidal dissipation across stellar evolution. In the simplest case of i-modes excited in a homogeneous envelope surrounding a rigid core with fractional radius α, averaging over the i-mode frequency range $-2\Omega_s < \omega < 2\Omega_s$ produces a dissipation rate that scales as α^5 and the dimensionless stellar rotation rate ϵ^2 (Goodman and Lackner, 2009; Ogilvie, 2013). With this formula for the dynamical tidal dissipation as a function of stellar properties, many studies have efficiently calculated the tidal dissipation coupled with stellar evolution (Mathis et al., 2016; Bolmont and Mathis, 2016; Gallet et al., 2017; Bolmont et al., 2017). However, the formula that is most commonly used in these works is of limited use for fully convective stars with realistic density profiles, as it predicts negligible tidal dissipation as the core size $\alpha \to 0$. In contrast, tidally excited inertial modes have actually been demonstrated to contribute significantly to the dynamical tide in rapidly rotating, coreless isentropic bodies (Wu, 2005a; Wu, 2005b; Ogilvie, 2013; Dewberry and Lai, 2022; Dewberry, 2023).

Furthermore, studies employing a frequency-averaged formalism do not account for the strong frequency dependence of the dynamical tidal response, which exhibits large peaks associated with resonances with the inertial modes (Ogilvie and Lin, 2007; Ogilvie, 2013). Ignoring the frequency dependence of tidal dissipation also entails the drawback that no resonance locking can be resolved in these systems. During resonance locking, the enhanced response resulting from tidal excitation of resonant modes persists over a significant period of the stellar lifetime. This mechanism has therefore been invoked to explain faster than expected orbital migration and circularization in stellar binaries and planet-moon systems (Witte and Savonije, 1999; Fuller and Lai, 2012; Fuller, Luan, and Quataert, 2016). In order to capture the amplified response near mode resonances, the tidal dissipation as a

function of frequency must be calculated throughout the stellar evolution. For convective stars, resonance locking is of particular interest since the frequency range of i-modes coincides with the tidal forcing frequencies of most planetary companions. Thus, planetary orbits will have many opportunities to encounter resonances with the capacity to shape orbital architectures through strong tidal dissipation.

In this work, we perform frequency-dependent calculations of tidal dissipation, coupled with the stellar evolution of a $M = 0.2\,M_\odot$ M-dwarf which is fully convective on the pre-main sequence (PMS) and main sequence (MS). This procedure is repeated for models with different initial rotation periods, allowing us to capture the diversity in outcomes that ensue by varying this initial condition. Using an expansion over the normal modes of stellar oscillation, we compute the dissipative response of the star, thereby resolving the resonant frequencies coinciding with inertial mode (i-mode) and fundamental mode (f-mode) frequencies as a function of stellar age. We use our results to calculate the orbital migration of Earth-mass and Jupiter-mass planets, initialized at a range of ages to represent a few possible formation pathways, and find that resonance locking dominates the migration of planets within $\sim$ 1–2 day orbits. Section 2.3 describes how we set up our calculations of the tidal dissipation, normal mode eigenfunctions, and orbital evolution; Section 2.4 demonstrates the dissipative response of the star across its evolution, noting how our approach compares to other methods; and Section 2.5 shows the associated orbital migration due to tides. We discuss the observational implications for exoplanet demographics and the uncertainties in our implementation of the tidal response in Section 2.6.

2.3 Methods

Tidal formalism

We consider circular, coplanar orbits of a satellite of mass M' at a separation a from a body of mass M, which rotates at a spin frequency Ω_s. The satellite orbital frequency is $\Omega_o = [G(M + M')/a^3]^{1/2}$. In a frame centered on and rotating with the body of mass M which experiences the tidal disturbance, the tidal potential of the satellite can be written as

$$U = \sum_{\ell=2}^{\infty} \sum_{m=-\ell}^{\ell} U_{\ell m} r^\ell Y_\ell^m(\theta, \phi) \exp[-\mathrm{i}\omega_m t], \tag{2.1}$$

where

$$\omega_m = m(\Omega_o - \Omega_s), \tag{2.2}$$

$$U_{\ell m} = -\left(\frac{GM'}{a^{l+1}}\right)\left(\frac{4\pi}{2\ell+1}\right) Y_\ell^{m*}(\pi/2, 0). \tag{2.3}$$

From here onward, we refer to the perturbed body M as a star, and the satellite M' as a planet. The linearized momentum equation for Lagrangian displacement $\boldsymbol{\xi}$ in the star's rotating frame of reference is

$$\frac{\partial^2 \boldsymbol{\xi}}{\partial t^2} + 2\Omega_s \times \frac{\partial \boldsymbol{\xi}}{\partial t} + C[\boldsymbol{\xi}] = -\nabla U, \tag{2.4}$$

where C is a self-adjoint operator describing internal fluid forces. The normal modes of the star are $\hat{\boldsymbol{\xi}}_\alpha = \boldsymbol{\xi}_\alpha(r)\exp[-\mathrm{i}\omega_\alpha t]$. For a rotating fluid, the normal modes satisfy the following conditions (in units of $G = M = R = 1$, where M and R are the stellar mass and radius, respectively):

$$-\omega_\alpha^2 \boldsymbol{\xi}_\beta - 2\mathrm{i}\omega_\alpha \Omega_s \times \boldsymbol{\xi}_\alpha + \mathbf{C}[\boldsymbol{\xi}_\alpha] = 0, \tag{2.5}$$

$$(\omega_\alpha + \omega_\beta)\langle \boldsymbol{\xi}_\alpha, \boldsymbol{\xi}_\beta \rangle + \langle \boldsymbol{\xi}_\alpha, 2\mathrm{i}\Omega \times \boldsymbol{\xi}_\beta \rangle = 0, \text{ for } \beta \neq \alpha, \tag{2.6}$$

$$\langle \boldsymbol{\xi}_\alpha, \boldsymbol{\xi}_\alpha \rangle = 1, \tag{2.7}$$

where $\langle\ ,\ \rangle$ is the inner product such that

$$\langle \boldsymbol{\xi}_\alpha, \boldsymbol{\xi}_\beta \rangle = \int_V \rho_0 \boldsymbol{\xi}_\alpha^* \cdot \boldsymbol{\xi}_\beta \mathrm{d}V. \tag{2.8}$$

Assuming a phase space expansion of the tidal response in terms of normal modes of stellar oscillation, it can be shown (e.g., Schenk et al. 2001; Lai and Wu 2006) that the amplitude of oscillation mode α forced by the tidal potential in the absence of dissipation satisfies

$$\dot{c}_\alpha + \mathrm{i}\omega_\alpha c_\alpha = -\frac{\mathrm{i}}{2\epsilon_\alpha}\exp[-\mathrm{i}\omega_m t]\sum_\ell U_{\ell m} Q_{\ell m}^\alpha, \tag{2.9}$$

where $\epsilon_\alpha = \omega_\alpha \langle \boldsymbol{\xi}_\alpha, \boldsymbol{\xi}_\alpha \rangle + \langle \boldsymbol{\xi}_\alpha, \mathrm{i}\Omega_s \times \boldsymbol{\xi}_\alpha \rangle$ and

$$Q_{\ell m}^\alpha = \langle \boldsymbol{\xi}_\alpha, \nabla(r^\ell Y_\ell^m) \rangle = -\frac{(2\ell+1)}{4\pi}\Phi_{\ell\alpha} \tag{2.10}$$

is the tidal overlap coefficient for mode α. In this work, we will consider the effect of forcing by one tidal potential $U_{\ell m}$ at a time. Stationary solutions with $\dot{c}_\alpha = -\mathrm{i}\omega_m c_\alpha$ for each mode α are then

$$\begin{aligned} c_\alpha^\ell(t) &= -\frac{\exp[-\mathrm{i}\omega_m t]}{2\epsilon_\alpha(\omega_\alpha - \omega_m)} U_{\ell m} Q_{\ell m}^\alpha \\ &:= \hat{c}_\alpha^\ell(\omega_m)\exp[-\mathrm{i}\omega_m t]. \end{aligned} \tag{2.11}$$

In the quasi-adiabatic formalism (e.g., Kumar, Ao, and Quataert, 1995; Burkart et al., 2012), we can write the individual mode damping rates γ_α due to viscous damping as (e.g., Ipser and Lindblom, 1991) $\gamma_\alpha = I_{\alpha\alpha}/(\omega_\alpha \epsilon_\alpha)$, where

$$I_{\alpha\beta} = \int_V \mu(\delta S_\alpha^* : \delta S_\beta) \mathrm{d}V, \tag{2.12}$$

where : indicates contraction along both indices of rank-2 tensors. Here $\mu = \rho\nu$ is the dynamic viscosity given density ρ and kinematic viscosity ν, and

$$\delta S_\alpha = \frac{1}{2}\left[\nabla v_\alpha + (\nabla v_\alpha)^T - \frac{2}{3}(\nabla \cdot v_\alpha) I\right] \tag{2.13}$$

is the shear tensor for mode α with velocity eigenfunction $v_\alpha = -\mathrm{i}\omega_\alpha \boldsymbol{\xi}_\alpha$. This normalizes the viscous dissipation rate $I_{\alpha\alpha}$ by the total energy of the mode α (Vick and Lai, 2020).

In general, the time-averaged dissipation rate due to viscous dissipation of the tide is

$$D = \int_V \mu(\delta S^* : \delta S) \mathrm{d}V, \tag{2.14}$$

where the total shear tensor δS is given by

$$\delta S = \frac{1}{2}\left[\nabla v + (\nabla v)^T - \frac{2}{3}(\nabla \cdot v) I\right]. \tag{2.15}$$

Here the velocity fields v constitute the sum of contributions from the normal modes of stellar oscillation:

$$v = \sum_\alpha \hat{c}_\alpha^\ell v_\alpha = -\sum_\alpha \frac{\omega_m}{\omega_\alpha} \frac{U_{\ell m} Q_{\ell m}^\alpha}{2\epsilon_\alpha(\omega_\alpha - \omega_m - i\gamma_\alpha)} v_\alpha. \tag{2.16}$$

Above, we have modified the mode amplitudes $\hat{c}_\alpha^\ell$ defined in Equation 2.11 to include the individual mode damping rates γ_α.

An important quantifier of the frequency-dependent tidal response in the perturbed body is the potential Love number $k_{\ell m}^n(\omega_m)$, which is a dimensionless, complex number. In this notation, for given azimuthal wavenumber m, the Love number describes the effect of an isolated tidal potential of harmonic degree n on the gravitational response of harmonic degree ℓ, at each tidal frequency ω_m. Note that in a spherically symmetric calculation, $k_{\ell m}^n = 0$ for $\ell \neq n$. The imaginary part of

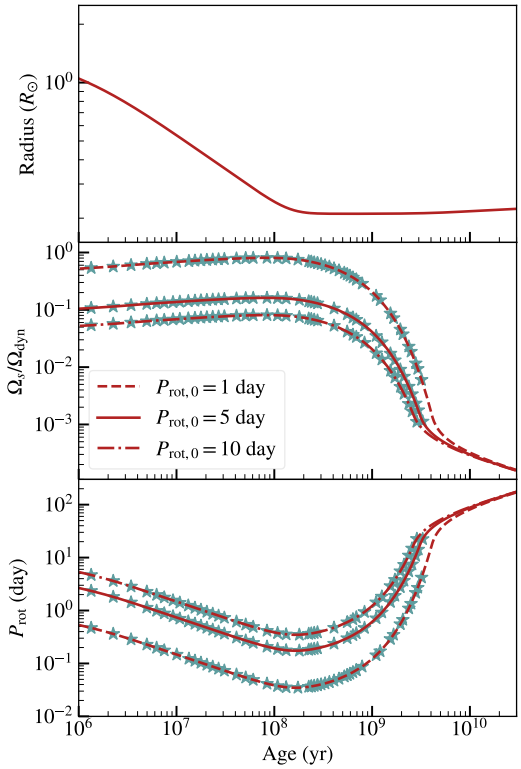

Figure 2.1: Evolution of the stellar radius (top panel), stellar spin frequency in units of the dynamical frequency $\Omega_{\rm dyn} = (GM/R^3)^{1/3}$ (middle panel), and stellar rotation period (bottom panel) with stellar age for the 0.2 $M_\odot$ stellar model used in this work. Different initial rotation periods $P_{\rm rot,0}$ of 1, 5, and 10 day are shown with the linestyles indicated in the legend; the radius evolution is the same for all three initial conditions. Blue stars indicate the stellar profiles used to calculate normal modes of oscillation and construct the grid of dissipation for each $P_{\rm rot,0}$.

the Love number where $\ell = n$ is related to the energy dissipation rate D by (Ogilvie, 2013)

$$\begin{aligned} D &= \frac{(2\ell+1)}{8\pi G} R|U_{\ell m}|^2 \omega_m \mathrm{Im}[k^\ell_{\ell m}] \\ &= \frac{(2\ell+1)}{8\pi} |U_{\ell m}|^2 \omega_m \mathrm{Im}[k^\ell_{\ell m}] \end{aligned} \tag{2.17}$$

in units of $G = M = R = 1$. We make use of this relation to calculate $\mathrm{Im}[k^\ell_{\ell m}]$, which enters into our orbital evolution equations in 2.3. Note that due to viscous coupling between modes (e.g., Braviner and Ogilvie, 2015), values of $\mathrm{Im}[k^\ell_{\ell m}]$ computed from 2.14 and 2.17 deviate from results achieved by treating mode damping independently. We discuss this discrepancy further in Section 2.6, and in a companion paper (Dewberry and Wu, 2024).

Orbital evolution due to tidal dissipation

Following Ogilvie, 2014, the evolution of the orbital semi-major axis a and stellar spin Ω_s for circular, coplanar orbits under tidal dissipation are given by

$$\frac{1}{a}\frac{\mathrm{d}a}{\mathrm{d}t} = -3\,\mathrm{Im}\left[k_{2,2}^2\right]\frac{M'}{M}\left(\frac{R}{a}\right)^5\Omega_o \tag{2.18}$$

$$\frac{1}{\Omega_s}\frac{\mathrm{d}\Omega_s}{\mathrm{d}t} = \frac{3}{2}\,\mathrm{Im}\left[k_{2,2}^2\right]\frac{L_o}{L_s}\frac{M'}{M}\left(\frac{R}{a}\right)^5\Omega_o \tag{2.19}$$

where the ratio of the orbital angular momentum to the spin angular momentum of the star is, generally,

$$\frac{L_o}{L_s} = \frac{GMM'(1-e^2)^{1/2}}{I_s\Omega_s\Omega_o a}. \tag{2.20}$$

Here Ω_o is the orbital frequency, I_s is the moment of inertia of the star, and e is the orbital eccentricity–throughout this work $e = 0$.

We integrate these equations to study the tidal evolution of these quantities. In the calculations described in Section 2.5, we adopt the approach appropriate for Earth-mass planets and ignore the tidal contribution to the spin from Equation 2.19; in Section 2.5, we discuss the validity of this assumption.

The timesteps required to accurately integrate Equations 2.18 and 2.19 are much smaller than the timescales of stellar evolution, and to recalculate the full frequency dependence of $\mathrm{Im}\left[k_{2,2}^2\right]$ at each step in the orbital evolution is prohibitively expensive. As a result, for each model in a given set of snapshots of stellar evolution, we calculate the imaginary part of the Love number as a function of tidal forcing frequency, $\mathrm{Im}\left[k_{2,2}^2\right](\omega_m)$. We discuss the details of this calculation and of our stellar models in Section 2.3. Combining the profiles of $\mathrm{Im}\left[k_{2,2}^2\right](\omega_m)$ for all the stellar models provides a grid of values across tidal forcing frequency and stellar age, for a total of three dissipation grids corresponding to the initial rotation periods of 1, 5, and 10 days. With each pre-calculated grid in hand, at each timestep in the orbital evolution we interpolate over the grid to find the value of $\mathrm{Im}\left[k_{2,2}^2\right]$ evaluated at the tidal forcing frequency ω_m and age of that step.

Normal mode oscillations of realistic stellar models

Using MESA (Paxton et al., 2011; Paxton et al., 2013; Paxton et al., 2015; Paxton et al., 2018; Paxton et al., 2019), we simulate the evolution of a star with zero-age main sequence (ZAMS) mass $0.2\,M_\odot$, using three different initial rotation periods of 1, 5, and 10 days, respectively. We prescribe the rotational evolution of the star

due to magnetic braking using the model of Matt et al., 2015. In this formulation of magnetic braking, the torque on the star encounters two regimes: saturated magnetic torque for small Rossby number, which applies below a critical rotation period $P_{\rm sat} \simeq 0.1 P_\odot \tau_{\rm cz}/\tau_{\rm cz,\odot}$; and unsaturated magnetic torque for slowly rotating stars where magnetic activity strongly correlates with the Rossby number. Here, $\tau_{\rm cz}$ is the convective turnover time. The chosen initial rotation periods of 5 and 10 day pass through observed values for young clusters $\sim$ 5 Myr as well as older clusters at $\sim$ 500 Myr and a few Gyr (Matt et al., 2015).

In each simulation, we evolve the star from the PMS to the terminal-age MS. For this initial mass, the star remains fully convective until $\approx$ 70 Gyr, about 20 Gyr before the terminal age MS. Figure 2.1 shows the evolution of the stellar radius, dimensionless stellar rotation rate, and rotation period for each of the initial conditions. As the stellar radius contracts, the star spins up until $\approx$100 Myr, after which it begins to spin down to $\sim$100 day rotation periods by 10 Gyr. The dimensionless stellar rotation rate, which is the stellar spin in units of the dynamical frequency $\Omega_{\rm dyn} = (GM/R^3)^{1/3}$, drops below 10^{-3} by $\approx$ 2.5 Gyr.

Throughout the PMS and MS evolution of our star, we use the 2D pseudospectral methods outlined in Dewberry et al., 2021; Dewberry and Lai, 2022; Dewberry, 2023 to compute normal modes of stellar oscillation in order to calculate the tidal response. These non-perturbative methods for finding stellar oscillation modes, which can capture the full effects of the Coriolis force by treating the linearized fluid equations as non-separable in (r, θ) under rotation, assume rigid rotation and zero viscosity. The axisymmetry of the background state allows modes to be labeled by unique azimuthal wavenumbers m. Assuming spherical symmetry, the 1D, radial profiles of realistic stellar structure from MESA constitute the equilibrium profiles for the 2D pseudospectral methods, which we use to solve for adiabatic normal modes with time dependence $\exp[-i\omega_\alpha t]$ for rotating frame mode frequencies ω_α.

In this work, we solve for modes with azimuthal wavenumber $m = 2$ and thus consider tidal forcing frequencies $\omega_m = 2(\Omega_o - \Omega_s)$. We keep track of the $\ell = 2, 4, 6$ prograde and retrograde f-modes, where ℓ is the spherical harmonic degree, as well as 12 i-modes. Here, prograde refers to modes whose inertial-frame frequency ω_α is positive, and retrograde modes have $\omega_\alpha < 0$. For the i-modes, we characterize them by the number of nodes in directions that are roughly horizontal (n_1) and vertical (n_2), where horizontal describes the direction of the cylindrical radius R, and vertical is the cylindrical z direction (Wu, 2005a). We consider the $n_1 + n_2 = 1$, $n_1 + n_2 = 2$,

and $n_1 + n_2 = 3$ prograde and retrograde i-modes. To refer to the modes in the text, we follow the notation of Dewberry and Lai, 2022 so that $f_{\ell,m,\pm}$ denotes the f-modes and $i_{m,n_1,n_2,\pm}$ labels the i-modes, with + and − indicating prograde or retrograde modes, respectively. Inertial modes are only labeled prograde or retrograde if the m, n_1, n_2 values are duplicated in another mode. The chosen set of i-modes are the longest-wavelength modes; shorter-wavelength modes are unlikely to contribute significantly to tidal dissipation as they have smaller tidal overlap coefficients $Q^{\alpha}_{\ell m}$ and smaller amplitudes.

For each stellar profile, we calculate the dissipation D from Equation 2.14, with Equations 2.15 and 2.16 summed over the oscillation modes α computed for each stellar model. In each sum, we include the f-modes and i-modes listed above. Equation 2.14 involves a double sum over the mode velocity eigenfunctions that allows us to capture the dissipative coupling between different modes, e.g., $I_{\alpha\beta}$ (Equation 2.12). In most prior work that takes the modal decomposition approach, they instead perform a single sum over each mode to calculate tidal dissipation (using, e.g., Equation 2.30) that does not incorporate this coupling. However, we find that the terms $I_{\alpha,\beta}$ can be quite large and contribute significantly to the dissipation away from mode resonances. Given D, the imaginary part of the Love number $\mathrm{Im}\left[k^2_{2,2}\right]$ as a function of tidal forcing frequency ω_m can be found from Equation 2.17.

Viscous dissipation in convective zones

To treat the viscous dissipation of the tides, we estimate the effective turbulent viscosity of convection throughout the fully convective models. The kinematic eddy viscosity ν of turbulent convective friction can be described using mixing-length theory as (Zahn, 1966b):

$$\nu_{\mathrm{NR}} \sim v_{\mathrm{con}} l_{\mathrm{con}} \sim \left(\frac{L_{\mathrm{con}}}{4\pi\rho r^2}\right)^{1/3} H, \tag{2.21}$$

where v_{con}, l_{con}, and L_{con} are the convective velocity, mixing length, and convective luminosity, respectively, H is the pressure scale height, and ρ is the density. This simple estimate ignores the effect of rotation on convective flows, as well as the attenuation of the dissipation efficiency when the tidal forcing frequency is much larger than the convective turnover frequency, $\omega_m \gg \omega_{\mathrm{con}} \sim v_{\mathrm{con}}/l_{\mathrm{con}}$ (see, e.g., Zahn 1966b; Goldreich and Keeley 1977; Duguid, Barker, and Jones 2020a).

Figure 2.2 shows the variation of $l_{\mathrm{con}} = H$, v_{con}, and the kinematic eddy viscosity

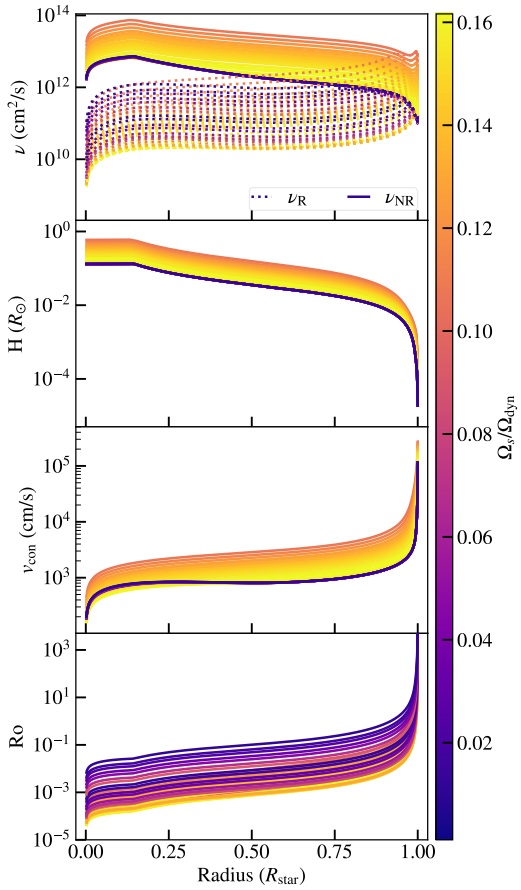

Figure 2.2: The kinematic viscosity (first panel), scale height (second panel), convective velocity (third panel), and Rossby number (fourth panel) versus radial coordinate (scaled by the total stellar radius) for a set of profiles during the evolution of a $P_{\rm rot,0}$ = 5 day model. The top panel shows the turbulent convective viscosity with ($\nu_{\rm R}$, Equation 2.26) and without ($\nu_{\rm NR}$, Equation 2.21) a rotational correction. As Equation 2.26 is a function of Rossby number, $\nu_{\rm R}$ varies with rotation and approaches the value of $\nu_{\rm NR}$ towards the surface of the star where the Rossby number is large. On the main sequence, $\nu_{\rm NR}$, H, and $v_{\rm con}$ remain nearly constant so all lines lie on top of each other under the purple line.

$\nu_{\rm NR}$ (solid lines in top panel) with radial coordinate, colored by the dimensionless stellar rotation rate for the $P_{\rm rot,0} = 5$ day models. While the star is on the pre-MS, the scale height and convective velocity are elevated because the stellar radius and luminosity are much larger than on the MS, leading to higher viscosity on the pre-MS (solid yellow and orange curves in Figure 2.2). While on the MS, the stellar radius remains nearly constant, so the scale height, convective velocity, and thus $\nu_{\rm NR}$ all remain similar throughout the rest of the star's lifetime as it spins down to small values of $\Omega_s/\Omega_{\rm dyn}$ (solid purple curves).

However, rapid rotation such as that experienced by our stellar models affects turbulent convective flows, in particular by inhibiting the efficiency of the turbulent friction. Mathis et al., 2016 address how the viscosity in Equation 2.21 should be modified for the rotating case by scaling the convective velocity and mixing length for rapid rotation to the non-rotating case (Stevenson, 1979; Barker, Dempsey, and Lithwick, 2014):

$$\frac{v_{\rm con}({\rm Ro})}{v_{\rm con}(\Omega_s = 0)} = 1.5({\rm Ro})^{1/5} \tag{2.22}$$

$$\frac{l_{\rm con}({\rm Ro})}{l_{\rm con}(\Omega_s = 0)} = 2({\rm Ro})^{3/5}. \tag{2.23}$$

Here ${\rm Ro} = \omega_{\rm con}/\Omega_s$ is the Rossby number. Mathis et al., 2016 use the above scalings for the rapidly rotating regime of ${\rm Ro} \lesssim 0.25$, whereas in the slowly rotating regime of ${\rm Ro} \gtrsim 0.25$ they employ the following:

$$\frac{v_{\rm con}({\rm Ro})}{v_{\rm con}(\Omega_s = 0)} = 1 - \frac{1}{242({\rm Ro})^2} \tag{2.24}$$

$$\frac{l_{\rm con}({\rm Ro})}{l_{\rm con}(\Omega_s = 0)} = \left(1 + \frac{1}{82({\rm Ro})^2}\right)^{-1}. \tag{2.25}$$

With these scaling relations, the kinematic eddy viscosity in the rotating case may be estimated as

$$\begin{aligned} \nu_{\rm R}({\rm Ro}) &\sim v_{\rm con}({\rm Ro}) l_{\rm con}({\rm Ro}) \\ &\sim \nu_{\rm NR} \frac{v_{\rm con}({\rm Ro})}{v_{\rm con}(\Omega_s = 0)} \frac{l_{\rm con}({\rm Ro})}{l_{\rm con}(\Omega_s = 0)}. \end{aligned} \tag{2.26}$$

As expected from the rotational evolution of the star (Figure 2.1), Ro is much smaller throughout the star during the pre-MS than the late MS. From the bottom panel of Figure 2.2, we see that ${\rm Ro} \ll 1$ in the stellar interior, but increases sharply towards the surface as H drops and $v_{\rm con}$ rises. As a result, the viscosity transitions between

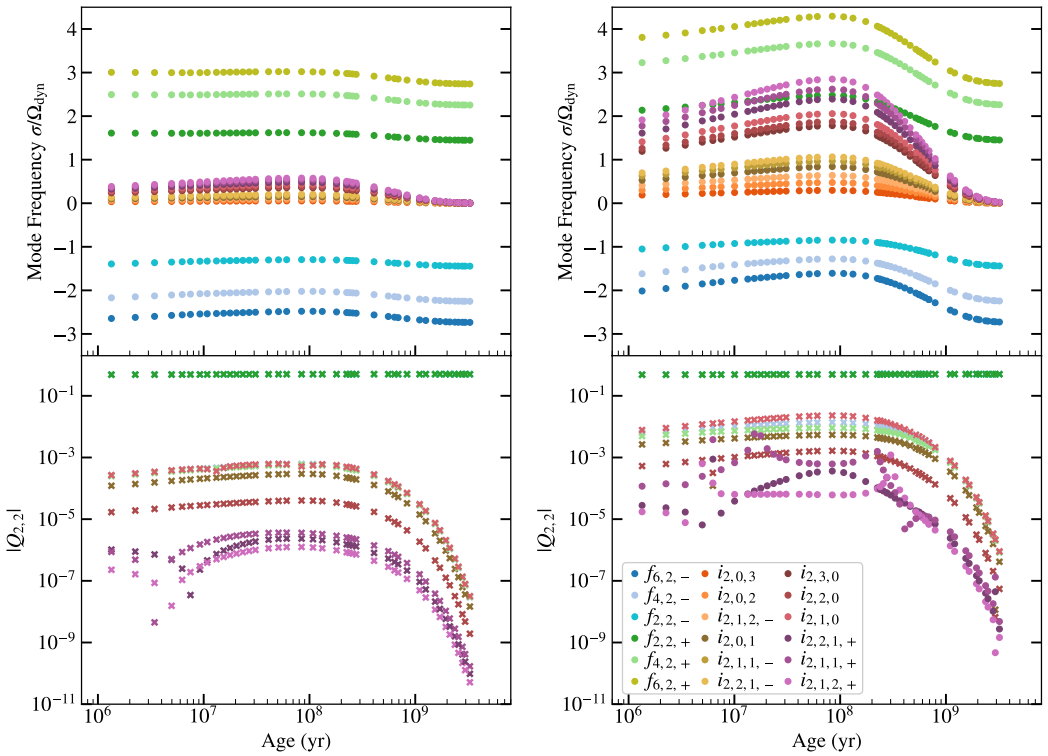

Figure 2.3: Evolution of the inertial-frame mode frequencies σ in units of the dynamical frequency $\Omega_{\rm dyn}$ (top panel) and the absolute value of the $\ell = m = 2$ tidal overlap coefficients $Q_{\ell,m}$ (bottom panel) for the set of f-modes and i-modes we include during the pre-MS to MS evolution of the $P_{\rm rot,0} = 5$ day (left) and 1 day (right) sets of stellar models. In the bottom panel, a subset of these modes are plotted. For the $P_{\rm rot,0} = 1$ day models, i-modes that experience avoided crossings are plotted with a circle marker in the bottom panel.

the rapidly rotating and slowly rotating regimes within the star. The dotted lines in the top panel of Figure 2.2 illustrate that the effect of rapid rotation in our models is to lower the kinematic viscosity in the majority of the star, as Ro is small except towards the surface. In addition, the rotationally corrected viscosity now varies on the MS due to the dependence on Ro, so that the slowly rotating models towards the late MS $\gtrsim$ 1 Gyr have 1–2 orders of magnitude larger $\nu_{\rm R}$ than at peak rotation around $\sim$ 10–100 Myr.

A second factor not implemented here is the frequency-dependent attenuation of the efficiency for rapid tide where $\omega_m \gg \omega_{\rm con}$. In the literature, several scalings have been proposed for this reduction, including linear (Zahn, 1966b; Penev et al., 2007; Penev, Barranco, and Sasselov, 2009) or quadratic (Goldreich and Keeley, 1977; Goodman and Oh, 1997; Ogilvie and Lesur, 2012; Duguid, Barker, and

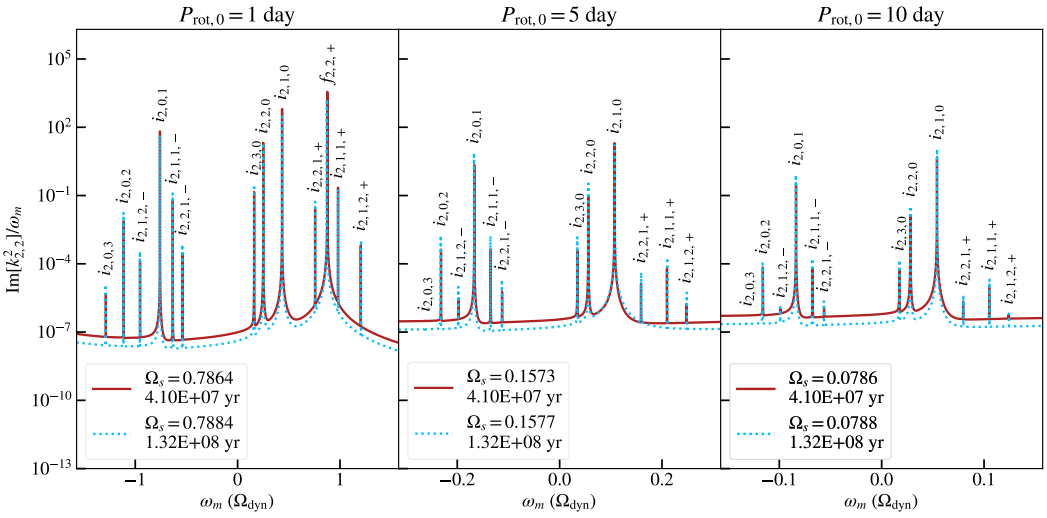

Figure 2.4: Imaginary parts of $k^2_{2,2}$ as a function of tidal forcing frequency ω_m (in units of the dynamical frequency $\Omega_{\rm dyn}$). The y-axis is scaled by ω_m, and panels are labeled by the value of $P_{\rm rot,0}$ used to evolve the stellar model. In each panel, the red lines show the dissipation on the pre-MS for the stellar rotation rates Ω_s (in units of $\Omega_{\rm dyn}$) listed in the legend, whereas the blue dotted lines show the same for a model on the MS with a very similar rotation rate. The x-axis limits in each panel are limited to $[-2\Omega_s, 2\Omega_s]$ to show the inertial mode range. Each resonant peak is labeled by the mode responsible for the resonance. The dissipation is larger on the pre-main sequence due to larger turbulent convective viscosity.

Jones, 2020a), with some arguing that no reduction is appropriate (Terquem, 2023). For i-modes, whose frequencies scale with the stellar rotation rate, the rapid tide attenuation will effectively scale as Ro or Ro^2 depending on which prescription is taken. In the former case, we expect similar effects on the mode damping compared to the considerations of rotating convection described above, but in the case of quadratic scaling, the suppression will be more dramatic than shown here. Furthermore, if both reductions act simultaneously, the viscosity would strongly scale with Ro and decrease even more.

We repeat our calculation of the dissipation as described in Section 2.3 for both assumptions of the kinematic viscosity $\nu_{\rm R}$ or $\nu_{\rm NR}$ as described above. The fiducial results shown throughout this work use the results from assuming $\nu_{\rm R}$, and we address comparisons between the two assumptions in Sections 2.4 and 2.5.

2.4 Tidal dissipation across stellar evolution

Mode evolution with stellar evolution

The top panel of Figure 2.3 shows the evolution of the inertial-frame mode frequency σ for the set of f-modes and i-modes tracked in this work, for initial conditions $P_{\rm rot,0} = 5$ and 1 day. The description for $P_{\rm rot,0} = 5$ day is representative of $P_{\rm rot,0} = 10$ day as both are calculated for slowly rotating stars. As the stellar spin increases and decreases (see Figure 2.1), the i-mode frequencies are generally proportional to the stellar spin and follow the same evolution. For the slower-spinning models, the f-mode frequencies also increase and decrease with stellar spin slightly, but remain fairly constant and well separated from the i-mode frequencies. In the $P_{\rm rot,0} = 1$ day model on the right, the i-mode frequencies again increase and decrease with rotation, but here the f-mode frequencies also show a significant increase with rotation rate. As the star spins down to $\Omega_s/\Omega_{\rm dyn} \sim 10^{-3}$ at ~ 2.5 Gyr, the i-mode frequencies similarly approach 0 in both models.

The bottom panels show the absolute value of the $\ell = m = 2$ tidal overlap coefficients $|Q_{2,2}|$ (Equation 2.10), which affect the mode amplitudes; for all i-modes, these drop by several orders of magnitude once the star spins down to $\Omega_s/\Omega_{\rm dyn} \sim 10^{-3}$ at a few Gyr. Throughout the evolution, the prograde and retrograde $\ell = 2$ f-modes still have much larger $|Q_{2,2}|$, but the next largest values come from the longest-wavelength i modes, e.g., $i_{2,0,1}$ and $i_{2,1,0}$, as well as the $\ell = 4$, $m = 2$ f-modes.

In the $P_{\rm rot,0} = 1$ day model, the prograde $\ell = 2, m = 2$ f-mode frequency crosses those of the highest-frequency i-modes at large rotation rates $\Omega_s \approx 0.6$–$0.8\,\Omega_{\rm dyn}$. This leads to several instances of an "avoided crossing", during which the f-mode and i-mode mix in character as they approach one another in frequency (see Dewberry and Lai, 2022, for a discussion of similar i-mode/f-mode mixing in isentropic polytropes). These avoided crossings occur between the f-mode $f_{2,2,+}$ and the i-modes $i_{2,1,1,+}$ and $i_{2,1,2,+}$, which are distinguished with dots instead of crosses in the bottom right panel of Figure 2.3. The i-mode $i_{2,2,1,+}$ also approaches $f_{2,2,+}$ in frequency near the maximum stellar rotation rate (also shown as dots). These three i-modes show increases in $|Q_{2,2}|$ over several orders of magnitude as their mode frequencies approach or cross that of the f-mode. For the $i_{2,2,1,+}$ i-mode whose frequency nears, but does not cross, that of the f-mode, the enhancement is reduced yet still visible. Though none of these i-modes achieve $|Q_{2,2}|$ values that are comparable to the f-mode's tidal overlap integral, the effect of mode mixing allows these relatively short wavelength i-modes to contribute similar $|Q_{2,2}|$ coefficients

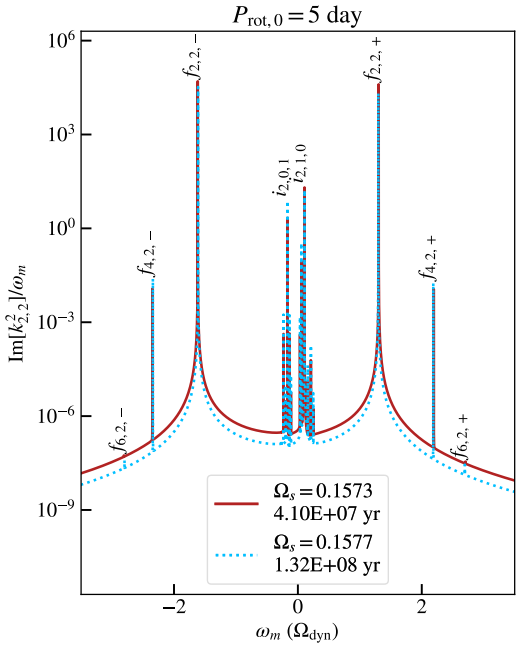

Figure 2.5: Same as Figure 2.4, but zoomed out to show the f-modes for the $P_{\rm rot,0} = 5$ day models. The f-mode and largest i-mode resonances are labeled by the mode responsible for each resonance.

compared to the longest-wavelength i-modes, whereas they would otherwise have negligibly small $|Q_{2,2}|$ in comparison. The consequence, as we discuss below in the context of Figure 2.4, is to enhance the amplitudes of these modes during these periods of rapid rotation, leading to greater resonant dissipation.

Tidal dissipation coupled with stellar evolution

We compute the frequency-dependent dissipation D from Equation 2.14 in each stellar model, using the f-modes and i-modes shown in Figure 2.3 to construct the velocity fields of Equation 2.16. Models shown in this section use the rotation correction to viscosity of Equation 2.26 unless specified otherwise.

Figures 2.4–2.5 show the positive-definite quantity $\mathrm{Im}\left[k^2_{2,2}\right]/\omega_m$ versus ω_m at different snapshots in the stellar evolution. In each panel corresponding to different $P_{\rm rot,0}$, the spikes that rise orders of magnitude above the baseline dissipation are peaks of resonance with the stellar oscillation mode as labeled. Modes with shorter peaks are shorter-wavelength and have smaller maximum amplitudes due to damping (Equation 2.16) and smaller tidal overlap integrals (Equation 2.10). Note that $\mathrm{Im}\left[k^2_{2,2}\right]/\omega_m$ is constant across $\omega_m = 0$ because of the scaling by ω_m. The value

of $\mathrm{Im}\left[k_{2,2}^2\right]$ actually approaches zero at $\omega_m = 0$, which corresponds to the case of co-rotation ($\Omega_s = \Omega_o$).

In red, the stellar model shown is on the pre-MS, whereas the blue dashed curve is for a model on the MS with a similar rotation rate (in units of $\Omega_{\rm dyn}$). Compared to the pre-MS model, the more compact star on the MS has a lower viscosity and therefore smaller off-resonant dissipation even for the same dimensionless rotation rate. For the models shown here, the difference amounts to a factor of a few, but similar comparisons involving the more extended star on the early pre-MS can differ by up to an order of magnitude.

Figure 2.4 focuses on the region $-2\Omega_s < \omega_m < 2\Omega_s$, which is the range over which inertial modes are excited. For $P_{\rm rot,0} = 1$ day at the rotation rate of $\Omega_s/\Omega_{\rm dyn} \sim 0.8$ shown, the peak for $f_{2,2,+}$ falls within this range and is very near in frequency to $i_{2,2,1+}$ and $i_{2,1,1,+}$. In the vicinity of this rotation rate, the avoided crossings between the f-mode and i-modes as described in the context of Figure 2.3 amplify the i-mode dissipation. In contrast, the same two i-modes in slower-rotating models appear with some of the smallest resonant spikes, as they have quite short wavelengths and small $|Q_{2,2}|$ values. Throughout the evolution, all the modes we consider for $P_{\rm rot,0} = 1$ day augment the dissipative response significantly near resonance, but fewer modes contribute significantly for the slower-rotating stars. This corresponds to overall smaller magnitudes of $|Q_{2,2}|$ exhibited by the slower-rotating models.

Figure 2.5 shows a larger range in tidal forcing frequency for the $P_{\rm rot,0} = 5$ day model. In this region, we can see that the f-mode amplitudes dominates the dissipation away from resonant peaks, which can also be thought of as the equilibrium tidal response. As the initial rotation period increases, the dissipation away from resonance mildly increases due to the rotational correction to viscosity. The largest dissipation comes from $\ell = m = 2$ f-modes and the longest-wavelength i-modes ($i_{2,1,0}$ and $i_{2,0,1}$). In older models with slower rotation rates, the strength of resonant i-mode dissipation fades as the star spins down greatly on the MS, tracking the rapid decline of $Q_{2,2}$ with age as seen in Figure 2.3. The $\ell = m = 2$ f-mode peaks maintain similar heights throughout the evolution.

As the star spins up from a few–100 Myr, the viscosity grows more inefficient due to the decreasing Rossby number, and the dissipation away from resonance correspondingly decreases. Once the star spins down significantly, the Rossby number and consequently the viscosity grow. The non-resonant dissipation is similar on the pre-MS at $\lesssim 10$ Myr and on the late MS at ~ 2 Gyr, even though the star

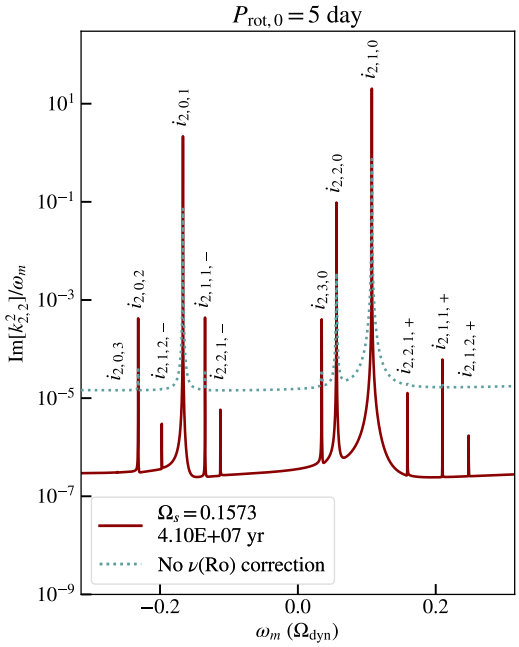

Figure 2.6: Similar to the center panel of Figure 2.4 ($P_{\rm rot,0}$ = 5 day), $\mathrm{Im}[k^2_{2,2}]$ scaled by ω_m as a function of tidal forcing frequency ω_m is shown, but now to compare the effect of viscosity. The red line shows the dissipation using the correction to viscosity due to rotation (Equation 2.26). The blue dotted lines show the same but using viscosity without the rotation correction (Equation 2.21). Including the effects of rotation lowers the viscosity, leading to sharper resonant peaks, but smaller off-resonant dissipation by 1–2 orders of magnitude.

is spinning 10–100 times faster on the pre-MS. Since the fully convective star has a much larger radius on the pre-MS, the convective velocity and scale height are correspondingly larger, leading to larger viscosities on the pre-MS for a given rotation rate.

Comparison of different assumptions for the viscosity

We compare in Figure 2.6 the effects of including or excluding the correction to viscosity under rapid rotation. In red, the quantity $\mathrm{Im}\left[k^2_{2,2}\right]/\omega_m$ is shown for the same pre-MS model as in Figures 2.4 and 2.5, for which we compute the dissipation assuming the kinematic viscosity to be $\nu_{\rm R}$ (Equation 2.26). In blue, the same model is shown for a calculation using $\nu_{\rm NR}$ (Equation 2.21) instead. As seen in Figure 2.2, $\nu_{\rm NR} \gg \nu_{\rm R}$ throughout the majority of the star, and this impacts the dissipation curves in two significant ways. The off-resonance dissipation is orders of magnitude larger when using the $\nu_{\rm NR}$ instead of $\nu_{\rm R}$, which follows from the

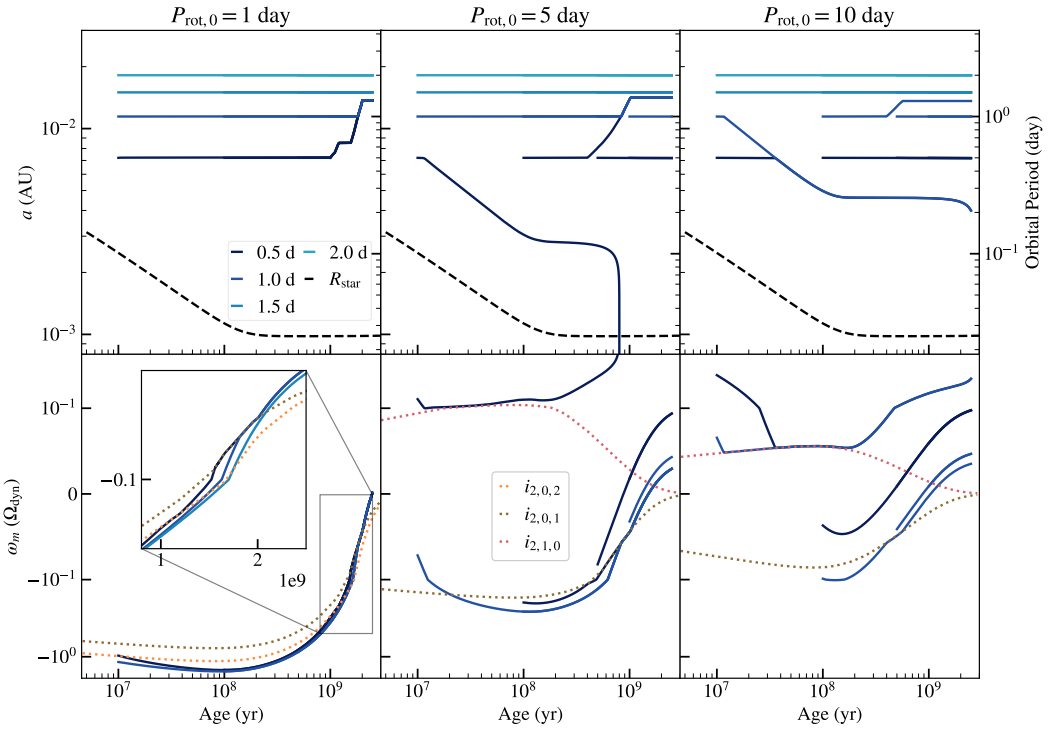

Figure 2.7: **Top row**: Evolution of the semi-major axis or orbital period of a $M_p = M_e$ Earth-mass companion for the different initial orbital periods shown in the legend in the upper left. Each column depicts results from each stellar evolutionary model with initial rotation periods $P_{\rm rot,0}$ as labeled, and the dissipation is calculated using the correction to viscosity under rotation (Equation 2.26). The dashed black line shows the radius of the star. **Bottom row**: The tidal forcing frequency ω_m (in units of the dynamical frequency) for the same models. Dotted lines show the rotating-frame mode frequencies ω_α for the i-modes listed in the legend in the center panel. Significant migration occurs when the companion's tidal forcing frequency enters a resonance lock with a stellar oscillation mode, which is visualized as a solid line overlapping with a dotted line in the bottom panels.

attenuation of $\nu_{\rm R}$ at small Ro by $\approx$ 2–3 orders of magnitude. Furthermore, the resonant spikes are wider and shorter for the higher viscosity, $\nu_{\rm NR}$. As discussed in Section 2.5, we expect larger off-resonance dissipation to cause more rapid orbital migration as a result of the equilibrium tide, whereas smaller peak heights decrease the likelihood of resonance locking for orbital evolutionary calculations that utilize the Ro-independent viscosity. We note that if the additional effect of frequency-dependent attenuation of the viscous efficiency were to be included such that the viscosity scaled even more strongly with Ro, then the profiles of $\mathrm{Im}\left[k^2_{2,2}\right]/\omega_m$ would trend towards even smaller dissipation away from resonance and narrower, taller peaks.

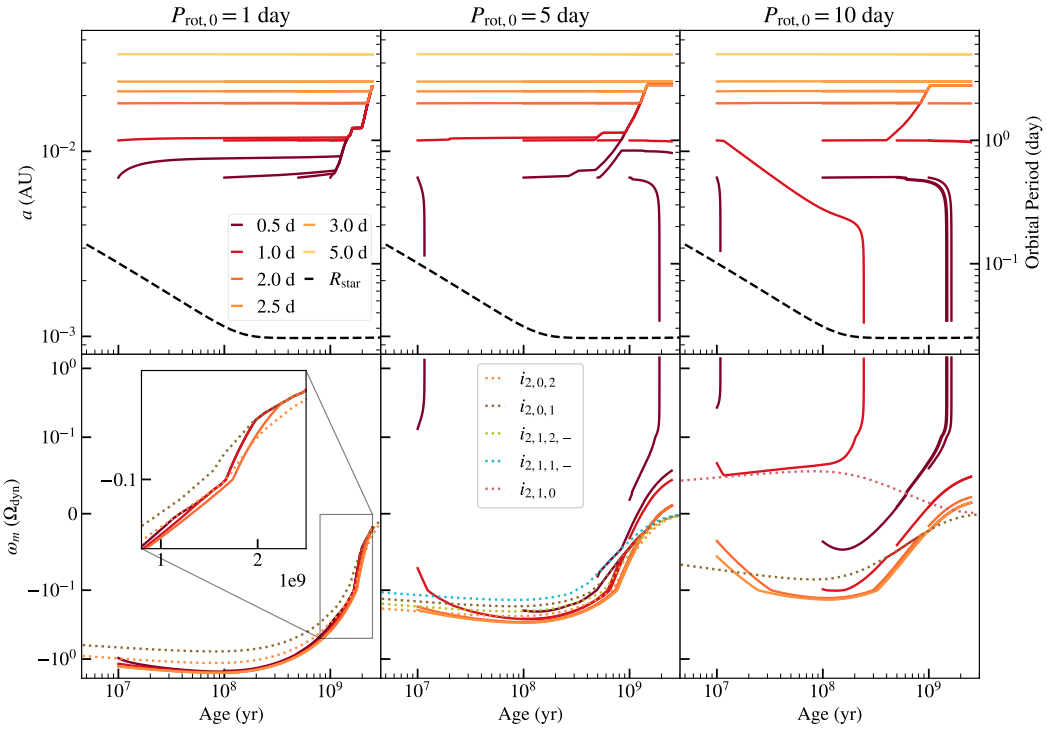

Figure 2.8: Same as Figure 2.8, but for a $M_p = M_j$ Jupiter mass companion.

2.5 Orbital evolution due to stellar tides

To study the orbital dynamics caused by the frequency-dependent tidal dissipation coupled with stellar evolution as presented in the previous section, we integrate planetary orbits beginning at stellar ages of 10 Myr, 100 Myr, 0.5 Gyr, and 1 Gyr. This spread in initial ages spans scenarios from in-situ or disk-driven formation of close-in planets, in which planets develop $\lesssim$ 10 day orbits while within the proto-planetary disk which persists until $\sim$ 10 Myr, to dynamically driven migration, in which planets may reach short-period orbits throughout the stellar lifetime. At each stellar age, we initialize planets at a range of orbital periods from $<$ 1 day to a few day. We repeat this for an Earth-mass companion ($M_p = M_e$) and a Jupiter-mass companion ($M_p = M_j$), and we also complete the entire procedure for each dissipation grid associated with initial stellar rotation rates $P_{\rm rot,0}$ = 1, 5, and 10 day. For each orbital integration, we assume co-planar, circular orbits and integrate Equations 2.18–2.19 from the respective initial stellar age to a final age of 2.5 Gyr. The stellar lifetime is, of course, much longer than this endpoint, but the stellar spin has slowed so drastically by 2.5 Gyr that our i-mode frequencies approach zero, so beyond this age we expect the f-mode dissipation (i.e., equilibrium tides) to govern the system.

Figure 2.7 shows a sample of orbital integrations for $M_p = M_e$ for each initial stellar rotation rate. The top panels show the semi-major axis evolution, while bottom panels show the evolution of the tidal forcing frequency ω_m and the rotating-frame mode frequencies ω_α. For all values of the initial stellar rotation period $P_{\rm rot,0}$, orbits with initial orbital period $P_{\rm orb,0} \gtrsim 1.5$ day experience negligible orbital migration. For these planets that are further away such that the ratio (R/a) is small, $\dot{a}$, which depends on $(R/a)^5$ (Equation 2.18), remains tiny, and thus the rate of change of the orbital frequency $\dot{\Omega}_o$ does not appreciably affect the evolution of the tidal forcing frequency $\dot{\omega}_m$. Nevertheless, the tidal forcing frequency still changes over time for these orbits due to the stellar spin evolution, but it usually traverses a path where the dissipation away from resonance is too low to affect the orbits.

For the shortest initial orbital periods shown of $P_{\rm orb,0} = 0.5$ and 1 day, we observe that resonance locking between the tidal forcing frequency and stellar oscillation modes causes significant orbital migration. We first consider the Earth-mass planetary orbits shown in Figure 2.7. For $P_{\rm rot,0} = 1$ day, the star spins faster than all planetary orbits at $P_{\rm orb,0} \gtrsim 0.5$ day so that the planets migrate outward, no matter at what age the integration begins. The planet at $P_{\rm orb,0} = 0.5$ day evolves into a brief resonance with the i-mode $i_{2,0,2}$, which is indicated in the bottom panel by the dark blue line overlapping with the dotted pink line (shown more clearly in the inset panel). After it breaks out of resonance with $i_{2,0,2}$ having migrated slightly outward, it enters another resonance with the longest-wavelength retrograde i-mode, $i_{2,0,1}$, and remains in that resonance until $\sim$ 2 Gyr. The planet at $P_{\rm orb,0} = 1$ day experiences the resonance with $i_{2,0,1}$ for a brief interval as well, and its orbit then converges with that of the $P_{\rm orb,0} = 0.5$ day planet. By 2.5 Gyr, both of these planets arrive at $P_{\rm orb} > 1$ day orbits, regardless of the time of formation.

For dissipation in a more slowly rotating star with $P_{\rm rot,0} = 5$ day, most orbits begin retrograde ($\Omega_o < \Omega_s$); however, planets initialized with $P_{\rm orb,0} = 0.5$ day at early times $\leq$ 10 Myr are instead prograde ($\Omega_o > \Omega_s$). These earlier prograde orbits enter into a resonance lock with the longest-wavelength prograde i-mode $i_{2,1,0}$ that lasts from $\approx$ 10–100 Myr, causing significant orbital decay to $P_{\rm orb} \sim 0.1$ day. Eventually, between 700–800 Myr, the planet plunges into the star because of the equilibrium tide, which can be understood equivalently as dissipation due to the $\ell = m = 2$ f-mode. If these planets arrive at $P_{\rm orb,0} = 0.5$ day between 50–400 Myr, they will instead migrate outward in a resonance lock with $i_{2,0,1}$ that breaks at $\sim$1 Gyr; however, if they land at $P_{\rm orb,0} = 0.5$ day from $\approx$ 500 Myr onward, they

are unable to lock into resonance and remain stationary. At $P_{\rm orb,0} = 1$ day, orbits remain unaffected by dissipation until $\sim$ 700 Myr, at which point they will also lock with $i_{2,0,1}$ and converge with the $P_{\rm orb,0} = 0.5$ day orbits to migrate slightly outward to $P_{\rm orb} > 1$ day. However, planets arriving at $P_{\rm orb,0} = 1$ day after $\sim$1 Gyr do not undergo migration.

For our slowest set of stellar rotation rates with $P_{\rm rot,0} = 10$ day, planets closer than $P_{\rm orb} \lesssim 1.5$ day will migrate inward until $\sim$100 Myr due to resonance locking with $i_{2,1,0}$. All these orbits converge to $P_{\rm orb} \sim 0.2$ day by 2.5 Gyr due to equilibrium tidal dissipation. Only planets at $P_{\rm orb,0} = 1$ day initialized between 50–500 Myr migrate outward. Overall, if Earth-mass planets form short-period orbits of $P_{\rm orb,0} \lesssim 1$ day at around 10 Myr, then tides tend to pull the planets from this initial position by a few Gyr. However, the final fate (migrating outward, orbital decay, or plunge-in) depends on the initial rotation rate of the star.

Figure 2.8 depicts the orbital evolution for $M_p = M_j$ companions. Jupiter-mass planets suffer stronger tidal dissipation because $\dot{a}$ is proportional to the mass ratio (Equation 2.18). Thus, even when orbits are not at resonant frequencies, more examples of migration are visible in each panel for $P_{\rm orb,0} < 2$ day. In general, the results for Jupiter mass planets are similar to those for Earth mass planets as they lock into resonance with similar modes at similar times, but with more drastic changes in the semi-major axis. Of note are the Jupiter-mass planets that form at $P_{\rm orb,0} = 0.5$ day, which mostly plunge towards the star in the $P_{\rm rot,0} = 5$ and 10 day examples. One exception is a planet for the $P_{\rm rot,0} = 5$ day stellar model that migrates outward in a resonance lock with $i_{2,1,1,-}$ at $\approx$ 500 Myr. Planets that migrate outward in resonance locks with $i_{2,0,2}$ and $i_{2,0,1}$ tend to approach similar 3 day orbits by 2.5 Gyr, independent of the stellar rotation rate.

As noted in Section 2.3, we calculate the change in stellar spin without incorporating this feedback into our orbital integrations, since including this effect is computationally prohibitive at this stage. This assumption holds well for Earth-mass planets as long as the planet is not plunging in, as Figure 2.9 shows. Even when the planet's tidal forcing frequency passes through resonance with mode frequencies, the ratio $|{\rm d}\Omega_{s,\rm tide}/{\rm d}\Omega_{s,\rm evol}|$ is small such that the change in stellar spin is dominated by the stellar evolution. In contrast, Jupiter-mass planets exert a stronger tidal torque on the star that significantly affects the stellar spin as the planetary orbit passes through resonances with various modes of the star. This introduces appreciable uncertainty in the ability of certain resonance locks with Jupiter-mass planets to

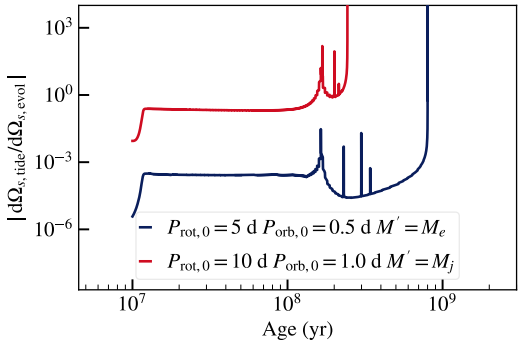

Figure 2.9: The rate of change of stellar spin from tides due to Equation 2.19, $\dot{\Omega}_{s,\mathrm{tide}}$, compared to that due to stellar evolution (magnetic braking, contraction, or expansion), $\dot{\Omega}_{s,\mathrm{evol}}$. This is shown for an Earth-mass planet in blue and a Jupiter-mass planet in red for the models listed in the legend. Note that the nearly vertical red and blue lines at 250 Myr and 800 Myr, respectively, are due to plunge-in of the planet (see corresponding times for the same models in top right panel of Figure 2.8 and top middle panel of Figure 2.7).

hold for the duration presented in this work, which is discussed further in the next section. Moreover, both Jupiter-mass and Earth-mass planets during plunge-in traverse nearly vertical lines in Figure 2.9 and attain large values of $|d\Omega_{s,\mathrm{tide}}/d\Omega_{s,\mathrm{evol}}|$. This trajectory indicates that both types of planets can greatly increase the stellar spin as their orbits decay into the star, potentially leading to tidal synchronization of the spin and orbit.

Resonance locking

In our orbital evolution calculations, we observe resonance locks that tend to occur between a few–100 Myr for inwardly migrating orbits, as well as later at a few hundred Myr–1 Gyr outwardly migrating orbits. To understand why resonance locks occur, we first note the conditions for resonance locking. The tidal forcing frequency must be nearly equal to the frequency of a mode: $\omega_m \simeq \omega_\alpha$. For the lock to be maintained, the time derivatives must remain equal as well: $\dot{\omega}_m \simeq \dot{\omega}_\alpha$. Once the resonance lock begins, the companion orbit will remain at a stable fixed point where this condition is true, unless something occurs to break the lock. The orbital migration timescale during the resonance lock follows the evolutionary timescale of the stellar oscillation mode: as the mode frequency changes over time, the tidal forcing frequency follows closely (Fuller, Luan, and Quataert, 2016).

Recalling that $\omega_m = m(\Omega_o - \Omega_s) \implies \dot{\omega}_m = m(\dot{\Omega}_o - \dot{\Omega}_s)$, we see that the ability to resonance lock depends on the interplay between the stellar spin evolution and

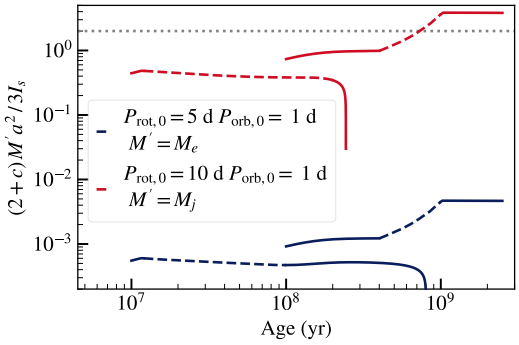

Figure 2.10: The value of the term $(2+c)M'a^2/3I_s$ in Equation 2.28 during resonance locking shown for the models listed in the legend. Orbits evolving from 10 Myr that migrate inward and from 100 Myr that migrate outward, as well as both Earth-mass (blue) and Jupiter-mass (red) planets, are shown. The resonance lock duration is shown as dashed sections in each curve. The dotted gray line denotes where $(2+c)M'a^2/3I_s = 2$. Above this value, resonance locks will break due to tidal torque on the stellar spin, which was not included in these models.

the orbital evolution. In this work, we do not incorporate the feedback of the tidal dissipation onto the stellar spin, so $\dot{\Omega}_s$ is given by the slope of the curves in Figure 2.1. Tidal dissipation drives the change in semi-major axis $\dot{a}$, and consequently $\dot{\Omega}_o$, through Equation 2.18. Given that the planet is close enough so that $(R/a)^5$ is non-negligible, then the term $\dot{\Omega}_o$ will begin to contribute when the dissipation from $\mathrm{Im}\left[k_{2,2}^2\right]$ becomes large enough. This will occur near normal mode frequencies where the dissipation rises sharply into peaks.

We can understand migration driven by resonance locking from the condition $\dot{\omega}_\alpha \simeq \dot{\omega}_m$. Inertial modes have $\omega_\alpha \simeq c\Omega_s$, where $-2 \leq c \leq 2$ is nearly constant over time. Hence a resonance lock with an inertial mode requires

$$\dot{\Omega}_o \simeq \frac{2+c}{2}\dot{\Omega}_s \,. \tag{2.27}$$

In a resonance lock with an inertial mode, the planet can only migrate inwards if the star is spinning up, and it can only migrate outwards if the star is spinning down, such that $\dot{\Omega}_o$ and $\dot{\Omega}_s$ have the same sign.

We can further decompose the spin evolution into a component from stellar evolution, $\dot{\Omega}_{s,\rm evol}$, and a component due to tidal torques, $\dot{\Omega}_{s,\rm tide}$. The latter can be related to the orbital evolution and $\dot{\Omega}_{s,\rm evol}$ via Equations 2.18 and 2.19. The orbital evolution during the resonance lock can then be written as

$$\dot{\Omega}_o \simeq (2+c)\left[2 - \frac{(2+c)M'a^2}{3I_s}\right]^{-1}\dot{\Omega}_{s,\rm evol} \,. \tag{2.28}$$

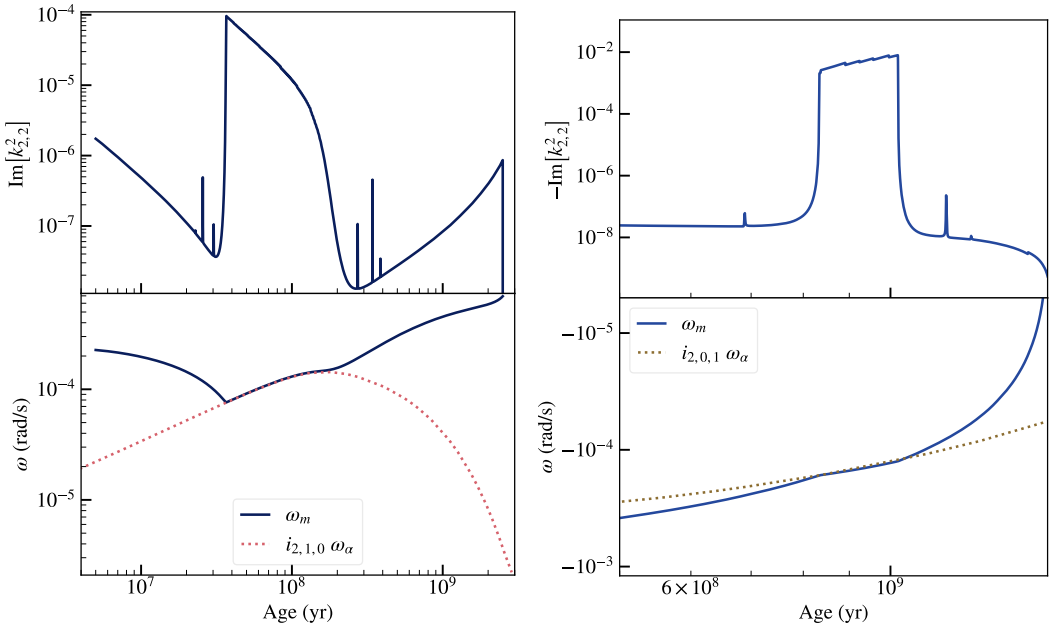

Figure 2.11: Examples of resonance locking for Earth-mass exoplanets from the $P_{\mathrm{rot},0} = 10$ day initial condition, for initial orbital periods 0.5 (left) and 1 day (right). The top panels show the time evolution of the imaginary part of the Love number $k^2_{2,2}$ (positive for prograde orbits $\omega_m > 0$, negative for retrograde orbits $\omega_m < 0$). The bottom panels show the tidal forcing frequency ω_m and the rotating-frame mode frequency ω_α for the i-mode in the legend. The left column shows an inwardly migrating resonance lock with a prograde mode $\omega_\alpha > 0$, and the right exemplifies an outwardly migrating resonance lock with a retrograde mode $\omega_\alpha < 0$.

The second term in brackets accounts for the back-reaction of the tidal torque on the star's spin, which we presently ignore in our orbital evolution calculations. It becomes important when the planet's orbital angular momentum is comparable to that of the star. In particular, as long as $(2+c)M'a^2/3I_s < 2$, then $\dot{\Omega}_o$ and $\dot{\Omega}_{s,\mathrm{evol}}$ have the same sign and resonance locking therefore continues to be possible.

In Figure 2.10, the second term in brackets in Equation 2.28 is shown for some orbits that experience resonance locking. Equation 2.28 is only valid throughout the duration of the resonance lock, which lasts for ~100 Myr in each orbit shown (dashed lines). At the start of each resonance lock, $\dot{\Omega}_o$ and $\dot{\Omega}_s$ are required to have the same sign in order to enter the resonance lock and satisfy Equations 2.27 and 2.28. Comparing the right hand sides of Equations 2.27 and 2.28 shows that this is equivalent to $\dot{\Omega}_o$ and $\dot{\Omega}_{s,\mathrm{evol}}$ having the same sign in our models, as $(2+c)M'a^2/3I_s < 2$ at the start of each resonance lock. For the majority of the models shown, the term $(2+c)M'a^2/3I_s$ never exceeds 2, so the resonance lock

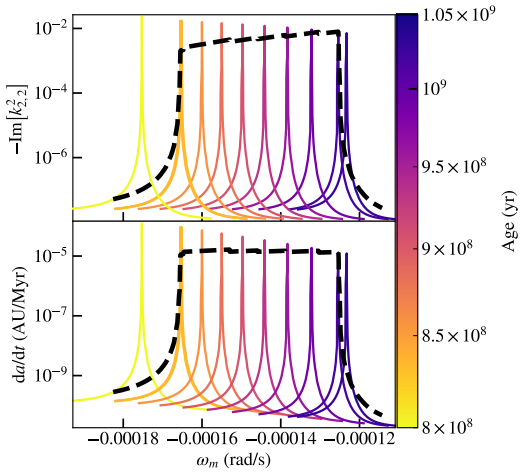

Figure 2.12: The imaginary part of the Love number (top panel) and the rate of change of the semi-major axis (bottom panel) versus tidal forcing frequency ω_m. For this example of a retrograde resonance lock, $\mathrm{Im}[k^2_{2,2}] < 0$ so $-\mathrm{Im}[k^2_{2,2}]$ is plotted. Black dashed lines show the evolution of each quantity for the planetary orbit. The peaked lines show the shape of the dissipation curve for a subset of times in the orbital evolution, shaded by the stellar age as shown in the colorbar. The dissipation is sharply peaked due to the resonant mode $i_{2,0,1}$, and the peak center moves to the right as the mode frequency ω_α evolves in time. The peak height decreases with time as the star spins down and the mode dissipation weakens. The resonance lock breaks when the dashed black line exceeds the height of the resonance peak.

may continue.

For the outwardly migrating Jupiter-mass planet whose orbital evolution begins at 50 Myr, the term $(2+c)M'a^2/3I_s$ crosses 2 (dotted gray line) during the resonance lock at 700 Myr, when the planet migrates past $P_{\rm orb} \approx 2$ day. Once $(2+c)M'a^2/3I_s > 2$, the tidal torque on the star will become important and cause the right-hand side of Equation 2.28 to switch sign. This implies that the star would have to spin up due to stellar evolution, $\dot{\Omega}_{s,\rm evol} > 0$, in order to maintain the resonance lock condition. Since the star is still spinning down at this point in our stellar models due to magnetic braking, we know the resonance lock condition should actually be broken at this point. As a result, we predict that including the back-reaction of the tidal torque on the stellar rotation will cause resonance locks with outwardly migrating Jupiter-mass planets to break once they reach $P_{\rm orb} \approx 2$ day orbits. In fact, the tidal torque could synchronize the stellar spin with the orbits of these outwardly migrating Jupiter-mass planets.

For Earth mass planets whose resonance locking is treated accurately in our models,

Figure 2.11 shows some examples of the dissipation and frequency evolution during the lock. The left panel exemplifies a resonance lock with a prograde i-mode. The bottom panel shows that the tidal forcing frequency approaches the value of ω_α, which is also changing with time. The relevant mode frequency increases as the star spins up until $\sim$ 100 Myr, then decreases with the stellar spin-down thereafter. Once $\omega_m \simeq \omega_\alpha$, the value of Im $\left[k_{2,2}^2\right]$ jumps by 3 orders of magnitude as the planetary orbit encounters the peak in dissipation due to resonance with $i_{2,1,0}$. On the right, Figure 2.11 depicts a resonance lock for retrograde orbits with $\omega_m < 0$ that occurs around a few 100 Myr–1 Gyr for a subset of initial conditions. These planets lock into resonance with $i_{2,0,1}$.

In both cases, the resonance locks break after $\sim$ 100s of Myr, which occurs when the stable fixed point of the resonance lock can no longer be maintained. For the prograde orbits on the left, the resonance lock is initially maintained as the mode frequency and tidal forcing frequency are both increasing. However, once the stellar rotation switches from spinning up to spinning down, the i-mode frequency begins to decrease and the resonant mode peak moves to decreasing forcing frequencies. The orbit thus loses the stable fixed point.

In the case of the retrograde resonance lock, the star is continuously spinning down by the time the lock begins at a few 100 Myr, so the lock breaks for a different reason. Figure 2.12 depicts the evolution of the relevant resonant mode peak for retrograde orbits shown in Figure 2.11, in terms of the value of Im $\left[k_{2,2}^2\right]$ (top) and the rate of change of the semi-major axis (bottom). The black dashed line shows the value of each quantity achieved by the planetary orbit, which in the regime of heightened dissipation can be thought of as the necessary value to maintain the fixed point. Since the peaks in both panels become shorter as the stellar rotation rate decreases, the maximum possible dissipation diminishes significantly over time. Furthermore, the value of Im $\left[k_{2,2}^2\right]$ required to maintain the fixed point actually increases with time, since more dissipation is required to sustain the necessary $\dot{a}$ as the planet migrates away. Thus, the maximum dissipation available from the resonant peak is eventually unable to sustain the torque required for the fixed point.

For the $P_{\rm orb,0}$ = 0.5–2 day orbits of Earth-mass planets shown in Figure 2.7, the only resonance locks occur for $i_{2,0,1}$, $i_{2,1,0}$, and $i_{2,0,2}$. On the other hand, for much closer orbits $\lesssim$ 0.5 day, we find that nearly every stellar oscillation mode is able to sustain resonance locks, given amenable initial conditions such that the tidal forcing frequency of the orbit can intersect with the mode frequency.

Viscosity and non-linearity

As discussed in Section 2.4, the off-resonant dissipation is orders of magnitude larger when calculating tidal dissipation using the viscosity independent of Rossby number $\nu_{\rm NR}$ (Equation 2.21). Furthermore, the resonant peaks associated with stellar oscillation modes are both wider and shorter. For the resulting orbital evolution, we find that the effect of using the larger viscosity $\nu_{\rm NR}$ is an increased prevalence of planets plunging towards the star due to non-resonant dissipation. In addition, there are fewer initial conditions $P_{\rm orb,0}$ for which resonance locking occurs. Compared to the fiducial models shown in Figure 2.7, we find that the prograde orbits decay on a shorter timescale, and the $P_{\rm orb,0} \gtrsim 1$ day orbits do not catch into resonance. Since the resonant mode peaks are shorter for this higher viscosity, $P_{\rm orb,0}$ =1 day orbits are now too far away for the resonant peak in the dissipation to be able to sustain the requisite torque for a resonance lock.

If the convective viscosity is much larger (or if the interaction of convective and tidal flows produces enhanced dissipation that is not well described with a convective viscosity; Terquem, 2021), then equilibrium tidal dissipation would likely dominate the evolution rather than locks with inertial modes. However, if convective viscosity is smaller via the Goldreich and Keeley, 1977 prescription as demonstrated by recent work (Duguid, Barker, and Jones, 2020a; Duguid, Barker, and Jones, 2020b), then equilibrium tidal dissipation will be less important. Tidal migration in that case is likely to be dominated by resonance locks, even for fairly massive planets. We leave the consideration of different prescriptions for the viscosity in the regime of rapid tides to future work.

Our study assumes that modes are linear, which we find holds true even during the resonance locks shown in Figures 2.7–2.8. Though resonance locking drives modes to larger amplitudes, typically the amplitude (Equation 2.11) remains small. In the case of Earth-mass planets, the mass ratio is small enough to ensure small mode amplitudes throughout resonance locks. Even for Jupiter-mass planets, in many cases the tidal overlap integral $Q^{\alpha}_{\ell,m}$ is small because the resonance lock occurs while the star is rotating slowly; during other resonance locks, either the frequency separation $\omega_\alpha - \omega_m$ or the mode damping rate γ_α is relatively large. Overall, we estimate mode amplitudes ξ on the order of $\sim 10^{-5}$–10^{-4}, and wavenumbers $k \sim \sqrt{n_1^2 + n_2^2 + m^2} \lesssim 4$, so that the nonlinearity measure $k\xi < 1$. Whether weakly non-linear dissipation (e.g., Weinberg et al. 2012) can increase tidal dissipation or prevent resonance locking is unclear for fully convective stars, and should be studied

in future work.

2.6 Discussion

Comparison with observed systems

The occurrence rate of Earth-like planets around M-dwarfs in the Kepler sample is less than a few percent for short orbital periods $P_{\rm orb,0} \lesssim 1$ day (Mulders, Pascucci, and Apai, 2015; Hsu, Ford, and Terrien, 2020), where our models predict migration due to resonance locking. The story appears to be similar for TESS, as recent analyses find only a few planets with Earth-like radii at $\lesssim 1$ day orbits out of the dozens of planets orbiting M-dwarfs in their sample (Rodríguez Martínez et al., 2023). The vast majority of planets lie at a few–10 day orbits, where negligible migration occurs in our fully convective stellar models. Our results indicate that a dearth of Earth-mass planets at $P_{\rm orb} \lesssim 1$ day around fully convective M-dwarfs is expected due to migration induced by resonance locks. For Earth-mass planets at $P_{\rm orb,0} \lesssim 1$ day, planets orbiting slower than the stellar spin tend to migrate out to similar ∼1.5 day orbits, whereas planetary orbits rotating faster than the stellar spin tend to decay towards the star. For Jupiter-mass planets, we expect few planets out to ∼3 days as a result of migration due to resonance locking.

By initializing our orbital evolutionary calculations at different times, we are able to explore how our predicted outcomes vary for the timescales associated with different theories of the origin of short-period planets. For in-situ planet formation or disk migration theories, changes to the orbital separation are dominated by the proto-planetary disk until the disk dissipates at a few–10 Myr (Dawson and Johnson, 2018). High-eccentricity tidal migration may operate on a large range of timescales, as it is highly sensitive to the initial conditions of the underlying planet-planet interactions. For instance, the secular interactions and the ensuing tidal migration to short orbital periods may span anywhere from ∼Myr to tens of Gyr (Dawson and Johnson, 2018).

For the fastest-spinning $P_{\rm rot,0} = 1$ day model, the Earth-mass planets will experience negligible migration until the resonance lock at ∼1–2 Gyr causes planets at $P_{\rm orb,0} < 1$ day to migrate outward. This is true during the first Gyr of the stellar evolution, no matter what time the orbital integration begins. As a result, we predict the same behavior regardless of when the planet reached its short orbital period, as long as it occurs before $\sim$ 1 Gyr.

In our slower-rotating stellar models, an assortment of behaviors may ensue depending on the formation timescale of short-period planets. For instance, in the

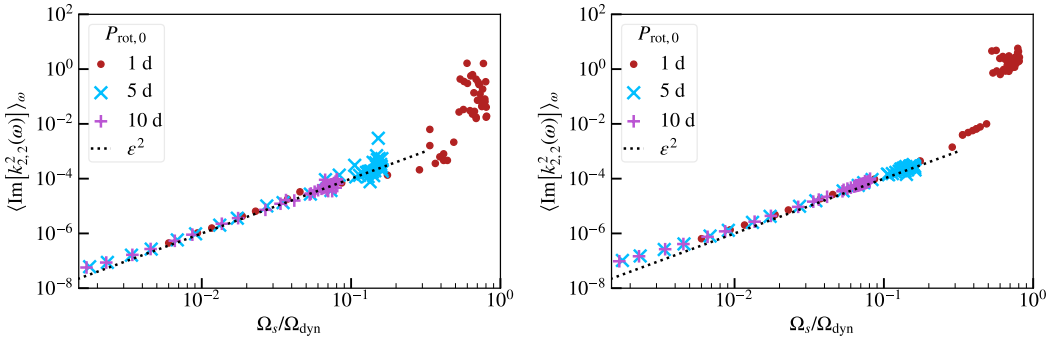

Figure 2.13: Frequency-averaged dissipation $\langle \mathrm{Im}\left[k^2_{2,2}\right]\rangle_\omega = \int_{-2\Omega_s}^{2\Omega_s} \mathrm{Im}\left[k^2_{2,2}\right] d\omega/\omega$ as in Ogilvie, 2013. The left panel shows the result for dissipation using rotationally modified viscosity $\nu_{\rm R}$ (Equation 2.26), and the right shows the result with the unmodified viscosity $\nu_{\rm NR}$ (Equation 2.21). For comparison, the scaling in black matches the prescription in Ogilvie, 2013 of $\langle \mathrm{Im}\left[k^2_{2,2}\right]\rangle_\omega \propto \epsilon^2 = (\Omega_s/\Omega_{\rm dyn})^2$.

$P_{\rm rot,0} = 5$ day set of integrations, formation theories placing planets at $P_{\rm orb,0} \lesssim 1.5$ day at stellar ages $\lesssim 50$ Myr are susceptible to resonance locking, either immediately beginning inward migration or experiencing delayed outward migration at a few 100 Myr–1 Gyr. However, if the Earth-mass planet is driven to short orbital periods at $\gtrsim 50$ Myr, the orbit may not be affected. For example, evolving a $P_{\rm orb,0} = 0.5$ day planet from 500 Myr in the $P_{\rm rot,0} = 5$ day model is too late for a resonance lock. In the $P_{\rm rot,0} = 10$ day model, the $P_{\rm orb,0} = 0.5$ day evolution initialized at 100 Myr is unable to lock into resonance, though the same evolution initialized at 10 Myr migrates inward due to resonance locking. Similar variations in behavior for different initial conditions can be observed for the $P_{\rm orb,0} = 1$–1.5 day curves in Figures 2.7.

In general, the dependence of evolutionary outcomes on the different timescales of short-period planet formation can be attributed to the variation in initial tidal forcing frequency ω_m as the stellar rotation rate changes over time. This aspect of the stellar evolution may prevent the planet from achieving the same resonance lock and enhanced migration that occurs for another initial condition. Figure 2.8 presents an analogous range in evolutionary outcomes that depend on the potential formation timescales for short-period Jupiter-mass planets, if they are found around low-mass M-dwarfs. Nevertheless, the caveat discussed in Section 2.5 for outwardly migrating Jupiter-mass planets remains relevant here.

The majority of the migration illustrated in this work occurs before a few Gyr, so

observing evidence of migration in the orbital architectures of exoplanets would be facilitated by the detection of young M-dwarf systems. In our predictions, planets with $P_{\rm orb} \lesssim 1$ day that move outward to larger $P_{\rm orb}$ often begin experiencing migration at ~ 1 Gyr. For older M-dwarf systems found at a few Gyr, these planets will have already reached larger separations and vacated the region of short-period orbits. If detected in future observations, e.g., from TESS or the Roman Space Telescope, short-period planets around M-dwarfs younger than $\lesssim 1$ Gyr likely have not yet migrated outward. As a result, we predict short-period planets to be more common around young M-dwarf systems than older M-dwarf systems.

Looking at the NASA Exoplanet Archive, we note that there are not many young, low-mass stars hosting short-period planets due to the challenges in observing planets around active young stars. Nevertheless, some young, rapidly rotating stars hosting planets at short periods such as TOI 540b (Ment et al., 2021) and K2-25b (Thao et al., 2020; Stefansson et al., 2020) are interesting candidates to undergo tidal evolution in the context of our models. In the future, we will be able to better test our model's predictions given more observations of planets around young stars. Nevertheless, to make a definitive prediction for evidence of tidal migration in the period distribution of observed exoplanet systems would require more extensive modeling than done in this work. The period distribution is shaped by combination of the physics of planet formation and the effect of tides, so it will be necessary to model both of these aspects in tandem (e.g., Lee and Chiang 2017) order to make more robust predictions in the future.

In exoplanet systems with more massive host stars, the star is not fully convective. Thus, the dynamical tide likely comprises gravito-inertial waves instead of the pure inertial modes examined in this work. For young, rapidly rotating solar type stars with planetary companions at $\lesssim 5$ day, for instance the host stars TOI 942 (Wirth et al., 2021) and WASP 25 (Bonomo et al., 2017), we do expect similar orbital dynamics due to gravito-inertial modes relative to what we discuss in this work. However, the denser spectrum of gravito-inertial modes at small frequencies will complicate the picture by involving contributions to the tidal dissipation from a larger number of normal modes. We anticipate that the rich spectrum of mode peaks will warrant detailed exploration of resonance locking effects in these systems.

Comparison to frequency-averaged dissipation

Models of similar star-planet systems in the past have relied upon a prescription for the frequency-averaged dissipation due to the dynamical tide. For instance, Gallet et al., 2017 modeled dynamical tides in stars between 0.3–1.4 $M_\odot$ based on a prescription for frequency-averaged dissipation from Ogilvie, 2013:

$$\begin{aligned}\langle \mathrm{Im}\left[k_{2,2}^2(\omega)\right]\rangle_\omega &= \int_{-2\Omega_s}^{2\Omega_s} \mathrm{Im}\left[k_{2,2}^2(\omega)\right]\frac{d\omega}{\omega} \\ &= \frac{100\pi}{63}\epsilon^2\frac{\alpha^5}{1-\alpha^5},\end{aligned} \tag{2.29}$$

where $\epsilon = \Omega_s/\Omega_{\mathrm{dyn}}$ and $\alpha = R_c/R$ is the fractional size of the radiative core. In their models, no tidal dissipation occurred during periods of the evolution where the star was fully convective because of their prescription's dependence on α. As a result, for our models where $\alpha = 0$, Equation 2.29 underestimates the amount of tidal dissipation.

We can also compare the how dissipation scales with ϵ. Figure 2.13 shows the value of $\langle \mathrm{Im}\left[k_{2,2}^2(\omega)\right]\rangle_\omega$ in our models, with the fiducial models using ν_{R} on the left, and the models with ν_{NR} on the right. We see the same scaling of ϵ^2 in our models up to values of $\epsilon \gtrsim 0.2$, where scatter begins to accumulate around the relation. This is not surprising, as the scaling was derived for slowly rotating bodies where the f-modes are well separated from the i-modes in frequency, assuming a constant dynamic viscosity (Ogilvie, 2013). The $P_{\mathrm{rot},0} = 1$ day models form a group of outliers as they encounter avoided crossings between f-modes and i-modes for $\epsilon \gtrsim 0.6$, such that the frequency range of $[-2\Omega_s, 2\Omega_s]$ includes the large f-mode dissipation. This strongly amplifies the value of the frequency-averaged dissipation. We also note that the models with ν_{NR} follow the trend more closely than models using ν_{R} because the variation of viscosity with Rossby number within the star introduces more scatter.

Compared to Figure 4 of Gallet et al., 2017, our frequency-averaged dissipation values, which represent $\alpha = 0$ in the context of their work, span a similar order-of-magnitude range of $\langle \mathrm{Im}\left[k_{2,2}^2(\omega)\right]\rangle_\omega \approx 10^{-8}$–$10^{-4}$ for $\epsilon \lesssim 0.1$. In their higher-mass models, stars achieve this level of dissipation with core sizes $\alpha \approx 0.2$–0.8 throughout the evolution. Their most similar model in terms of stellar mass is an 0.3 $M_\odot$ model which only hosts a radiative core for a few tens of Myr and correspondingly only exhibits dissipation during that period. In contrast, for our low-mass M-dwarfs that are fully convective, we predict frequency-averaged dissipation at the same level as

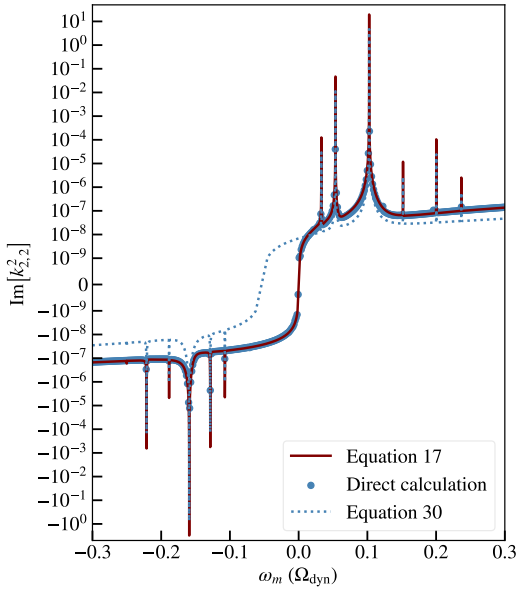

Figure 2.14: Comparison of different methods for computing the Love number, shown for a $P_{\rm rot,0} = 5$ day, $\Omega_s/\Omega_{\rm dyn} = 0.150$ model. The red solid curve shows the result of using Equations 2.14–2.17 to infer Im $\left[k_{2,2}^2\right]$, which includes dissipative mode coupling terms. The blue dots show the results from a direct forced calculation, which are nearly indistinguishable from the red line. In contrast, the dotted blue line shows the result from a sum over normal modes without dissipative coupling terms (Equation 2.30), which deviates significantly from the other two methods away from resonance.

their solar-mass models throughout the stellar lifetime. Furthermore, the goal of this work was to instead use a frequency-dependent tidal dissipation in our calculations, which reveal a variety of scenarios involving resonance locking that are not captured by an average over frequency.

Total dissipation vs. individual mode damping

Multiple approaches to calculating dissipation from the dynamical tide exist in the literature, primarily by direct calculation or by modal decomposition. The direct calculation refers to numerically solving the linearized fluid dynamics equations to find the perturbed response of a fluid under the influence of a tidal potential with forcing frequency ω_m (see, e.g., Dewberry, 2023; Ogilvie, 2013). To recover the spectrum of Im $\left[k_{2,2}^2\right]$ across forcing frequency, the calculation must be repeated at each value of ω_m. Other works use an expansion over oscillation modes, which constitutes the theoretical framework of this work (e.g., Press and Teukolsky, 1977; Kumar, Ao, and Quataert, 1995; Lai, 1997; Fuller and Lai, 2012; Fuller, 2017).

This popular approach allows for a less numerically expensive analysis that readily captures resonances with normal modes of the star.

However, Townsend and Sun, 2023 find a discrepancy between the two methods in the context of modeling secular tidal torques in binary star systems. They attribute the issue to a subtlety about expanding over normal modes: it is insufficient to consider each mode as contributing independent coefficients characterized by individual mode damping rates γ_α. For instance, works using modal decomposition typically find the Love number from the following sum (e.g., Dewberry, 2023):

$$k^n_{\ell,m} = \frac{2\pi}{2\ell+1} \sum_\alpha \frac{Q^\alpha_{\ell m} Q^\alpha_{nm}}{\epsilon_\alpha(\omega_\alpha - \omega_m - i\gamma_\alpha)}. \tag{2.30}$$

This method employs Equation 2.16 to compute the mode amplitudes.

Though we also use Equation 2.16 to calculate the mode amplitudes, we obtain coefficients in the damping integral (Equation 2.14) that couple different oscillation modes together (more details are discussed in Dewberry and Wu 2024). The discrepancy in the dissipation away from resonances as noted by Townsend and Sun, 2023 motivates us to take the approach described in Section 2.3 of inverting Equation 2.17 to find the Love number instead of using Equation 2.30.

In agreement with the inconsistency put forth by Townsend and Sun, 2023, we demonstrate in Figure 2.14 that the spectrum of $\mathrm{Im}\left[k^2_{2,2}\right]$ from Equation 2.30 diverges from the results of Equations 2.14–2.17 significantly away from resonance. In both calculations, we sum over the subset of f-modes and i-modes utilized in this work. However, Equation 2.30 (blue dotted line) can yield unphysical results. For instance, it does not cross zero at $\omega_m = 0$ with this set of modes, and the magnitude of the off-resonance dissipation is lower than what we find from our approach using the same viscosity. Figure 2.14 also verifies that our approach (red line) agrees very well with the results of a direct calculation (brown dots). Thus, the mode decomposition method can yield accurate results, but only if mode interaction cross terms due to dissipation (Equation 2.14 in this work) are included when summing over modes.

2.7 Conclusion

We have modeled the frequency-dependent tidal response throughout the pre-main sequence and main sequence evolution of fully convective stars using realistic stellar models. Using a non-perturbative spectral method that fully resolves the effects of the Coriolis force to calculate fundamental and inertial mode oscillations of the star,

we then compute the dissipation in terms of contributions from these normal modes. Our formalism accounts for the importance of viscous coupling between different modes in producing a reliable dissipation spectrum across tidal forcing frequency.

We performed our analysis for a fully convective 0.2 $M_\odot$ M-dwarf at three different initial rotation periods, one of which ($P_{\rm rot,0}$ = 1 day) rotates very quickly relative to observed cluster stars, and two of which ($P_{\rm rot,0}$ = 5 and 10 day) span a more common range of stellar rotation periods. As the star traverses the pre-main sequence and main sequence, we prescribe its spin evolution using the saturated magnetic braking model of Matt et al., 2015. The tidal response within this fully convective star is expected to be damped by a turbulent convective viscosity, which can be estimated from mixing-length theory as independent of Rossby number Ro (Equation 2.21) or modified to account for the reduced efficiency of turbulent convective viscosity at high rotation rates (Equation 2.26). Including the effects of rotation on viscosity decreases the magnitude of the viscosity in the stellar interior, leading to smaller equilibrium tidal dissipation but larger dissipation at resonances with stellar oscillation modes.

Using the formalism described in Section 2.3, we compute the spectrum of dynamical tidal dissipation across tidal forcing frequency ω_m throughout the stellar evolution. Peaks in the dissipation spectrum form at frequencies which are resonant with the star's inertial modes (i-modes) and fundamental modes (f-modes). For rapidly rotating models $\Omega_s/\Omega_{\rm dyn} \gtrsim 0.6$, avoided crossings between f-modes and i-modes greatly enhance the dissipation at tidal forcing frequencies $|\omega_m| \leq 2\Omega_s$. As the star evolves, the mode frequencies change, allowing them to sweep through resonances with orbiting planets.

We integrate the semi-major axis evolution of planets causing tidal dissipation in the host star. We find that both inward and outward orbital migration can occur for Earth-mass planets at $P_{\rm orb,0} \lesssim 1.5$ day and Jupiter-mass planets at $P_{\rm orb,0} \lesssim 2.5$ day. In general, significant migration is induced by resonance locking, whereby the planetary orbit's tidal forcing frequency resonantly excites a stellar oscillation mode and continues to closely follow this mode frequency over time. This leads to enhanced dissipation during the resonance lock by several orders of magnitude. Due to orbital migration during the first few Gyr of the star's lifetime, we predict that the region of $P_{\rm orb} \lesssim 1$ day is likely to be cleared of small planets, and giant planets are made scarce out to $P_{\rm orb} \lesssim 3$ day around fully convective M-dwarfs.

In the future, we hope to incorporate the feedback of the tidal torque on the stellar spin in our calculations, which we find to be significant for Jupiter-mass planets. This will

contextualize our expectations for resonance locking of Jupiter-mass planets, as the spin-up or spin-down of the host star will affect the mode frequencies as a function of time. Another promising next step will be to apply the formalism established in this work to higher-mass, partially convective stars. These stars will host gravito-inertial modes, which we anticipate will lead to a denser spectrum of dynamical tidal dissipation that can also drive resonance locking in planetary systems. These solar-type stars are representative of the majority of known exoplanet hosts and in particular the host star in the only planetary system whose orbit is known to decay, WASP-12b (Maciejewski et al., 2013; Maciejewski et al., 2018; Patra et al., 2017; Yee et al., 2020).

In addition, observations of exoplanet hosts in this mass range indicate that cooler stars with convective envelopes, which are often observed with spin that is aligned with their planetary orbits, may experience greater tidal dissipation than hotter stars with radiative envelopes, whose spin-orbit alignments trend larger (Albrecht et al., 2012; Albrecht et al., 2021; Winn et al., 2010; Winn and Fabrycky, 2015; Spalding and Winn, 2022). While we only considered aligned spin and orbits, our methods can easily be extended to planets with misaligned orbits to compute the tidal damping of obliquities. Studying the dynamical tide in low and high-mass stars will elucidate the puzzle of obliquity damping in these systems.

Acknowledgments

This material is based upon work supported by the National Science Foundation Graduate Research Fellowship under Grant No. DGE-1745301, and by NASA through grant 20-XRP20 2-0147.

References

Albrecht, S. et al. (Sept. 2012). "Obliquities of Hot Jupiter Host Stars: Evidence for Tidal Interactions and Primordial Misalignments". In: *ApJ* 757.1, p. 18. DOI: 10.1088/0004-637X/757/1/18.

Albrecht, S. H. et al. (July 2021). "A Preponderance of Perpendicular Planets". In: *ApJL* 916.1, p. L1. DOI: 10.3847/2041-8213/ac0f03.

Bailey, A. and J. Goodman (Jan. 2019). "Understanding WASP-12b". In: *MNRAS* 482.2, pp. 1872–1882. DOI: 10.1093/mnras/sty2805.

Barker, A. J. (Sept. 2020). "Tidal dissipation in evolving low-mass and solar-type stars with predictions for planetary orbital decay". In: *Monthly Notices of the Royal Astronomical Society* 498.2, pp. 2270–2294. ISSN: 0035-8711. DOI: 10.1093/mnras/staa2405.

Barker, A. J., A. M. Dempsey, and Y. Lithwick (Aug. 2014). "Theory and Simulations of Rotating Convection". In: *ApJ* 791.1, p. 13. DOI: 10.1088/0004-637X/791/1/13.

Bolmont, E. et al. (Aug. 2017). "Tidal dissipation in rotating low-mass stars and implications for the orbital evolution of close-in massive planets. II. Effect of stellar metallicity". In: *A&A* 604, A113. DOI: 10.1051/0004-6361/201730662.

Bolmont, E. and S. Mathis (Nov. 2016). "Effect of the rotation and tidal dissipation history of stars on the evolution of close-in planets". In: *Celestial Mechanics and Dynamical Astronomy* 126.1-3, pp. 275–296. DOI: 10.1007/s10569-016-9690-3.

Bonomo, A. S. et al. (June 2017). "The GAPS Programme with HARPS-N at TNG . XIV. Investigating giant planet migration history via improved eccentricity and mass determination for 231 transiting planets". In: *A&A* 602, A107. DOI: 10.1051/0004-6361/201629882.

Braviner, H. J. and G. I. Ogilvie (Feb. 2015). "Tidal interactions of a Maclaurin spheroid - II. Resonant excitation of modes by a close, misaligned orbit". In: *MNRAS* 447.2, pp. 1141–1153. DOI: 10.1093/mnras/stu2521.

Burkart, J. et al. (Apr. 2012). "Tidal asteroseismology: Kepler's KOI-54". In: *MNRAS* 421.2, pp. 983–1006. DOI: 10.1111/j.1365-2966.2011.20344.x.

Dawson, R. I. and J. A. Johnson (Sept. 2018). "Origins of Hot Jupiters". In: *ARA&A* 56, pp. 175–221. DOI: 10.1146/annurev-astro-081817-051853.

Dewberry, J. W. (June 2023). "Dynamical tides in Jupiter and other rotationally flattened planets and stars with stable stratification". In: *MNRAS* 521.4, pp. 5991–6004. DOI: 10.1093/mnras/stad546.

Dewberry, J. W. and D. Lai (Feb. 2022). "Dynamical Tidal Love Numbers of Rapidly Rotating Planets and Stars". In: *ApJ* 925.2, p. 124. DOI: 10.3847/1538-4357/ac3ede.

Dewberry, J. W. and S. C. Wu (Jan. 2024). "On the damping of tidally driven oscillations". In: *MNRAS* 527.2, pp. 2288–2296. DOI: 10.1093/mnras/stad3164.

Dewberry, J. W. et al. (Sept. 2021). "Constraining Saturn's Interior with Ring Seismology: Effects of Differential Rotation and Stable Stratification". In: *The Planetary Science Journal* 2.5, p. 198. DOI: 10.3847/PSJ/ac0e2a.

Dressing, C. D. and D. Charbonneau (Apr. 2013). "The Occurrence Rate of Small Planets around Small Stars". In: *ApJ* 767.1, p. 95. DOI: 10.1088/0004-637X/767/1/95.

Duguid, C. D., A. J. Barker, and C. A. Jones (Sept. 2020). "Convective turbulent viscosity acting on equilibrium tidal flows: new frequency scaling of the effective viscosity". In: *MNRAS* 497.3, pp. 3400–3417. DOI: 10.1093/mnras/staa2216.

Duguid, C. D., A. J. Barker, and C. A. Jones (Jan. 2020). “Tidal flows with convection: frequency dependence of the effective viscosity and evidence for antidissipation”. In: *MNRAS* 491.1, pp. 923–943. DOI: 10.1093/mnras/stz2899.

Fuller, J. (Sept. 2017). “Pre-supernova outbursts via wave heating in massive stars - I. Red supergiants”. In: *MNRAS* 470.2, pp. 1642–1656. DOI: 10.1093/mnras/stx1314.

Fuller, J. and D. Lai (Mar. 2012). “Dynamical tides in eccentric binaries and tidally excited stellar pulsations in Kepler KOI-54”. In: *MNRAS* 420.4, pp. 3126–3138. DOI: 10.1111/j.1365-2966.2011.20237.x.

Fuller, J., J. Luan, and E. Quataert (June 2016). “Resonance locking as the source of rapid tidal migration in the Jupiter and Saturn moon systems”. In: *MNRAS* 458.4, pp. 3867–3879. DOI: 10.1093/mnras/stw609.

Gallet, F. et al. (Aug. 2017). “Tidal dissipation in rotating low-mass stars and implications for the orbital evolution of close-in planets. I. From the PMS to the RGB at solar metallicity”. In: *A&A* 604, A112. DOI: 10.1051/0004-6361/201730661.

Gillon, M. et al. (Feb. 2017). “Seven temperate terrestrial planets around the nearby ultracool dwarf star TRAPPIST-1”. In: *Nature* 542.7642, pp. 456–460. DOI: 10.1038/nature21360.

Goldreich, P. and D. A. Keeley (Feb. 1977). “Solar seismology. I. The stability of the solar p-modes.” In: *ApJ* 211, pp. 934–942. DOI: 10.1086/155005.

Goodman, J. and C. Lackner (May 2009). “Dynamical Tides in Rotating Planets and Stars”. In: *ApJ* 696.2, pp. 2054–2067. DOI: 10.1088/0004-637X/696/2/2054.

Goodman, J. and S. P. Oh (Sept. 1997). “Fast Tides in Slow Stars: The Efficiency of Eddy Viscosity”. In: *ApJ* 486.1, pp. 403–412. DOI: 10.1086/304505.

Hsu, D. C., E. B. Ford, and R. Terrien (Oct. 2020). “Occurrence rates of planets orbiting M Stars: applying ABC to Kepler DR25, Gaia DR2, and 2MASS data”. In: *MNRAS* 498.2, pp. 2249–2262. DOI: 10.1093/mnras/staa2391.

Ipser, J. R. and L. Lindblom (May 1991). “The Oscillations of Rapidly Rotating Newtonian Stellar Models. II. Dissipative Effects”. In: *ApJ* 373, p. 213. DOI: 10.1086/170039.

Kumar, P., C. O. Ao, and E. J. Quataert (Aug. 1995). “Tidal Excitation of Modes in Binary Systems with Applications to Binary Pulsars”. In: *ApJ* 449, p. 294. DOI: 10.1086/176055.

Lai, D. (Dec. 1997). “Dynamical Tides in Rotating Binary Stars”. In: *ApJ* 490.2, pp. 847–862. DOI: 10.1086/304899.

Lai, D. and Y. Wu (July 2006). “Resonant tidal excitations of inertial modes in coalescing neutron star binaries”. In: *PhRvD* 74.2, p. 024007. DOI: 10.1103/PhysRevD.74.024007.

Lee, E. J. and E. Chiang (June 2017). "Magnetospheric Truncation, Tidal Inspiral, and the Creation of Short-period and Ultra-short-period Planets". In: *ApJ* 842.1, p. 40. DOI: 10.3847/1538-4357/aa6fb3.

Maciejewski, G. et al. (Mar. 2013). "Multi-site campaign for transit timing variations of WASP-12 b: possible detection of a long-period signal of planetary origin". In: *A&A* 551, A108. DOI: 10.1051/0004-6361/201220739.

Maciejewski, G. et al. (Dec. 2018). "Planet-Star Interactions with Precise Transit Timing. I. The Refined Orbital Decay Rate for WASP-12 b and Initial Constraints for HAT-P-23 b, KELT-1 b, KELT-16 b, WASP-33 b and WASP-103 b". In: *AcA* 68.4, pp. 371–401. DOI: 10.32023/0001-5237/68.4.4.

Mathis, S. et al. (July 2016). "The impact of rotation on turbulent tidal friction in stellar and planetary convective regions". In: *A&A* 592, A33. DOI: 10.1051/0004-6361/201527545.

Matt, S. P. et al. (Jan. 2015). "The Mass-dependence of Angular Momentum Evolution in Sun-like Stars". In: *ApJL* 799.2, p. L23. DOI: 10.1088/2041-8205/799/2/L23.

Ment, K. and D. Charbonneau (June 2023). "The Occurrence Rate of Terrestrial Planets Orbiting Nearby Mid-to-late M Dwarfs from TESS Sectors 1-42". In: *AJ* 165.6, p. 265. DOI: 10.3847/1538-3881/acd175.

Ment, K. et al. (Jan. 2021). "TOI 540 b: A Planet Smaller than Earth Orbiting a Nearby Rapidly Rotating Low-mass Star". In: *AJ* 161.1, p. 23. DOI: 10.3847/1538-3881/abbd91.

Mulders, G. D., I. Pascucci, and D. Apai (Jan. 2015). "A Stellar-mass-dependent Drop in Planet Occurrence Rates". In: *ApJ* 798.2, p. 112. DOI: 10.1088/0004-637X/798/2/112.

Ogilvie, G. I. and D. N. C. Lin (June 2007). "Tidal Dissipation in Rotating Solar-Type Stars". In: *ApJ* 661.2, pp. 1180–1191. DOI: 10.1086/515435.

Ogilvie, G. I. (Feb. 2013). "Tides in rotating barotropic fluid bodies: the contribution of inertial waves and the role of internal structure". In: *MNRAS* 429.1, pp. 613–632. DOI: 10.1093/mnras/sts362.

Ogilvie, G. I. (Aug. 2014). "Tidal Dissipation in Stars and Giant Planets". In: *ARA&A* 52, pp. 171–210. DOI: 10.1146/annurev-astro-081913-035941.

Ogilvie, G. I. and G. Lesur (May 2012). "On the interaction between tides and convection". In: *MNRAS* 422.3, pp. 1975–1987. DOI: 10.1111/j.1365-2966.2012.20630.x.

Patra, K. C. et al. (July 2017). "The Apparently Decaying Orbit of WASP-12b". In: *AJ* 154.1, p. 4. DOI: 10.3847/1538-3881/aa6d75.

Paxton, B. et al. (Jan. 2011). "Modules for Experiments in Stellar Astrophysics (MESA)". In: *ApJS* 192, p. 3. DOI: 10.1088/0067-0049/192/1/3.

Paxton, B. et al. (Sept. 2013). "Modules for Experiments in Stellar Astrophysics (MESA): Planets, Oscillations, Rotation, and Massive Stars". In: *ApJS* 208.1, p. 4. DOI: 10.1088/0067-0049/208/1/4.

Paxton, B. et al. (Sept. 2015). "Modules for Experiments in Stellar Astrophysics (MESA): Binaries, Pulsations, and Explosions". In: *ApJS* 220.1, p. 15. DOI: 10.1088/0067-0049/220/1/15.

Paxton, B. et al. (Feb. 2018). "Modules for Experiments in Stellar Astrophysics (MESA): Convective Boundaries, Element Diffusion, and Massive Star Explosions". In: *ApJS* 234.2, p. 34. DOI: 10.3847/1538-4365/aaa5a8.

Paxton, B. et al. (July 2019). "Modules for Experiments in Stellar Astrophysics (MESA): Pulsating Variable Stars, Rotation, Convective Boundaries, and Energy Conservation". In: *ApJS* 243.1, p. 10. DOI: 10.3847/1538-4365/ab2241.

Penev, K., J. Barranco, and D. Sasselov (Nov. 2009). "Direct Calculation of the Turbulent Dissipation Efficiency in Anelastic Convection". In: *ApJ* 705.1, pp. 285–297. DOI: 10.1088/0004-637X/705/1/285.

Penev, K. et al. (Feb. 2007). "On Dissipation inside Turbulent Convection Zones from Three-dimensional Simulations of Solar Convection". In: *ApJ* 655.2, pp. 1166–1171. DOI: 10.1086/507937.

Press, W. H. and S. A. Teukolsky (Apr. 1977). "On formation of close binaries by two-body tidal capture." In: *ApJ* 213, pp. 183–192. DOI: 10.1086/155143.

Rodríguez Martínez, R. et al. (Oct. 2023). "A Comparison of the Composition of Planets in Single-planet and Multiplanet Systems Orbiting M dwarfs". In: *AJ* 166.4, p. 137. DOI: 10.3847/1538-3881/aced9a.

Schenk, A. K. et al. (Dec. 2001). "Nonlinear mode coupling in rotating stars and the r-mode instability in neutron stars". In: *PhRvD* 65.2, p. 024001. DOI: 10.1103/PhysRevD.65.024001.

Spalding, C. and J. N. Winn (Mar. 2022). "Tidal Erasure of Stellar Obliquities Constrains the Timing of Hot Jupiter Formation". In: *ApJ* 927.1, p. 22. DOI: 10.3847/1538-4357/ac4993.

Stefansson, G. et al. (Oct. 2020). "The Habitable Zone Planet Finder Reveals a High Mass and Low Obliquity for the Young Neptune K2-25b". In: *AJ* 160.4, p. 192. DOI: 10.3847/1538-3881/abb13a.

Stevenson, D. J. (Jan. 1979). "Turbulent thermal convection in the presence of rotation and a magnetic field: A heuristic theory". In: *Geophysical and Astrophysical Fluid Dynamics* 12.1, pp. 139–169. DOI: 10.1080/03091927908242681.

Tamburo, P., P. S. Muirhead, and C. D. Dressing (June 2023). "Predicting the Yield of Small Transiting Exoplanets around Mid-M and Ultracool Dwarfs in the Nancy Grace Roman Space Telescope Galactic Bulge Time Domain Survey". In: *AJ* 165.6, p. 251. DOI: 10.3847/1538-3881/acd1de.

Terquem, C. (June 2021). “On a new formulation for energy transfer between convection and fast tides with application to giant planets and solar type stars”. In: *MNRAS* 503.4, pp. 5789–5806. DOI: 10.1093/mnras/stab224.

Terquem, C. (Oct. 2023). “On the energetics of a tidally oscillating convective flow”. In: *MNRAS* 525.1, pp. 508–526. DOI: 10.1093/mnras/stad2163.

Thao, P. C. et al. (Jan. 2020). “Zodiacal Exoplanets in Time (ZEIT). IX. A Flat Transmission Spectrum and a Highly Eccentric Orbit for the Young Neptune K2-25b as Revealed by Spitzer”. In: *AJ* 159.1, p. 32. DOI: 10.3847/1538-3881/ab579b.

Townsend, R. H. D. and M. Sun (Aug. 2023). “Discrepant Approaches to Modeling Stellar Tides and the Blurring of Pseudosynchronization”. In: *ApJ* 953.1, p. 48. DOI: 10.3847/1538-4357/acdd5a.

Vick, M. and D. Lai (Aug. 2020). “Tidal evolution of eccentric binaries driven by convective turbulent viscosity”. In: *MNRAS* 496.3, pp. 3767–3780. DOI: 10.1093/mnras/staa1784.

Weinberg, N. N. et al. (June 2012). “Nonlinear Tides in Close Binary Systems”. In: *ApJ* 751.2, p. 136. DOI: 10.1088/0004-637X/751/2/136.

Weinberg, N. N. et al. (Nov. 2017). “Tidal Dissipation in WASP-12”. In: *ApJL* 849.1, p. L11. DOI: 10.3847/2041-8213/aa9113.

Winn, J. N. and D. C. Fabrycky (Aug. 2015). “The Occurrence and Architecture of Exoplanetary Systems”. In: *ARA&A* 53, pp. 409–447. DOI: 10.1146/annurev-astro-082214-122246.

Winn, J. N. et al. (Aug. 2010). “Hot Stars with Hot Jupiters Have High Obliquities”. In: *ApJL* 718.2, pp. L145–L149. DOI: 10.1088/2041-8205/718/2/L145.

Wirth, C. P. et al. (Aug. 2021). “TOI-942b: A Prograde Neptune in a 60 Myr Old Multi-transiting System”. In: *ApJL* 917.2, p. L34. DOI: 10.3847/2041-8213/ac13a9.

Witte, M. G. and G. J. Savonije (Oct. 1999). “Tidal evolution of eccentric orbits in massive binary systems. A study of resonance locking”. In: *A&A* 350, pp. 129–147. DOI: 10.48550/arXiv.astro-ph/9909073.

Wu, Y. (Dec. 2005). “Origin of Tidal Dissipation in Jupiter. I. Properties of Inertial Modes”. In: *ApJ* 635.1, pp. 674–687. DOI: 10.1086/497354.

Wu, Y. (Dec. 2005). “Origin of Tidal Dissipation in Jupiter. II. The Value of Q”. In: *ApJ* 635.1, pp. 688–710. DOI: 10.1086/497355.

Yee, S. W. et al. (Jan. 2020). “The Orbit of WASP-12b Is Decaying”. In: *ApJL* 888.1, p. L5. DOI: 10.3847/2041-8213/ab5c16.

Zahn, J. P. (Feb. 1966). “Les marées dans une étoile double serrée”. In: *Annales d’Astrophysique* 29, p. 313.

Zahn, J. P. (Feb. 1966). “Les marées dans une étoile double serrée (suite)”. In: *Annales d’Astrophysique* 29, p. 489.

Chapter 3

A DIVERSITY OF WAVE-DRIVEN PRE-SUPERNOVA OUTBURSTS

Wu, S. C. and J. Fuller (Jan. 2021). "A Diversity of Wave-driven Presupernova Outbursts". In: *The Astrophysical Journal* 906.1, p. 3. DOI: 10.3847/1538-4357/abc87c.

3.1 Abstract

Many core-collapse supernova progenitors show indications of enhanced pre-supernova (SN) mass loss and outbursts, some of which could be powered by wave energy transport within the progenitor star. Depending on the star's structure, convectively excited waves driven by late stage nuclear burning can carry substantial energy from the core to the envelope, where the wave energy is dissipated as heat. We examine the process of wave energy transport in single-star SNe progenitors with masses between 11–50 $M_\odot$. Using MESA stellar evolution simulations, we evolve stars until core collapse and calculate the wave power produced and transmitted to the stars' envelopes. These models improve upon prior efforts by incorporating a more realistic wave spectrum and non-linear damping effects, reducing our wave heating estimates by ~ 1 order of magnitude compared to prior work. We find that waves excited during oxygen/neon burning typically transmit $\sim 10^{46–47}$ erg of energy at $0.1 - 10$ years before core collapse in typical ($M < 30\,M_\odot$) SN progenitors. High-mass progenitors can often transmit $\sim 10^{47–48}$ erg of energy during oxygen/neon burning, but this tends to occur later, at about $0.01 - 0.1$ years before core collapse. Pre-SN outbursts may be most pronounced in low-mass SN progenitors ($M \lesssim 12\,M_\odot$) undergoing semi-degenerate neon ignition, and in high-mass progenitors ($M \gtrsim 30\,M_\odot$) exhibiting convective shell mergers.

3.2 Introduction

Evidence continues to mount that a substantial fraction of core-collapse supernovae (SNe) are preceded by greatly elevated mass loss rates from their progenitor stars. In most cases, this is inferred from SN observations that reveal large amounts of circumstellar material (CSM) very close (within $\sim 10^{15}$ cm) to the progenitor star, which is not predicted by standard stellar and wind models. The CSM is usually

manifested by faster rise times and brighter early-time SN light curves, or by blue and featureless early spectra indicative of a shock heated envelope or CSM. Narrow flash-ionized emission lines are sometimes seen in the early spectra and then disappear, and they are thought to be produced by confined CSM which is then swept up by the SN ejecta.

Recent examples of SNe with evidence for early interaction include type II SNe such as SN2016bkv (Nakaoka et al., 2018), SN2018zd (Zhang et al., 2020), and many others (Khazov et al., 2016; Förster et al., 2018); and type I SNe such as LSQ13abf (Stritzinger et al., 2020), LSQ13ddu (Clark et al., 2020), SN2018bgv and SN2018don (Lunnan et al., 2020), SN2018gep (Ho et al., 2019), SN2019dge (Yao et al., 2020), SN2019uo (Gangopadhyay et al., 2020). These SNe extend across virtually all spectroscopic classes of SNe (including type II-P, II-L, IIn, Ib, Ic, Ibn, Ic-BL, superluminous Ic, etc.). There are many other SNe that show narrow emission lines and late-time interaction, such as SN2004dk (Mauerhan et al., 2018; Pooley et al., 2019), SN 2010bt (Elias-Rosa et al., 2018b), SN2012ab (Bilinski et al., 2018), SNhunt151 (Elias-Rosa et al., 2018a), SN2013L (Taddia et al., 2020), ASASSN-15no (Benetti et al., 2018), iPTF16eh (Lunnan et al., 2018), SN2017dio (Kuncarayakti et al., 2018), and SN2017ens (Chen et al., 2018), indicative of extreme pre-SN mass loss occurring ~decades before the SN.

The list above includes only events from the last three years, and many others are listed in Fuller (2017) and Fuller and Ro (2018). In several SNe, pre-SN outbursts have been observed directly, and Ofek et al. (2014) find that the majority of type IIn SNe exhibit bright ($L \gtrsim 3 \times 10^7\ L_\odot$) outbursts in the final months of their lives.

However, it is also important to note that many (perhaps the majority) of SN progenitors do not exhibit pre-SN outbursts or amplified pre-SN variability. Johnson, Kochanek, and Adams (2017) found no significant variability of the progenitor of type Ic SN2012fh, and Johnson, Kochanek, and Adams (2018) found variability amplitudes less than ~10% for four type II-P SN progenitors. Kochanek et al. (2017) examined some of the best available progenitor constraints for several well studied nearby SNe, finding no evidence for outbursts.

One should also note that for type II SN with early peaks in their light curves, the CSM is not necessarily related to elevated levels of mass loss, but could instead be produced by moderate amounts of mass ($M \lesssim 1\ M_\odot$) in an optically thin stellar chromosphere or corona (Dessart, Hillier, and Audit, 2017; Hillier and Dessart, 2019) that is not included in standard stellar models.

The inevitable conclusion reached from these observations is that the massive star progenitors of SNe are diverse, with some presenting bright pre-SN outbursts, others exhibiting elevated levels of mass loss, and many more demonstrating no unusual behavior at all. A successful physical explanation for elevated pre-SN mass loss must account for this diversity.

One compelling model for at least some pre-SN outbursts is the wave heating model of Quataert and Shiode (2012). Vigorous core convection (often carrying more than $10^9\,L_\odot$) excites internal gravity waves (IGW) that couple with acoustic waves to deposit a small fraction of this power in the outer layers of the star, which can be sufficient to eject mass or drive an observable outburst. Shiode and Quataert (2014) examined approximate wave heating energetics and time scales in a suite of models and found larger amounts of wave heating in more massive stars, whose outbursts occur closer to core-collapse.

Fuller (2017) examined the consequences of wave heating in a $15\,M_\odot$ red supergiant star, finding that waves can inflate the envelopes and possibly drive mass loss through a secondary shock. In compact hydrogen-poor stars, Fuller and Ro (2018) found that wave heat can launch a dense super-Eddington wind carrying more than $10^{-2}\,M_\odot$/yr. Both studies predicted large changes in luminosity and temperature during phases of enhanced mass loss, although the outburst luminosities in those works did not reach the level of $\sim 3 \times 10^7 L_\odot$ seen in type IIn progenitors (Ofek et al., 2014).

However, the amount of wave heat deposited in the envelope is sensitive to the wave spectrum excited by convection, to non-linear wave breaking effects, and to the rapidly evolving core structure. Most prior work has not simultaneously accounted for all of these effects to predict the wave heating rate as a function of time. In this paper, we improve upon prior work through a more complete modeling of the physics at play, applying these calculations to a suite of stars extending over the mass range $M_{ZAMS} = 11 - 50\,M_\odot$. We find that wave heating rates have been overestimated in some prior work and are not high enough to produce large outbursts in most stars. Interestingly, however, we find that wave-driven outbursts are likely to be most energetic and most prevalent in the lowest and highest-mass SN progenitors.

3.3 Implementation of wave physics in stellar models

Wave generation and propagation

To implement wave energy transport, we follow the same basic procedure as Fuller (2017) and Fuller and Ro (2018), which is largely based on the initial work of

Model	12 $M_\odot$	40 $M_\odot$
$L_{\rm con}$	$\sim 5 \times 10^9 L_\odot$	$\sim 10^{10} L_\odot$
$\mathcal{M}_{\rm con}$	~ 0.03	~ 0.04
$f_{{\rm esc},\ell=1}$	~ 0.7	~ 0.7
$f_{{\rm esc},\ell=2}$	~ 0.2	~ 0.1
$f_{{\rm esc},\ell=3}$	~ 0.05	~ 0.01
Accumulated $E_{\rm heat}$	$\sim 10^{47}$ erg	$\sim 2 \times 10^{47}$ erg
$t_{\rm prop,g}$	hours	hours
Global $t_{\rm dyn}$	months	months
$t_{\rm burn,O/Ne}$	~ 6 yr	months
$t_{\rm burn,Si}$	weeks	days
$t_{\rm prop,SN}$	~ 15 hr	~ 15 hr

Table 3.1: Order-of-magnitude values of some relevant properties and timescales that describe the wave heating phenomenon in two fiducial models, a low-mass $12\,M_\odot$ and a high-mass $40\,M_\odot$ model. For wave heating due to O/Ne burning phases, we compare the convective luminosity, convective Mach number, and escape fraction for angular wavenumbers $\ell = 1$, 2, and 3 (Equation 3.14). We also list the accumulated wave energy at $\sim$ 1 day before core collapse (Equation 3.21), the propagation timescale for gravity waves, the global dynamical time for a red supergiant, the timescales of O/Ne and Si burning, and the timescale for SN shock propagation.

Quataert and Shiode (2012) and Shiode and Quataert (2014). We calculate the wave heating rates, but do not simulate the impact of wave heating on the stellar structure.

To provide a qualitative description of the wave heating phenomenon, we list some order-of-magnitude estimates of relevant quantities and timescales for two fiducial models, a low-mass $12\,M_\odot$ model and a high-mass $40\,M_\odot$ model in Table 3.1. When appropriate, quantities are estimated during oxygen/neon (O/Ne) burning phases, which we ultimately find to contribute most significantly to wave heating.

As we explain in more detail below, the waves will initially propagate as gravity waves through the core on a timescale $t_{\rm prop,g} \sim r/v_g$ (Equation 3.7). In both models, the waves have plenty of time to escape the core because $t_{\rm prop,g} \ll t_{\rm burn,O/Ne}$ and $t_{\rm prop,g} \ll t_{\rm burn,Si}$, where $t_{\rm burn,O/Ne}$ and $t_{\rm burn,Si}$ are defined as the time until core collapse when O/Ne and Si ignite. Once waves reach the envelope, they propagate as acoustic waves on approximately the global dynamical timescale of the star $t_{\rm dyn} \sim (G\rho)^{-1/2}$. Since $t_{\rm burn,O/Ne}$, $t_{\rm burn,Si} < t_{\rm dyn}$ in the high-mass model, an outburst in high-mass supergiants is unlikely. However, in a stripped SN progenitor, the absence of envelope shortens $t_{\rm dyn}$ to minutes, making outbursts much more

promising. We have also provided the timescale for SN shock propagation after core collapse for a red supergiant, $t_{\rm prop,SN} \sim R/v_{\rm ej}$, assuming $v_{\rm ej} \sim 10^9$ cm/s; it is small compared to the timescale of acoustic wave propagation in our supergiant models.

Gravity waves are excited at the interface between convective and radiative zones and carry a fraction of the kinetic energy of turbulent convection. While convective wave excitation is not totally understood, it is generally agreed that the power put into waves, $L_{\rm wave}$, is at least

$$L_{\rm wave} = \mathcal{M}_{\rm con} L_{\rm con} \tag{3.1}$$

where $\mathcal{M}_{\rm con}$ is the MLT (mixing-length theory) convective Mach number and $L_{\rm con}$ is the convective luminosity (Goldreich and Kumar, 1990). In fact, (Lecoanet and Quataert, 2013) predict a somewhat higher flux, depending on the details of the radiative convective interface. We define the convective velocity $v_{\rm con}$ as

$$v_{\rm con} = \left(\frac{L_{\rm con}}{4\pi\rho r^2}\right)^{1/3}, \tag{3.2}$$

and we define the associated MLT convective turnover frequency as

$$\omega_{\rm con} = 2\pi \frac{v_{\rm con}}{2\alpha_{\rm MLT} H}, \tag{3.3}$$

where $\alpha_{\rm MLT} H$ is the mixing length and H is the scale height.

At the excitation region, energy is supplied to gravity waves in a power spectrum over frequency and angular wavenumber ℓ, whose details remain poorly understood. We adopt the spectrum from (Goldreich and Kumar, 1990; Shiode et al., 2013):

$$\begin{aligned}\frac{d\dot{E}_g}{d\ln\omega d\ln\ell} \sim L_{\rm wave} &\left(\frac{\omega}{\omega_{\rm con}}\right)^{-a} \left(\frac{\ell}{\ell_{\rm con}}\right)^{b+1} \left(1+\frac{\ell}{\ell_{\rm con}}\right) \\ &\times \exp\left[-\left(\frac{\ell}{\ell_{\rm con}}\right)^2 \left(\frac{\omega}{\omega_{\rm con}}\right)^{-3}\right].\end{aligned} \tag{3.4}$$

Here, $\ell_{\rm con} = r/H$ is evaluated at the edge of the convective zone and the predicted exponents are $a = 13/2$ and $b = 2$. We simplify the calculation by setting $\omega = \omega_{\rm con}$ for all ℓ values.

In case the scale height H is larger than the size of the convective zone Δr, we take $\ell_{\rm con} = r/\min(\Delta r, H)$. The proportion of wave energy generation per ℓ value, $\dot{E}_\ell/L_{\rm wave}$, can be calculated using this power spectrum, which we normalize to Equation 3.1, i.e., we set $\sum \dot{E}_\ell = L_{\rm wave}$.

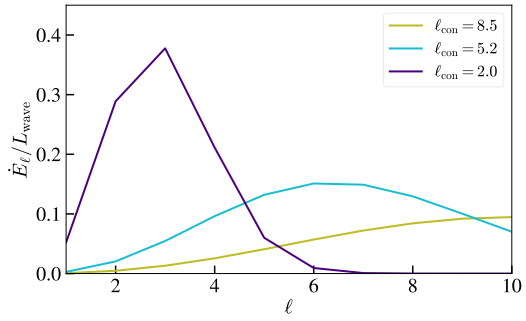

Figure 3.1: Fraction of wave energy generation per ℓ value $\dot{E}_\ell / L_{\rm wave}$, shown for representative values of $\ell_{\rm con} = r/\min(\Delta r, H)$. Large values of $\ell_{\rm con}$ represent thin convective shells and vice versa. We find $\ell_{\rm con} \sim 2$–4 for core O/Ne and Si burning, while He shell burning in our higher mass models can exhibit values as high as $\ell_{\rm con} \approx 8$.

In the WKB limit, waves that remain linear have the dispersion relation

$$k_r^2 = \frac{(N^2 - \omega_{\rm wave}^2)(L_\ell^2 - \omega_{\rm wave}^2)}{\omega_{\rm wave}^2 c_s^2}, \tag{3.5}$$

where N^2 is the squared Brunt-Väisälä frequency, k_r is the radial wavenumber, and $L_\ell^2 = \ell(\ell+1)c_s^2/r^2$ is the Lamb frequency squared. In the limit that $\omega_{\rm wave} \ll N, L_\ell$, this reduces to the gravity wave dispersion relation

$$k_r^2 = \frac{\ell(\ell+1)N^2}{\omega_{\rm wave}^2 r^2} \tag{3.6}$$

with group velocity

$$v_g = \omega_{\rm wave}^2 r / \sqrt{\ell(\ell+1)N^2}. \tag{3.7}$$

The limit $\omega_{\rm wave} \gg N, L_\ell$ gives acoustic waves, with dispersion relation

$$k_r^2 = \frac{\omega_{\rm wave}^2}{c_s^2} \tag{3.8}$$

and group velocity $v_g = c_s$. In either of these limits, linear waves propagate freely and approximately conserve their luminosity, apart from damping effects discussed below.

If $\omega_{\rm wave} > N$ and $\omega_{\rm wave} < L_\ell$ or vice versa, then the radial wavenumber is imaginary and waves are evanescent. The probability of tunneling through this evanescent zone, or the fraction of transmitted wave energy, is approximately given by the transmission coefficient

$$T^2 = \exp\left(-2\int_{r_0}^{r_1} |k_r| dr\right), \tag{3.9}$$

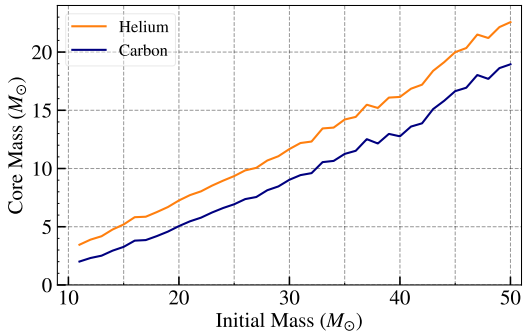

Figure 3.2: The helium (He) core mass (orange) and carbon (C) core mass (blue) as a function of initial progenitor mass for our models.

where the integral is taken over the evanescent zone. In practice, waves sometimes encounter multiple evanescent zones and the thickest evanescent zone dominates the wave reflection (see Appendix B2 of Fuller 2017). To calculate the wave flux tunneling into the envelope, we thus take the minimum value of T^2 out of all evanescent zones (i.e., the thickest evanescent region), $T^2_{\rm min}$. The remaining fraction $1 - T^2$ of wave energy that encounters the evanescent region is reflected from the boundary of the evanescent zone.

The fraction of wave energy that escapes the core, $f_{\rm esc}$, is determined by the transmission coefficient (Equation 3.9) and energy losses within the core. Neutrino emission attenuates the net energy flux escaping from the g-mode cavity, and the local neutrino wave damping rate is given by

$$\gamma_\nu = \frac{\Gamma_1^2 \nabla_{\rm ad}^2 g^2}{N^2 c_s^4} \left(\frac{\partial \ln \epsilon_\nu}{\partial \ln T} \right)_\rho \epsilon_\nu, \tag{3.10}$$

where all quantities are as defined in Appendix B of Fuller (2017). Gravity waves are also damped by the diffusion of photons, and the thermal damping rate is given by

$$\gamma_{\rm rad} \simeq k_r^2 K, \tag{3.11}$$

where

$$K = \frac{16 \sigma_{SB} T^3}{3 \rho^2 c_p \kappa} \tag{3.12}$$

is the thermal diffusivity.

As a result, after traversing to the upper edge of the core and back, a wave's energy is attenuated by the factor

$$f_\nu = e^{x_\nu} = \exp \left[2 \int_{r_-}^{r_+} \frac{\gamma_\nu + \gamma_{\rm rad}}{v_g} dr \right] \tag{3.13}$$

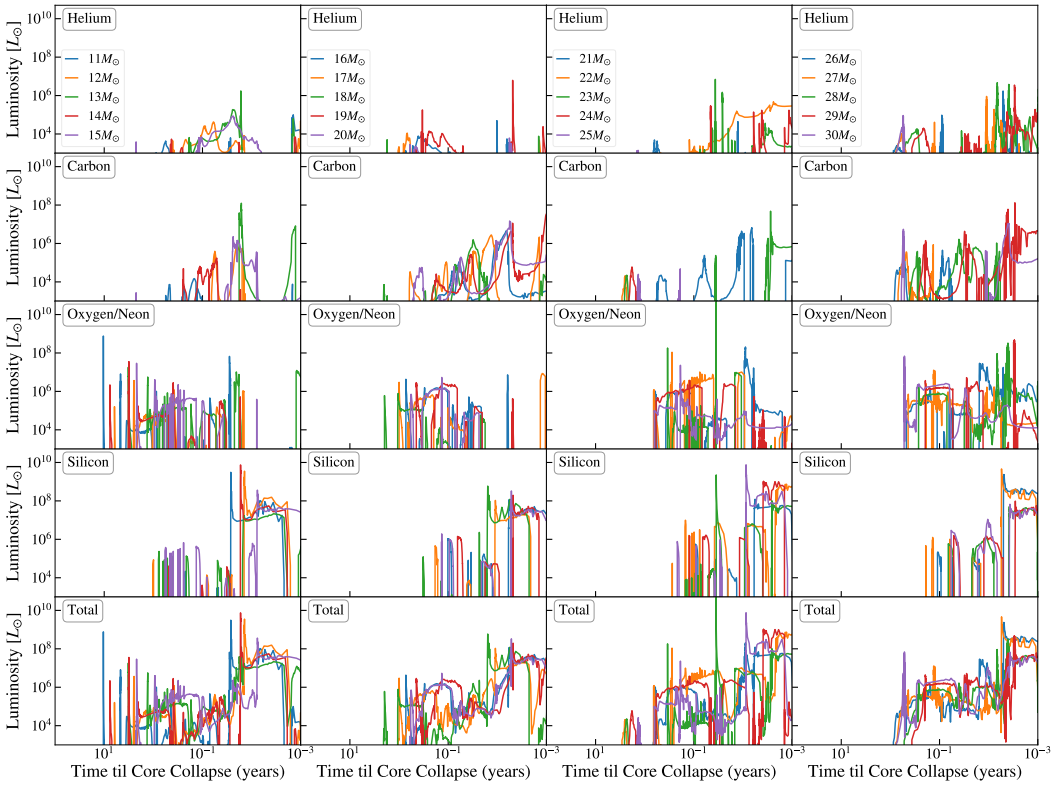

Figure 3.3: Wave heating luminosity for models with initial mass in the range 11–30 $M_\odot$, grouped into columns by mass. Element labels in each row refer to the type of burning occurring in the convective region that generates the waves. Sharp spikes in wave heating luminosity typically occur at the ignition of a new burning phase or during a convective shell merger (Section 3.4).

where v_g is the gravity wave group velocity (Equation 3.7) and the integral is taken over the upper and lower boundaries of the gravity wave cavity. Then the escape fraction is

$$f_{\mathrm{esc},\ell} = \left(1 + \frac{f_\nu - 1}{T_{\mathrm{min}}^2}\right)^{-1}. \tag{3.14}$$

and the ℓ-dependent power that escapes to heat the envelope is

$$L_{\mathrm{heat},\ell} = f_{\mathrm{esc},\ell}\dot{E}_\ell. \tag{3.15}$$

Another source of energy loss is non-linear wave breaking. To calculate the gravity wave non-linearity in the WKB limit, we first calculate the radial Lagrangian displacement ξ_r. Assuming a constant wave energy escape rate, then the rate at which energy enters the cavity $L_{\mathrm{heat},\ell}$ equals the rate $\dot{E}_{\mathrm{leak}}$ at which the energy E in the

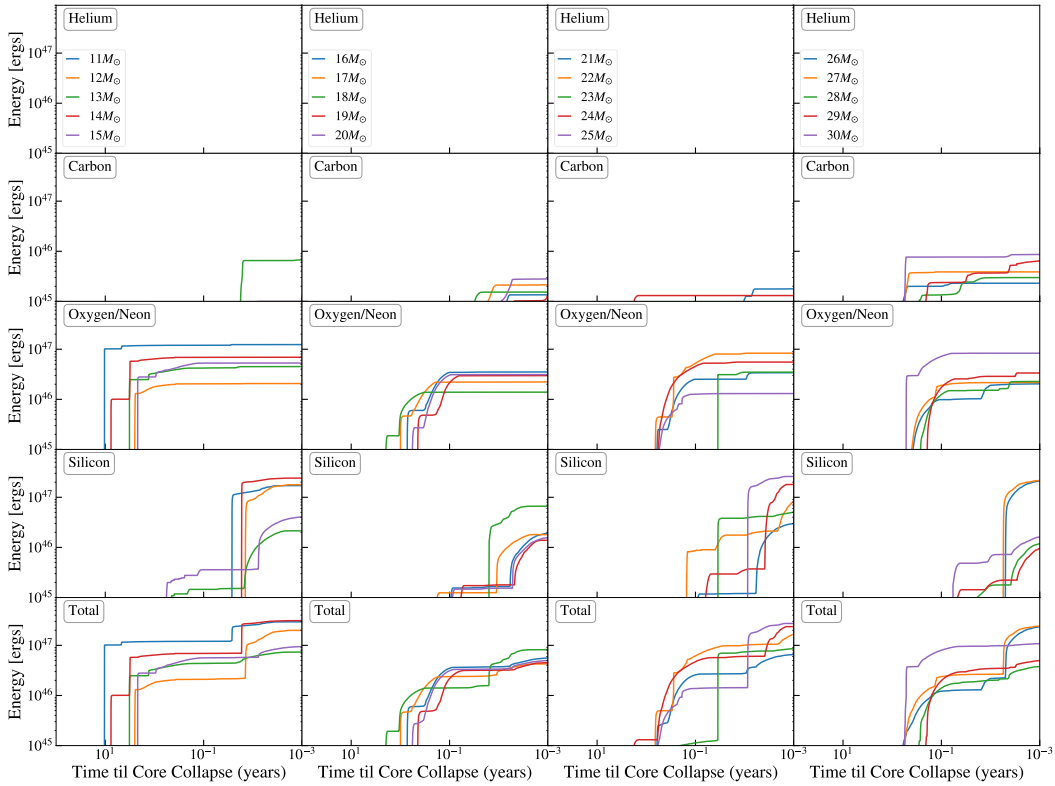

Figure 3.4: Accumulated wave heating energy transported to the envelope, for models corresponding to the heating rates of Figure 3.3.

g-mode cavity leaks out:

$$\dot{E}_{\rm leak} = \frac{E}{t_{\rm leak}}. \tag{3.16}$$

As in Fuller et al. (2015), the energy leakage timescale is

$$t_{\rm leak} = \frac{2t_{\rm cross}}{T^2}, \tag{3.17}$$

and the energy per unit radius

$$E_r = \frac{E}{v_g t_{\rm cross}} \tag{3.18}$$

is given by $E_r = 4\pi r^2 \rho \omega^2 \xi^2$ in the cavity, where ξ is the wave displacement amplitude. Using the fact that the radial displacement $|\xi_r| \simeq \frac{\omega}{N}|\xi|$ for gravity waves, we can rearrange to find

$$|\xi_r|^2 = \frac{2}{T_{\rm min}^2} \frac{L_{{\rm heat},\ell}}{4\pi r^2 \rho v_g N^2}. \tag{3.19}$$

Then a measure of the gravity wave non-linearity as a function of ℓ is

$$|k_r \xi_r| = \left[\frac{2}{T_{\rm min}^2} \frac{L_{{\rm heat},\ell} N [\ell(\ell+1)]^{3/2}}{4\pi \rho r^5 \omega^4} \right]^{1/2} \tag{3.20}$$

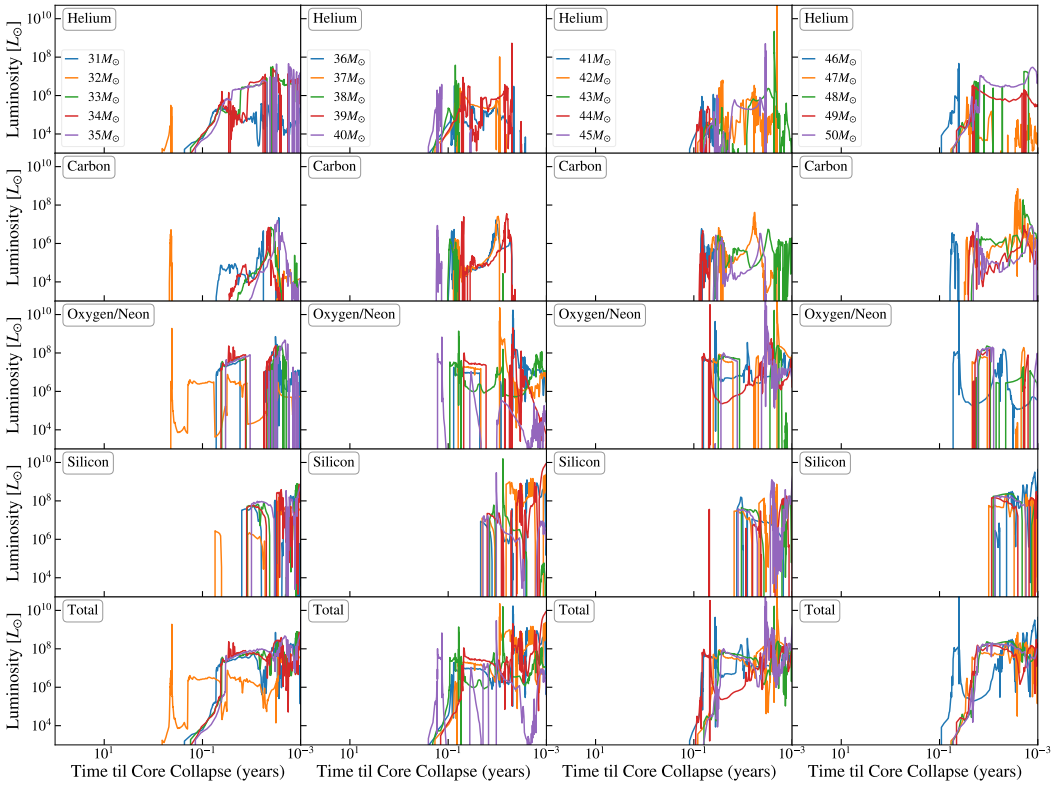

Figure 3.5: Same as Figure 3.3, but showing the wave heating luminosity for models with initial mass in the range 31–50 $M_\odot$.

Where $|k_r \xi_r| \geq 1$, waves are highly non-linear, whereas linear waves have $|k_r \xi_r| \leq 1$. Highly non-linear gravity waves will break and their energy will cascade to small scales, where the energy dissipates and thermalizes on a wave crossing time scale (Barker and Ogilvie, 2010). This process caps wave amplitudes at $|k_r \xi_r| \sim 1$. Waves that require large amplitudes ξ_r to sustain their power and frequency are potentially non-linear. Since non-linear terms couple waves of different ℓ, it is not clear what the appropriate non-linear breaking threshold is for a spectrum of waves, but if a wave of any ℓ value has $|k_r \xi_r| \geq 1$, it is likely that a non-linear cascade will damp the energy of all the waves on a short time scale. We account for this non-linear damping by capping the wave amplitude as described below.

Methods

We run a suite of MESA simulations (Paxton et al., 2011; Paxton et al., 2013; Paxton et al., 2015; Paxton et al., 2018; Paxton et al., 2019) for zero-age main sequence (ZAMS) masses between 11 and 50 $M_\odot$ and evolve the stars from the main sequence

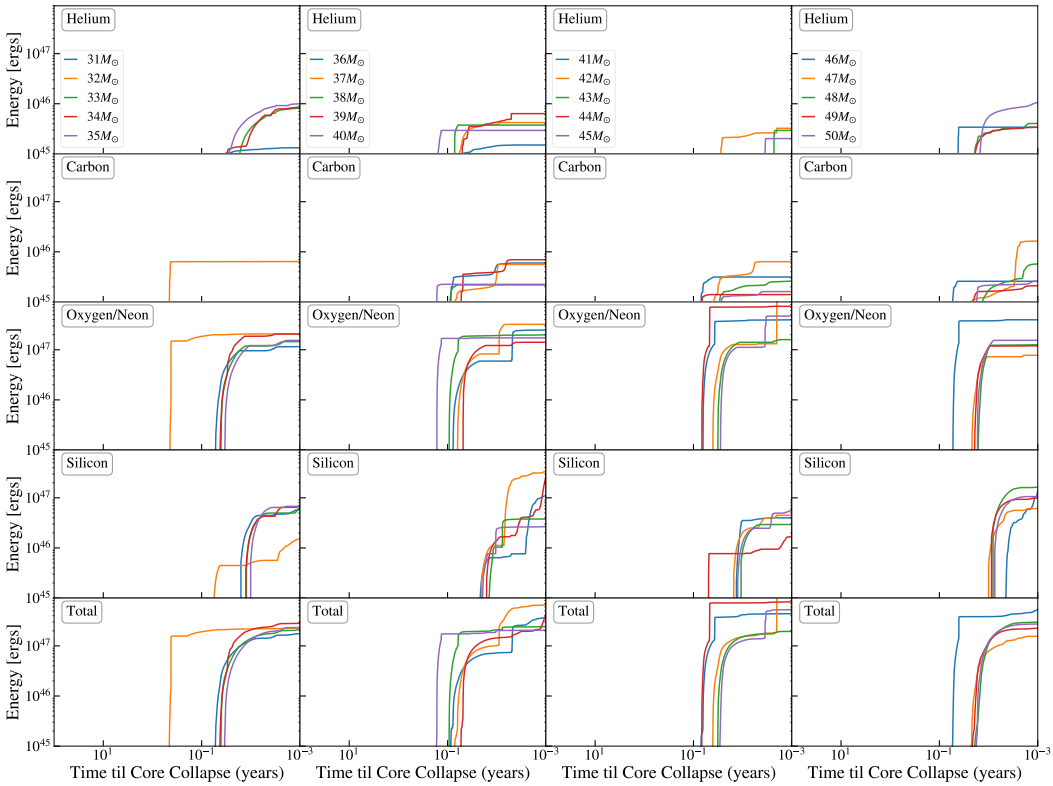

Figure 3.6: Same as Figure 3.4, but for the accumulated energy of higher mass models in the range 31–50 $M_\odot$.

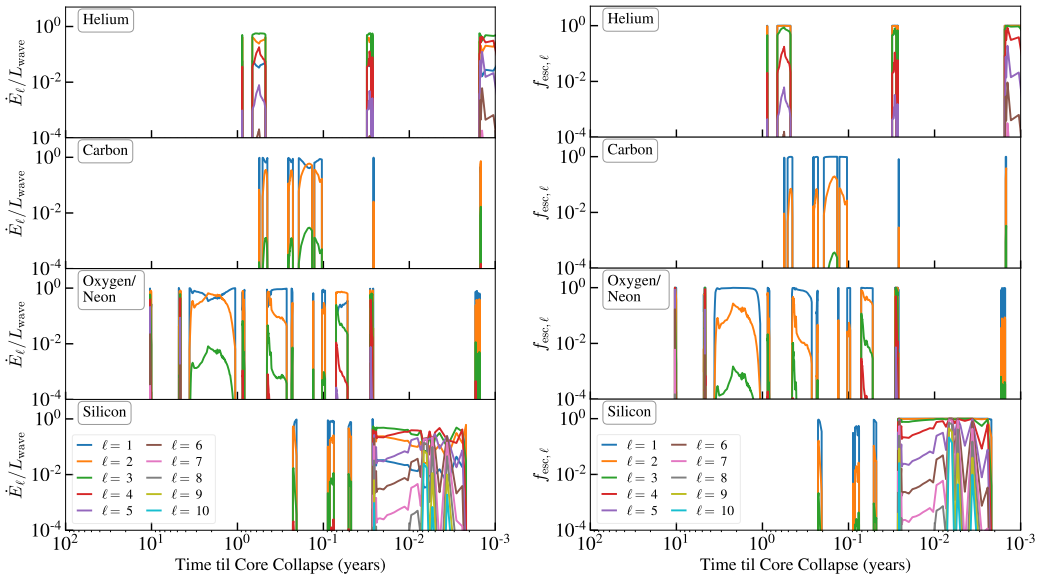

Figure 3.7: Fraction of total wave heat deposited in the envelope by waves of each angular number ℓ (left), and the wave escape probability for each ℓ (right), for the 11 $M_\odot$ model shown in Figures 3.3 and 3.4. Results are only shown for waves where $L_{{\rm heat},\ell} > 10^3\ L_\odot$.

to core collapse.[1] The evolution of late burning stages in the core is primarily determined by the helium (He) core mass and the carbon (C) core mass, each shown in Figure 3.2 as a function of initial (ZAMS) mass. Here, the He core mass is the mass coordinate where the He mass fraction is ≥ 0.01 and the hydrogen mass fraction has dropped below 0.01; similarly, the C core mass defines the transition where the He mass fraction < 0.01 and C mass fraction ≥ 0.01.

At each timestep, we perform the following calculations for the convective burning regions in each model.

1. Calculate wave luminosity and frequency: We find the mass-weighted average of the total wave luminosity and convective frequency within each convective burning region (Equations 3.1 and 3.3). We assume here that the waves of each ℓ value are of the same frequency $\omega = \omega_{\rm con}$, and we consider $\ell = 1$ to 10 waves.

2. Calculate transmission coefficient and neutrino damping factor for each ℓ value: For each ℓ value, we integrate over the evanescent regions above each convective burning region, using Equation 3.9 to find the transmission coefficient T^2 through each evanescent region. As explained in Section 3.3, we use the minimum $T^2_{\rm min}$ when there are multiple evanescent regions. For the wave energy attenuated due to local neutrino damping and radiative diffusion damping, the damping rates due to these effects are given by Equations 3.10 and 3.11. We integrate Equation 3.13 through all overlying gravity wave cavities and calculate the attenuation factor f_ν for each ℓ value.

3. Calculate wave heating rate and energy transmitted: Given the transmission coefficient T^2 and the neutrino damping factor f_ν, the fraction of wave luminosity that can escape is given by Equation 3.14 for each ℓ value. The total heating luminosity $L_{\rm heat}$ for each convective burning region is calculated by summing up the wave energy generation rate per ℓ value multiplied by the escape fraction per ℓ value, i.e., $L_{\rm heat} = \sum_{\ell=1}^{10} f_{{\rm esc},\ell} \dot{E}_\ell$. Then the energy transmitted to the envelope at each time step is

$$\Delta E_{\rm heat} = L_{\rm heat} dt, \tag{3.21}$$

evaluated for each convective burning region that generates waves.

[1] Model parameters are available on Zenodo at 10.5281/zenodo.4416166.

4. Calculate wave non-linearity: Section 3.3 introduces $|k_r \xi_r|$ as a measure of the nonlinearity of the gravity waves and notes that waves of different ℓ are coupled by nonlinear effects. As a result, we consider the largest value of $|k_r \xi_r|$ out of all the waves of different ℓ. If this maximum $|k_r \xi_r| > 1$ in the gravity wave cavity, the wave amplitudes are likely capped such that $|k_r \xi_r| \lesssim 1$. The wave power is proportional to the square of the wave amplitude, so in the case of non-linear waves we reduce $L_{\rm heat}$ by a factor of $|k_r \xi_r|^2$. While we are not able to capture the complexities of how non-linear coupling among waves of different ℓ truly affects wave heating, this approach at least provides us with an understanding of where non-linear effects are most important.

3.4 Results

Figure 3.3 shows the wave heating rate $L_{\rm heat}$ (Equation 3.21) of models in the mass range 11–30 $M_\odot$, and Figure 3.4 shows the cumulative energy transmitted by waves to the envelope, $\int L_{\rm heat} dt$, for this mass range. Each row corresponds to the wave heat generated by different convective burning regions, He, C, O/Ne, and Si, throughout the stars' lifetimes. In our models, the largest power is usually produced by O/Ne and Si burning regions, whereas the typical power from He and C burning is 1–2 orders of magnitude lower.

The mass range 11–20 $M_\odot$ typically generates $10^{5-6}\, L_\odot$ of wave power from O/Ne burning between 0.01–10 years before core collapse, with brief excursions above $10^{6-7}\, L_\odot$ that typically occur at the ignition of core or shell burning phases. In more massive stars, between 21–30 $M_\odot$, waves from O/Ne burning typically carry $10^{6-7}\, L_\odot$ from ~ 0.1 years before core collapse onward. The spikes in wave energy generation rates from O/Ne burning months to years before core collapse are responsible for the majority of wave heating in the 11–15 $M_\odot$ models, creating the sudden jumps in accumulated energy in Figure 3.4. These sudden jumps are most pronounced in the lowest mass models because O/Ne burning ignites in semi-degenerate conditions, discussed more in Section 3.4. For some models, certain C shell burning spikes in wave power can be of similar magnitude, but they occur too briefly and too late in the star's lifetime to contribute appreciably to wave heating. Waves from Si burning can carry 1–2 orders of magnitude more power than O/Ne burning throughout the 11–30 $M_\odot$ models, but Si burning only sustains this power for days to weeks before core collapse.

For the high-mass models between 31–50 $M_\odot$, Figure 3.5 shows that wave power is

generally higher for all burning types, but the high luminosity phases are both brief and late in the star's lifetime. The power from He and C burning waves remains 1–2 orders of magnitude lower than that of the other burning regions. The waves produced by O/Ne burning in these high-mass models generate $\sim 10^{7-8}\ L_\odot$ of power from a few weeks before core collapse onward. Meanwhile, the power carried by Si burning waves is on the same order as that of O/Ne burning waves, but this power is only sustained for hours to days before core collapse. Throughout the mass range 20–50 $M_\odot$, many models exhibit extremely large spikes in the wave heating rates of O/Ne burning that reach $\sim 10^{10}\ L_\odot$. One notable example is the spike of the 32 $M_\odot$ model months before core collapse, which is atypically early for its mass range. These spikes are due to convective shell mergers, discussed further in Section 3.4.

The models in the lower mass range 11–30 $M_\odot$ exhibit quite a bit of scatter in the accumulated energy transmitted by waves (Figure 3.4), as changing the mass by only 1 $M_\odot$ alters both the total amount of energy accumulated and the time before core collapse when the most energy is transmitted. This is particularly evident when looking at the energy transmission from Si burning, which may accumulate $> 10^{47}$ erg by 10^{-2} years before core collapse in some models, but fails to achieve this in models that only differ by a solar mass. In the upper mass range, Figure 3.6 shows that models which are close in mass typically result in similar magnitudes and timescales of energy deposition. However, there is still a fair amount of scatter in the energy scale of Si burning, and there are a few outliers. Compared to the other models in the 31–35 $M_\odot$ mass range, the 32 $M_\odot$ model accumulates $> 10^{47}$ erg of energy earlier in O/Ne burning. Similarly, the 44 $M_\odot$ and 46 $M_\odot$ models have higher and earlier O/Ne heating than neighboring-mass models.

Despite the large scatter, there are general trends within different mass ranges in our models. For the majority of 11–20 $M_\odot$ models, O/Ne burning dominates the transmitted energy and the energy transmission rises early, at a few months to years before core collapse. The 21–30 $M_\odot$ models reach similar energy scales to the 11–20 $M_\odot$ models, but usually this accumulates later at weeks before core collapse. In all models from 11–30 $M_\odot$, there is negligible energy transmission from He burning and very little contribution from C burning as well.

In the 31–50 $M_\odot$ range, most models begin to accumulate more energy than the lower-mass models in O/Ne burning. In addition, this energy is transmitted later on average, at several days to weeks before core collapse. He and C burning each still contribute over an order of magnitude less energy in this mass range. Throughout

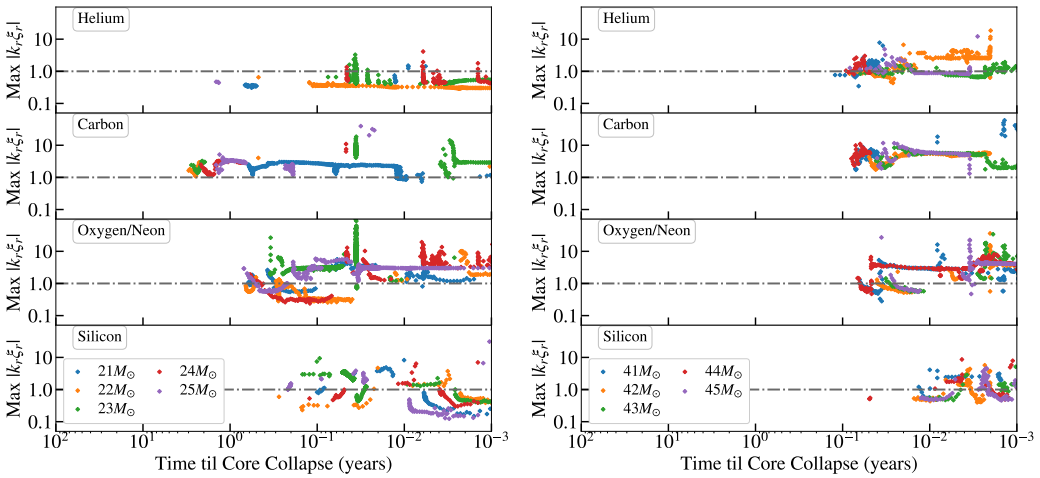

Figure 3.8: The maximum value of $|k_r\xi_r|$, taken over waves of all ℓ, for models with initial mass 21–25 $M_\odot$ (left) and 41–45 $M_\odot$ (right). The gray dashed-dotted line denotes $|k_r\xi_r| = 1$, above which the waves are considered strongly nonlinear so that the wave heating rate is reduced, as described in the text. Results are only shown for waves where $L_{\mathrm{heat},\ell} > 10^3\ L_\odot$.

these high-mass models, Si burning consistently accumulates energy in a sharp, late rise at $\sim$ 1–3 days before core collapse. However, the $\sim 10^{47}$ erg of energy accumulated from Si burning is typically a few times less than that deposited by waves from O/Ne burning.

In most of these models, the heating is dominated by $\ell = 1$–3 waves, as exemplified for the 11 $M_\odot$ model in Figure 3.7 (note that the escape and heating fractions are only shown for waves where $L_{\mathrm{heat},\ell} > 10^3\ L_\odot$). The right panel shows that low-ℓ waves are much more likely to escape before damping, due to their larger transmission coefficients T^2 (Equation 3.9) and their smaller damping fractions (Equation 3.13). Although the wave power spectrum generated by convection usually peaks for $\ell \gtrsim 3$ (Figure 3.1) so that more power initially goes into higher ℓ waves, the escape fraction is many orders of magnitude smaller for high ℓ. Consequently, waves of $\ell = 1$ and $\ell = 2$ (and occasionally $\ell = 3$) constitute the large majority of the escaping heat, as shown in the left panel of Figure 3.7. Only for helium burning are $\ell = 4, 5$ able to contribute comparable amounts.

Our wave heating rates are about an order of magnitude lower than predicted by previous work. Fuller (2017) estimated for a 15 $M_\odot$ red supergiant that waves generated from core O/Ne burning would carry $\sim 10^7\ L_\odot$ of power and that $\sim 10^{48}$ erg of energy would be deposited into the envelope at months to years before core

collapse; in our results, that mass range at best would transmit 10^{47} erg on that timescale from O/Ne burning and possibly a few times 10^{47} erg much later from Si burning. In addition, Shiode and Quataert (2014) found that core O/Ne burning for 12–30 $M_\odot$ models excites waves carrying a few $\times 10^{46–47}$ and few $\times 10^{47}$ erg of energy, and high mass models (40 $M_\odot$ and 50 $M_\odot$) carry up to 8×10^{47} erg of wave energy from O/Ne burning. In contrast, we estimate transmitted wave energies that are lower by a factor of a few on average compared to the models in Shiode and Quataert (2014).

The differences stem from the fact that prior work assumed that most wave power went into $\ell = 1$ waves, and previous calculations did not account for non-linear wave dissipation. In our implementation of wave physics, we distribute wave power over a spectrum of different ℓ-valued waves. Figure 3.1 shows that for typical values of $\ell_{\rm con} \gtrsim 2$, $\ell = 1$ waves receive $\lesssim 10\%$ of the wave flux. This large reduction accounts for most of the differences with prior work, though non-linear wave breaking also plays a role.

Non-linearity

When waves are strongly non-linear such that $|k_r \xi_r| > 1$ within the core, we reduce the wave heating rate by a factor of $|k_r \xi_r|^2$ (Section 3.3). As shown in Figure 3.8, this reduction can amount to a suppression of 1–2 orders of magnitude in some cases. The points in Figure 3.8 (only plotted for waves where $L_{{\rm heat},\ell} > 10^3\, L_\odot$ as in Figure 3.7) show the maximum value of $|k_r \xi_r|$ out of waves of all ℓ for two mass ranges, 21–25 $M_\odot$ (left) and 41–45 $M_\odot$ (right). In these mass ranges, as well as for all models with $M > 15\, M_\odot$, the waves are usually nonlinear during carbon, oxygen/neon, and silicon burning. In the upper mass range of 35–50 $M_\odot$, waves produced by helium burning are also nonlinear throughout the last 0.1–10 years until core-collapse.

Reducing the wave power by non-linearity has the most considerable effect on waves generated by convective C shell burning, since in this case often the waves carrying the most power are also quite non-linear. Before taking non-linearity into account, there were several models in every mass range which could transmit close to 10^{47} erg of energy via C shell burning waves, but non-linear saturation limits the accumulated energy of C burning waves in any model to at most 10^{46} erg. The typical value of $|k_r \xi_r|$ for O/Ne and Si burning waves is similar overall to that of C burning waves, but unlike C burning waves, the O/Ne and Si burning waves that

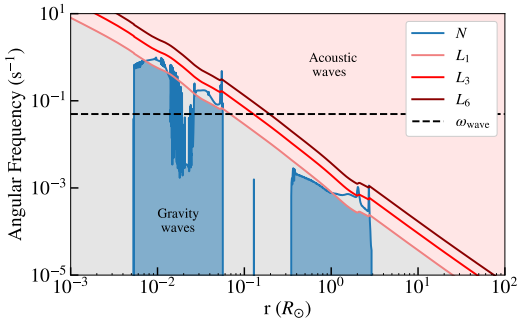

Figure 3.9: Propagation diagram for the 11 $M_\odot$ model during core Ne burning, showing the Brunt-Väisälä frequency N (blue) and the Lamb frequency L_ℓ for $\ell = 1, 3$, and 6 (shades of red). Waves propagate through the gravity wave cavity (blue region) and into the envelope as acoustic waves (red region, shown for $\ell = 1$), tunneling through evanescent zones (gray region) along the way. Semi-degenerate Ne ignition in the core causes vigorous convection, exciting waves with high frequencies of $\omega \sim 0.05$ rad/s (dashed line). The high frequencies of these waves allow them to more easily tunnel through a thinner evanescent zone.

carry the largest $L_{\text{heat},\ell}$ are often less non-linear. Thus in most of the models they are still able to transmit considerable amounts of energy and they usually make the largest contributions to energy transmission in the models. Due to these very energetic waves, the energy transmission from O/Ne and Si burning each remain the same order of magnitude after suppression due to non-linearity in most of the models. Exceptions to this include the 25 $M_\odot$ and 27 $M_\odot$ models, which experience significant suppression of O/Ne burning due to non-linear effects. In particular, the O/Ne and Si energy transmission for the 11–20 $M_\odot$ mass range is not significantly altered by non-linear effects, due to the high wave frequencies in these models.

Notable models

One of the main new results of our investigation is that the lowest mass models show some of the largest heating rates from O/Ne burning. For example, the 11 $M_\odot$ model is noteworthy because its O/Ne heating rate is very large and occurs ≈ 10 years before core collapse, earlier than most models. Figure 3.9 shows a propagation diagram for this model, which demonstrates that the frequency of the waves associated with the large O/Ne burning luminosity is high enough to create a thin evanescent region above the core so that waves can easily tunnel into the envelope. As a result, the high wave luminosity is not as greatly reduced by neutrino damping. In addition, the high wave frequency reduces the impact of non-linearity (Equation 3.20).

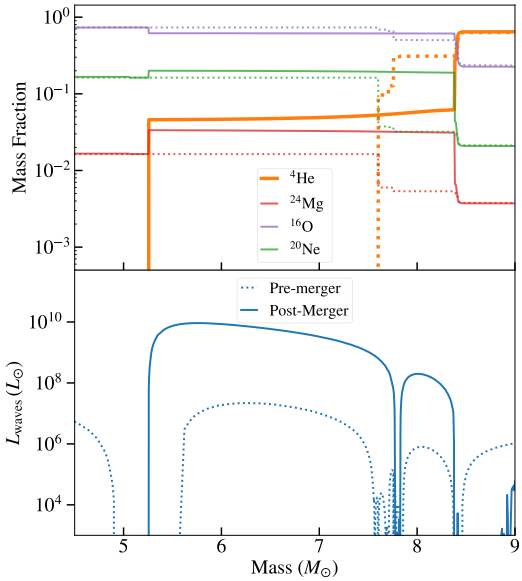

Figure 3.10: **Top**: The mass fractions of certain elements near the convective He and C burning shells immediately before a shell merger event (dotted lines), and after the shell merger (solid lines). All quantities are shown for a 30 $M_\odot$ model about 2 weeks before core collapse. Note how He is mixed downward into the C burning shell. **Bottom**: The wave luminosity (Equation 3.1) produced by the same convective shell before the shell merger (dotted) and after the shell merger (solid lines). The shell exhibits vigorous burning from α-capture reactions post-merger.

The high wave luminosities and frequencies of the 11 $M_\odot$ model are due to semi-degenerate ignition of Ne in the core; the degeneracy parameter $\eta \sim 10$ in the core at Ne ignition. In contrast, for models with $M > 15\,M_\odot$, $\eta \lesssim 1$ or at most $\eta \sim$ a few during core O/Ne burning, so these higher mass models do not exhibit vigorous burning due to semi-degenerate O/Ne ignition. Instances of degenerate Si ignition also lead to very large spikes in wave heating from Si burning for the 11, 12, and 14 $M_\odot$ models (Figure 3.3), and Si ignition in the 20–25 $M_\odot$ range is also moderately degenerate. However, these energy contributions occur quite late at ~ 0.01 years before core collapse.

In many of our high-mass models, convective shell mergers occur during the last year before core collapse. Typically this phenomenon occurs between a He and C burning shell, when He is mixed into the high-temperature C burning region. This then causes an enormous increase in energy generation due to chains of α-capture reactions on C, O, Ne, etc. The heating rates can be anomalously high, e.g., $L_{\rm waves} \gtrsim 10^{9\text{–}10}\,L_\odot$, suddenly increasing the energy transmission for the associated model.

For example, the jump in C and O/Ne burning for the 30 $M_\odot$ model stems from a shell merger (far right column of Figure 3.4). The top panel of Figure 3.10 shows how the shell merger affects the composition of the burning shell. The shell between 5–8 $M_\odot$ initially contains a negligible amount of helium (dotted yellow line in top panel of Figure 3.10), but the shell merger causes an influx of helium (solid yellow line) and triggers vigorous burning of C, O, Ne, etc., by α capture reactions. Due to the high temperature, these α captures are favored over the typical progression onward from triple-α burning of He. This causes the wave luminosity (Equation 3.1) generated by the burning shell to jump by three orders of magnitude (bottom panel of Figure 3.10). The sudden change in composition and luminosity is representative of the shell merger phenomenon that is seen in many of the higher-mass models.

These shell mergers are consequential for our models, as the jumps in wave power transmit large amounts of energy that often constitute major contributions to the accumulated energy of the model. In the 21–30 $M_\odot$ mass range, sudden jumps in O/Ne heating are generally due to shell mergers, with the exception that the jump in energy for 23 $M_\odot$ in O/Ne is due to central core ignition after a period of off-center O burning. The 31–46 $M_\odot$ mass range exhibits shell mergers in all but the 31 $M_\odot$, 33–35 $M_\odot$, and 43 $M_\odot$ models, and the shell mergers are linked to large spikes in energy in those models. For $M \geq 47\,M_\odot$, shell mergers occur, but later than 10^{-3} years before core collapse. In contrast, no models between 11–20 $M_\odot$ have shell mergers.

Some of the most extreme jumps in energy caused by shell mergers are ultimately lowered by nonlinear effects so that the accumulated energy transmission becomes more typical of the associated model's mass range. While the vigorous convection excites high-frequency waves that are less prone to nonlinear damping, the enormous wave fluxes do lead to non-linearity. For example, although the energy transmission from the shell merger in the 30 $M_\odot$ model would be unusually large, non-linearity effects limit it to around the typical amounts in this mass range (Figure 3.4). In addition, the 32 $M_\odot$ and 35–40 $M_\odot$ models would have featured jumps in accumulated energy that were anomalously high without non-linearity reducing them to more typical amounts.

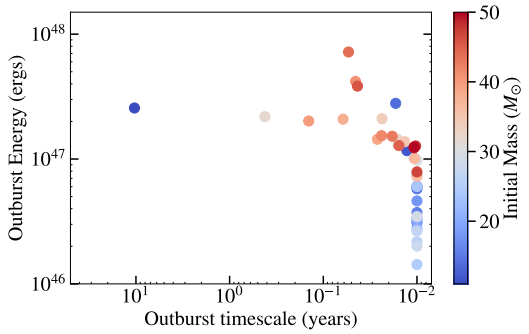

Figure 3.11: Outburst energy versus outburst timescale for each of our models, as defined in Section 3.5. The initial mass of each model is indicated by the color of the scatter point. We set the outburst timescale to a minimum value of 10^{-2} years for models that do not exceed 10^{47} erg by 10^{-2} years before core collapse.

3.5 Discussion

Outburst energies and time scales

To assess which models have the greatest potential to produce pre-supernova outbursts from wave heating, we consider the following two quantities: the outburst energy $E_{\rm burst}$, which we define as the total energy deposited by 10^{-2} years before core collapse; and the outburst timescale $t_{\rm burst}$, which we define as the time until core collapse for accumulated wave energy to exceed 10^{47} erg. We choose the value 10^{47} erg because this is comparable to the amount of energy needed to eject substantial mass from a red supergiant or compact helium star (Fuller 2017; Fuller and Ro 2018, Linial et al. in prep), and is thus an approximate threshold energy needed to power a pre-SN outburst.

Figure 3.11 shows where each of our models lies on a plot of outburst energy versus outburst timescale. We set a minimum outburst timescale of 10^{-2} years, so models which do not accumulate 10^{47} erg of energy by 10^{-2} years before core collapse are plotted with their integrated wave heat at a time of 10^{-2} years. Thus the figure shows a group of models at $t_{\rm burst} = 10^{-2}$ years which have accumulated $E_{\rm burst} < 10^{47}$ erg of energy by this time.

The majority of models which do reach $E_{\rm burst} > 10^{47}$ erg by 10^{-2} years before core collapse are clustered just above the threshold energy and time. Thus we expect most stars with “outbursts" will lie at the weak end of the distribution, and their outbursts may only become apparent in the final days before explosion. It is important to remember that because of the time it takes acoustic waves to propagate to the surface, there is a substantial delay between the wave generation

and the deposition of energy in the envelope. This delay time will be approximately $t_{\rm delay} \sim 0.02\,{\rm year}(M/10\,M_\odot)^{-1/2}(R/100R_\odot)^{3/2}$. In red/yellow supergiants with hydrogen-rich envelopes, there is not enough time for the acoustic waves to propagate to the surface, so these stars would likely exhibit no outburst at all.

However, several models may produce earlier and more energetic outbursts. The 11 $M_\odot$ model is a clear outlier; with $t_{\rm burst} = 10$ years, its outburst timescale is orders of magnitude earlier than most models. Its energy scale is also above average, with $E_{\rm burst} = 2.5 \times 10^{47}$ erg, due to the semi-degenerate ignition of Ne as discussed in Section 3.4. The next earliest model, with initial mass 32 $M_\odot$, has a similar energy scale but an outburst timescale of months. The 44 $M_\odot$ model has the highest outburst energy, $E_{\rm burst} = 7.2 \times 10^{47}$ erg. Within the group of energetic and early outliers, all but two of the models are very massive ($M > 30\,M_\odot$) and experienced a shell merger event that catapulted the accumulated energy of that model up to $> 10^{47}$ erg. The exceptions are the 11 $M_\odot$ and 14 $M_\odot$ models (blue dots at $E_{\rm burst} \approx 2$–3×10^{47} erg), both of which experience degenerate ignition of O/Ne or Si burning as explained above

Once the wave energy is transmitted to the base of the stellar envelope, the waves will damp as they travel toward the surface as acoustic waves and deposit their energy in the envelope. Waves steepen and thermalize their energy due to both weak shock dissipation and radiative diffusion damping. This process is described in detail for red supergiants in Fuller (2017) and hydrogen-poor progenitors in Fuller and Ro (2018). They find that wave energy is typically deposited just above the core, where the wave heat can increase the pressure of the heated region and cause it to expand. The expansion is approximately hydrostatic if $t_{\rm heat} \gtrsim t_{\rm dyn}$, but if $t_{\rm heat} < t_{\rm dyn}$, it will launch a pressure wave. For red supergiants, Fuller (2017) find that during core Ne burning, $t_{\rm heat} < t_{\rm dyn}$ so that wave heating launches a pressure wave into the envelope, which drives a small outflow ($M < M_\odot$). In addition, wave heating from core O burning, where $t_{\rm heat} \gtrsim t_{\rm dyn}$, inflates the envelope and causes an unusual envelope density structure to form. In stripped progenitors, waves deposited just above the core are very near the stellar surface, so the wave energy deposition also drives an outflow (Fuller and Ro, 2018).

Implications for supernovae and their progenitors

As described in Section 3.4, our results for the energy transmitted by wave heating are generally lower than that of prior work since we now account for a spectrum of

ℓ = 1–10 waves and for non-linear wave dissipation. We therefore find outbursts to be less common among our models than previously expected; in turn, those models that do have outbursts also have lower outburst energies than the findings of prior work. Our models do not yet include the effects of wave heating on the star's structure and luminosity, but our results allow for basic inference of pre-SN outburst properties.

The outburst energies and timescales of our models indicate that outbursts may be most common among low-mass ($M \lesssim 12\,M_\odot$) stars and a fraction of high-mass ($M \gtrsim 30\,M_\odot$) stars. Many of these progenitors would exhibit outbursts on a timescale of days to weeks before core collapse, but the outburst timescale varies considerably. As noted in Section 3.5, the delay time for acoustic waves to propagate to the surface and produce a potential outburst could be longer than the time to core-collapse in red supergiants. We may also consider outbursts from stripped SN progenitors, which will have similar outburst timescales and energies to models that share the same He/C core masses since the evolution of core burning in stars is well determined by these quantities (Figure 3.2). Given the negligible delay-time in stripped SN progenitors, outbursts can occur in these stars even for timescales far closer to core collapse.

For low-mass stars, pre-SN outbursts are most likely to occur years or perhaps even decades before core-collapse for the lowest-mass SN progenitors. Such outbursts would be fueled by high wave energies generated by vigorous convection at the onset of semi-degenerate Ne ignition. We have not simulated $M < 11\,M_\odot$ stars, whose core evolution can be very complex and difficult to model due to off-center ignition of O/Ne and Si; yet since these elements ignite semi-degenerately, wave-driven outbursts may be common in these stars. Indeed, even in the absence of convectively excited gravity waves, degenerate Si ignition in these stars can launch an energetic hydrodynamic pulse that can partially eject the envelope (Woosley and Heger, 2015) weeks or months before core collapse. Convectively excited waves may increase the energy of such outbursts, as well as the parameter space over which they occur.

In general, we expect that more energetic wave heating is capable of producing more massive ejecta, and earlier outburst timescales will propel the CSM to larger radii where it can affect the supernova light curve and spectrum. For example, the outburst energy of our 11 $M_\odot$ model is sufficient to eject a thin ($\sim 1\,M_\odot$) hydrogen envelope from a yellow supergiant and accelerate it to ~ 100 km/s. In the ten years between

that event and core-collapse, this material could expand out to $\sim 3 \times 10^{15}$ cm. This CSM mass, radius, and velocity is similar to that inferred for transformational SNe such as SN2017dio (Kuncarayakti et al., 2018). It is also similar that inferred for SN2014C (Margutti et al., 2017), though the inferred CSM radius in that event of $> 10^{16}$ cm is larger by an order of magnitude. A wave-driven outburst from a slightly lower mass progenitor, with longer time until core-collapse, could potentially explain that event.

In a hydrogen-rich envelope, the larger binding energy may prevent total envelope disruption, but the envelope's density profile may be altered and a small amount of marginally bound CSM may also be produced (Fuller, 2017). This type of very confined CSM potentially contributes to early peaks in some type II-P SNe light curves (Moriya et al., 2011; Morozova, Piro, and Valenti, 2017; Das and Ray, 2017; Moriya et al., 2018; Morozova et al., 2020). The CSM structure depends on the details of the heating history, as slow and steady heating will inflate the star without producing CSM and will not match observations of type II-P SNe (Ouchi and Maeda, 2019). However, our models typically exhibit sharp spikes in the wave heating rate at the onset of nuclear burning phases. This sudden wave heating can likely launch shocks that propagate through the stellar envelope, potentially unbinding material at the surface rather than inflating the entire star (Morozova et al., 2020; Leung and Fuller, 2020). More detailed hydrodynamic modeling should be performed to determine the pre-SN stellar/CSM density profile resulting from these outbursts.

In hydrogen-free progenitors, the ejected mass would form a dense wind (Fuller and Ro, 2018) of circumstellar He, perhaps similar to that observed via flash ionization in the heavily stripped type Ib/c SNe iPTF 14gqr (De et al., 2019) and SN2019dge (Yao et al., 2020). However, SNe with even larger inferred CSM radii ($R_{\rm CSM} \gtrsim 10^{17}$ cm, such as SN2004dk (Mauerhan et al., 2018; Pooley et al., 2019), most likely arise from a different mechanism that can operate at longer timescales ($\gtrsim$ 100 years) before core-collapse.

More massive progenitors with shorter pre-SN outburst time scales are likely to produce a more confined CSM. For instance, the outburst energies of our $36-40\,M_\odot$ models are sufficient to eject $\sim 10^{-2}\,M_\odot$ from their He cores (assuming they end their lives as $M \sim 15\,M_\odot$ Wolf-Rayet stars), but this material can only expand out to $\sim 2\times10^{14}$ cm before core-collapse. It is thus swept up within the first few days after explosion. However, the shock breakout from this extended CSM would produce an extremely fast rise and fall of the optical light curve, and these CSM parameters are

very similar to that inferred for the Ic-BL SN2018gep (Ho et al., 2019). Hence, we believe confined wave-driven CSM from massive progenitors ($M_{\rm ZAMS} \gtrsim 30\,M_{\odot}$) may provide a compelling explanation for some fast blue optical transients (FBOTs) like SN2018gep.

Caveats

Our results for wave energy transport still involve several uncertainties in the treatment of the relevant physics. Although we are able to identify waves that should experience non-linear wave breaking and have included an approximation of this attenuation in our calculations, it is difficult to quantify how much the amplitude of each wave will be reduced. Due to non-linear coupling between waves of different ℓ, it is also not clear exactly when non-linear breaking will occur. A determination of a reliable metric for the onset and efficacy of non-linear damping by extending upon work such as Kumar and Goodman (1996) and Weinberg and Quataert (2008) should be performed in the future.

The uncertainty of the convectively excited wave spectrum must also be considered. Our work assumes the spectrum of Equation 3.4, but the true spectrum remains a subject of active research (e.g., Lecoanet and Quataert 2013; Couston et al. 2018; Edelmann et al. 2019). We also assume all waves are excited at the same mass-weighted average value of $\omega_{\rm con}$, very different from the realistic polychromatic spectrum of waves generated by convection. The effect on wave heating rates is unclear. In the case of higher frequency waves, we would have underestimated $f_{\rm esc}$ (Equation 3.14), and vice versa for low frequency waves. We also used the mass-weighted convective luminosity for each convective burning shell in our calculations, but the gradient in convective frequency and luminosity is often quite steep across these regions. Therefore, it is possible that waves are actually excited at different amplitudes and frequencies than we have assumed. Our models utilize standard MLT theory to model convection, but we note that convective instabilities (Arnett and Meakin, 2011; Meakin, Sukhbold, and Arnett, 2011; Smith and Arnett, 2014) may change the nature of convection (thereby changing the wave spectrum), potentially driving outbursts even in the absence of non-radial waves.

We have not modeled the effect that wave heating will have on the structure of the star, focusing here on calculating the amount of power and energy transported by waves. Once the waves reach the envelope, they will heat the envelope and modify its structure as discussed in Fuller (2017) and Fuller and Ro (2018), but this process

should not alter our calculations of the wave heating rate because the core evolution is nearly independent of the envelope. Furthermore, the wave energy dissipated within the core (i.e., the waves that do not escape) will not have a strong effect on its evolution, as the total energy from waves that enters the gravity wave cavity is much smaller than the binding energy of that cavity. For example, the wave energy $E_{\rm wave} = \int L_{\rm wave} dt$ excited throughout O/Ne and Si burning phases in the 11 $M_\odot$ model is negligible compared to the binding energy $E_{\rm bind}$ of the overlying g-mode cavity, $E_{\rm wave} \sim 10^{-3} E_{\rm bind}$; for our most energetic 44 $M_\odot$ model, O/Ne and Si burning phases only inject $E_{\rm wave} \sim 10^{-2} E_{\rm bind}$ into the overlying gravity wave cavity.

In addition, our 1D stellar evolution calculations cannot capture the multi-dimensional effects that come into play for convection during late nuclear burning stages. Yadav et al. (2020) demonstrate that 3D simulations of nuclear burning in the minutes before core-collapse can have much larger convective velocities than in 1D simulations. An increase in the assumed convective velocities could somewhat increase our wave-heating rates, which scale linearly with the RMS convective velocity for a given convective flux. Several other simulations of carbon and oxygen burning on longer time scales (e.g., Meakin and Arnett 2006; Meakin and Arnett 2007; Arnett, Meakin, and Young 2009; Arnett and Meakin 2011) also indicate that 1D models slightly underestimate RMS convective velocities, and they do not properly capture the stochasticity of convection and entrainment that occurs at convective boundaries. Hence, it seems likely that our models marginally underestimate wave flux, but it remains unclear whether other multi-dimensional effects will significantly alter our results.

Finally, we have treated the convective shell mergers in our simulations with some caution, as spontaneous mixing between convective shells can in some cases be a numerical artifact. We performed resolution tests on models that exhibited shell mergers to test whether they were products of poorly resolved shell boundaries. In our tests, the phenomena as described in Section 3.4 usually persisted throughout the increases in resolution, although in some cases details such as the timing of the shell merger changed. Thus the shell merger events were not occurring simply due to insufficient resolution in the cores of our models. Interestingly, 3D simulations of late-stage nuclear burning in general produce even more mixing and shell merger events than in 1D models (Yadav et al., 2020). Nevertheless, it remains uncertain whether adjusting different parameters of our models would have a significant effect on the prevalence of the shell mergers; if so, our results would be substantially

altered, as the high-mass models with the greatest outburst potential are each linked to a shell merger and its associated large spike in wave power.

3.6 Conclusion

We have modeled wave heating physics in single-star core-collapse SNe progenitors using a suite of MESA stellar evolution models with solar metallicity and ZAMS masses ranging between 11–50 $M_\odot$. As we evolve the stars until core-collapse, we calculate the wave power that is generated by core convection during late-stage nuclear burning, and the fraction of this energy that is transmitted to the stellar envelope. Our calculations improve on prior efforts by accounting for non-linear damping effects and implementing a more realistic wave spectrum. In most cases, $\ell > 2$ waves carry a large fraction of wave power but are more strongly trapped in the core than the $\ell = 1$ waves considered in prior work. Hence, much of the wave power is dissipated within the core via neutrino damping and non-linear wave breaking. These effects ultimately reduce our wave heating estimates by ~ 1 order of magnitude compared to previous results.

In our models for typical SN progenitors ($M_{\rm ZAMS} < 30\,M_\odot$), waves excited during oxygen/neon burning typically transmit $\sim 10^{46\text{–}47}$ erg of energy between $0.1 - 10$ years before core collapse. Though we have not simulated the response of the stellar envelope, comparison with Fuller (2017) and Fuller and Ro (2018) indicates this level of energy deposition is unlikely to drive a detectable pre-SN outburst in most SN progenitors.

There are important exceptions, however, especially in the lowest-mass and highest-mass SN progenitors. Many of our high-mass ($M_{\rm ZAMS} \geq 30\,M_\odot$) SN progenitors exhibit convective shell mergers that drive intense nuclear burning. Assuming these events are not numerical artifacts, waves in these models transmit more energy ($\sim 10^{47\text{–}48}$ erg) to the envelope, but not until $\sim 0.01 - 0.1$ years before core collapse. We speculate that the confined circumstellar medium created by these outbursts in hydrogen-free stars could lead to rapidly rising and fading transients resembling some fast blue optical transients.

In low-mass SN progenitors ($M_{\rm ZAMS} \lesssim 12 M_\odot$), semi-degenerate neon ignition greatly enhances wave heating due to higher wave fluxes and frequencies. This could drive pre-SN outbursts with energies $\sim 10^{47}$ erg, on a time scale of 10 years or longer before core-collapse, which could be related to the CSM found in transitional SNe and some type II-P SNe. Future investigations should further examine the

interplay of the complex core evolution and wave heating process in these low-mass stars. In subsequent work, we plan to model the hydrodynamic response of the stellar envelope to wave heating, making more informed predictions for the outburst luminosities, ejecta masses, and CSM density structures.

Acknowledgments

This work was partially supported by NASA grants HST-AR-15021.001-A and 80NSSC18K1017. JF acknowledges support from an Innovator Grant from The Rose Hills Foundation, and the Sloan Foundation through grant FG-2018-10515.

References

Arnett, D., C. Meakin, and P. A. Young (Jan. 2009). "Turbulent Convection in Stellar Interiors. II. The Velocity Field". In: *ApJ* 690.2, pp. 1715–1729. DOI: 10.1088/0004-637X/690/2/1715.

Arnett, W. D. and C. Meakin (June 2011). "Toward Realistic Progenitors of Core-collapse Supernovae". In: *ApJ* 733.2, p. 78. DOI: 10.1088/0004-637X/733/2/78.

Barker, A. J. and G. I. Ogilvie (June 2010). "On internal wave breaking and tidal dissipation near the centre of a solar-type star". In: *MNRAS* 404.4, pp. 1849–1868. DOI: 10.1111/j.1365-2966.2010.16400.x.

Benetti, S. et al. (May 2018). "ASASSN-15no: the Supernova that plays hide-and-seek". In: *MNRAS* 476.1, pp. 261–270. DOI: 10.1093/mnras/sty166.

Bilinski, C. et al. (Mar. 2018). "SN2012ab: a peculiar Type IIn supernova with aspherical circumstellar material". In: *MNRAS* 475.1, pp. 1104–1120. DOI: 10.1093/mnras/stx3214.

Chen, T. .-. et al. (Nov. 2018). "SN 2017ens: The Metamorphosis of a Luminous Broadlined Type Ic Supernova into an SN IIn". In: *ApJL* 867.2, p. L31. DOI: 10.3847/2041-8213/aaeb2e.

Clark, P. et al. (Feb. 2020). "LSQ13ddu: a rapidly evolving stripped-envelope supernova with early circumstellar interaction signatures". In: *MNRAS* 492.2, pp. 2208–2228. DOI: 10.1093/mnras/stz3598.

Couston, L.-A. et al. (Nov. 2018). "The energy flux spectrum of internal waves generated by turbulent convection". In: *Journal of Fluid Mechanics* 854, R3. DOI: 10.1017/jfm.2018.669.

Das, S. and A. Ray (Dec. 2017). "Modeling Type II-P/II-L Supernovae Interacting with Recent Episodic Mass Ejections from Their Presupernova Stars with MESA and SNEC". In: *ApJ* 851.2, p. 138. DOI: 10.3847/1538-4357/aa97e1.

De, K. et al. (Mar. 2019). "ZTF 18aaqeasu (SN2018byg): A Massive Helium-shell Double Detonation on a Sub-Chandrasekhar-mass White Dwarf". In: *ApJL* 873.2, p. L18. DOI: 10.3847/2041-8213/ab0aec.

Dessart, L., D. J. Hillier, and E. Audit (Sept. 2017). "Explosion of red-supergiant stars: Influence of the atmospheric structure on shock breakout and early-time supernova radiation". In: *A&A* 605, A83. DOI: 10.1051/0004-6361/201730942.

Edelmann, P. V. F. et al. (May 2019). "Three-dimensional Simulations of Massive Stars. I. Wave Generation and Propagation". In: *ApJ* 876.1, p. 4. DOI: 10.3847/1538-4357/ab12df.

Elias-Rosa, N. et al. (Apr. 2018). "SNhunt151: an explosive event inside a dense cocoon". In: *MNRAS* 475.2, pp. 2614–2631. DOI: 10.1093/mnras/sty009.

Elias-Rosa, N. et al. (June 2018). "The Type IIn Supernova SN 2010bt: The Explosion of a Star in Outburst". In: *ApJ* 860.1, p. 68. DOI: 10.3847/1538-4357/aac510.

Förster, F. et al. (Sept. 2018). "The delay of shock breakout due to circumstellar material evident in most type II supernovae". In: *Nature Astronomy* 2, p. 808. DOI: 10.1038/s41550-018-0563-4.

Fuller, J. (Sept. 2017). "Pre-supernova outbursts via wave heating in massive stars - I. Red supergiants". In: *MNRAS* 470.2, pp. 1642–1656. DOI: 10.1093/mnras/stx1314.

Fuller, J. and S. Ro (May 2018). "Pre-supernova outbursts via wave heating in massive stars - II. Hydrogen-poor stars". In: *MNRAS* 476.2, pp. 1853–1868. DOI: 10.1093/mnras/sty369.

Fuller, J. et al. (Oct. 2015). "Asteroseismology can reveal strong internal magnetic fields in red giant stars". In: *Science* 350.6259, pp. 423–426. DOI: 10.1126/science.aac6933.

Gangopadhyay, A. et al. (Feb. 2020). "Flash Ionization Signatures in the Type Ibn Supernova SN 2019uo". In: *ApJ* 889.2, p. 170. DOI: 10.3847/1538-4357/ab6328.

Goldreich, P. and P. Kumar (Nov. 1990). "Wave Generation by Turbulent Convection". In: *ApJ* 363, p. 694. DOI: 10.1086/169376.

Hillier, D. J. and L. Dessart (Nov. 2019). "Photometric and spectroscopic diversity of Type II supernovae". In: *A&A* 631, A8. DOI: 10.1051/0004-6361/201935100.

Ho, A. Y. Q. et al. (Dec. 2019). "Evidence for Late-stage Eruptive Mass Loss in the Progenitor to SN2018gep, a Broad-lined Ic Supernova: Pre-explosion Emission and a Rapidly Rising Luminous Transient". In: *ApJ* 887.2, p. 169. DOI: 10.3847/1538-4357/ab55ec.

Johnson, S. A., C. S. Kochanek, and S. M. Adams (Dec. 2017). "On the progenitor of the Type Ibc supernova 2012fh". In: *MNRAS* 472.3, pp. 3115–3119. DOI: 10.1093/mnras/stx2170.

Johnson, S. A., C. S. Kochanek, and S. M. Adams (Oct. 2018). "The quiescent progenitors of four Type II-P/L supernovae". In: *MNRAS* 480.2, pp. 1696–1704. DOI: 10.1093/mnras/sty1966.

Khazov, D. et al. (Feb. 2016). "Flash Spectroscopy: Emission Lines from the Ionized Circumstellar Material around <10-day-old Type II Supernovae". In: *ApJ* 818.1, p. 3. DOI: 10.3847/0004-637X/818/1/3.

Kochanek, C. S. et al. (May 2017). "Supernova progenitors, their variability and the Type IIP Supernova ASASSN-16fq in M66". In: *MNRAS* 467.3, pp. 3347–3360. DOI: 10.1093/mnras/stx291.

Kumar, P. and J. Goodman (Aug. 1996). "Nonlinear Damping of Oscillations in Tidal-Capture Binaries". In: *ApJ* 466, p. 946. DOI: 10.1086/177565.

Kuncarayakti, H. et al. (Feb. 2018). "SN 2017dio: A Type-Ic Supernova Exploding in a Hydrogen-rich Circumstellar Medium". In: *ApJL* 854.1, p. L14. DOI: 10.3847/2041-8213/aaaa1a.

Lecoanet, D. and E. Quataert (Apr. 2013). "Internal gravity wave excitation by turbulent convection". In: *MNRAS* 430.3, pp. 2363–2376. DOI: 10.1093/mnras/stt055.

Leung, S.-C. and J. Fuller (Sept. 2020). "Hydrodynamic Simulations of Pre-supernova Outbursts in Red Supergiants: Asphericity and Mass Loss". In: *ApJ* 900.2, p. 99. DOI: 10.3847/1538-4357/abac5d.

Lunnan, R. et al. (Sept. 2018). "A UV resonance line echo from a shell around a hydrogen-poor superluminous supernova". In: *Nature Astronomy* 2, pp. 887–895. DOI: 10.1038/s41550-018-0568-z.

Lunnan, R. et al. (Sept. 2020). "Four (Super)luminous Supernovae from the First Months of the ZTF Survey". In: *ApJ* 901.1, p. 61. DOI: 10.3847/1538-4357/abaeec.

Margutti, R. et al. (Feb. 2017). "Ejection of the Massive Hydrogen-rich Envelope Timed with the Collapse of the Stripped SN 2014C". In: *ApJ* 835.2, p. 140. DOI: 10.3847/1538-4357/835/2/140.

Mauerhan, J. C. et al. (Aug. 2018). "Stripped-envelope supernova SN 2004dk is now interacting with hydrogen-rich circumstellar material". In: *MNRAS* 478.4, pp. 5050–5055. DOI: 10.1093/mnras/sty1307.

Meakin, C. A. and D. Arnett (Jan. 2006). "Active Carbon and Oxygen Shell Burning Hydrodynamics". In: *ApJL* 637.1, pp. L53–L56. DOI: 10.1086/500544.

Meakin, C. A. and D. Arnett (Aug. 2007). "Anelastic and Compressible Simulations of Stellar Oxygen Burning". In: *ApJ* 665.1, pp. 690–697. DOI: 10.1086/519372.

Meakin, C. A., T. Sukhbold, and W. D. Arnett (Nov. 2011). “Presupernova structure of massive stars”. In: *Astrophysics and Space Science* 336.1, pp. 123–128. DOI: 10.1007/s10509-010-0591-8.

Moriya, T. et al. (July 2011). “Supernovae from red supergiants with extensive mass loss”. In: *MNRAS* 415.1, pp. 199–213. DOI: 10.1111/j.1365-2966.2011.18689.x.

Moriya, T. J. et al. (May 2018). “Type IIP supernova light curves affected by the acceleration of red supergiant winds”. In: *MNRAS* 476.2, pp. 2840–2851. DOI: 10.1093/mnras/sty475.

Morozova, V., A. L. Piro, and S. Valenti (Mar. 2017). “Unifying Type II Supernova Light Curves with Dense Circumstellar Material”. In: *ApJ* 838.1, p. 28. DOI: 10.3847/1538-4357/aa6251.

Morozova, V. et al. (Mar. 2020). “The Influence of Late-stage Nuclear Burning on Red Supergiant Supernova Light Curves”. In: *ApJL* 891.2, p. L32. DOI: 10.3847/2041-8213/ab77c8.

Nakaoka, T. et al. (June 2018). “The Low-luminosity Type IIP Supernova 2016bkv with Early-phase Circumstellar Interaction”. In: *ApJ* 859.2, p. 78. DOI: 10.3847/1538-4357/aabee7.

Ofek, E. O. et al. (July 2014). “Precursors Prior to Type IIn Supernova Explosions are Common: Precursor Rates, Properties, and Correlations”. In: *ApJ* 789.2, p. 104. DOI: 10.1088/0004-637X/789/2/104.

Ouchi, R. and K. Maeda (June 2019). “Constraining Massive Star Activities in the Final Years through Properties of Supernovae and Their Progenitors”. In: *ApJ* 877.2, p. 92. DOI: 10.3847/1538-4357/ab1a37.

Paxton, B. et al. (Jan. 2011). “Modules for Experiments in Stellar Astrophysics (MESA)”. In: *ApJS* 192, p. 3. DOI: 10.1088/0067-0049/192/1/3.

Paxton, B. et al. (Sept. 2013). “Modules for Experiments in Stellar Astrophysics (MESA): Planets, Oscillations, Rotation, and Massive Stars”. In: *ApJS* 208.1, p. 4. DOI: 10.1088/0067-0049/208/1/4.

Paxton, B. et al. (Sept. 2015). “Modules for Experiments in Stellar Astrophysics (MESA): Binaries, Pulsations, and Explosions”. In: *ApJS* 220.1, p. 15. DOI: 10.1088/0067-0049/220/1/15.

Paxton, B. et al. (Feb. 2018). “Modules for Experiments in Stellar Astrophysics (MESA): Convective Boundaries, Element Diffusion, and Massive Star Explosions”. In: *ApJS* 234.2, p. 34. DOI: 10.3847/1538-4365/aaa5a8.

Paxton, B. et al. (July 2019). “Modules for Experiments in Stellar Astrophysics (MESA): Pulsating Variable Stars, Rotation, Convective Boundaries, and Energy Conservation”. In: *ApJS* 243.1, p. 10. DOI: 10.3847/1538-4365/ab2241.

Pooley, D. et al. (Oct. 2019). "Interaction of SN Ib 2004dk with a Previously Expelled Envelope". In: *ApJ* 883.2, p. 120. DOI: 10.3847/1538-4357/ab3e36.

Quataert, E. and J. Shiode (June 2012). "Wave-driven mass loss in the last year of stellar evolution: setting the stage for the most luminous core-collapse supernovae". In: *MNRAS* 423.1, pp. L92–L96. DOI: 10.1111/j.1745-3933.2012.01264.x.

Shiode, J. H. and E. Quataert (Jan. 2014). "Setting the Stage for Circumstellar Interaction in Core-Collapse Supernovae. II. Wave-driven Mass Loss in Supernova Progenitors". In: *ApJ* 780.1, p. 96. DOI: 10.1088/0004-637X/780/1/96.

Shiode, J. H. et al. (Apr. 2013). "The observational signatures of convectively excited gravity modes in main-sequence stars". In: *MNRAS* 430.3, pp. 1736–1745. DOI: 10.1093/mnras/sts719.

Smith, N. and W. D. Arnett (Apr. 2014). "Preparing for an Explosion: Hydrodynamic Instabilities and Turbulence in Presupernovae". In: *ApJ* 785.2, p. 82. DOI: 10.1088/0004-637X/785/2/82.

Stritzinger, M. D. et al. (Feb. 2020). "The Carnegie Supernova Project II. Early observations and progenitor constraints of the Type Ib supernova LSQ13abf". In: *A&A* 634, A21. DOI: 10.1051/0004-6361/201936619.

Taddia, F. et al. (June 2020). "The Carnegie Supernova Project II. The shock wave revealed through the fog: The strongly interacting Type IIn SN 2013L". In: *A&A* 638, A92. DOI: 10.1051/0004-6361/201936654.

Weinberg, N. N. and E. Quataert (June 2008). "Non-linear saturation of g-modes in proto-neutron stars: quieting the acoustic engine". In: *MNRAS* 387.1, pp. L64–L68. DOI: 10.1111/j.1745-3933.2008.00486.x.

Woosley, S. E. and A. Heger (Sept. 2015). "The Remarkable Deaths of 9-11 Solar Mass Stars". In: *ApJ* 810.1, p. 34. DOI: 10.1088/0004-637X/810/1/34.

Yadav, N. et al. (Feb. 2020). "Large-scale Mixing in a Violent Oxygen-Neon Shell Merger Prior to a Core-collapse Supernova". In: *ApJ* 890.2, p. 94. DOI: 10.3847/1538-4357/ab66bb.

Yao, Y. et al. (Sept. 2020). "SN2019dge: A Helium-rich Ultra-stripped Envelope Supernova". In: *ApJ* 900.1, p. 46. DOI: 10.3847/1538-4357/abaa3d.

Zhang, J. et al. (Oct. 2020). "SN 2018zd: an unusual stellar explosion as part of the diverse Type II Supernova landscape". In: *MNRAS* 498.1, pp. 84–100. DOI: 10.1093/mnras/staa2273.

Chapter 4

WAVE-DRIVEN OUTBURSTS AND VARIABILITY OF LOW-MASS SUPERNOVA PROGENITORS

Wu, S. C. and J. Fuller (May 2022). "Wave-driven Outbursts and Variability of Low-mass Supernova Progenitors". In: *The Astrophysical Journal* 930.2, p. 119. DOI: 10.3847/1538-4357/ac660c.

4.1 Abstract

In a substantial number of core-collapse supernovae, early-time interaction indicates a dense circumstellar material (CSM) that may be produced by outbursts from the progenitor star. Wave-driven mass loss is a possible mechanism to produce these signatures, with previous work suggesting this mechanism is most effective for low mass ($\sim 11\,M_\odot$) SN progenitors. Using one-dimensional hydrodynamic simulations with MESA, we study the effects of this wave heating in SN progenitors of masses $M_{\rm ZAMS} = 10$–$13\,M_\odot$. This range encompasses stars that experience semi-degenerate, central neon burning and more degenerate, off-center neon ignition. We find that central Ne ignition at $M_{\rm ZAMS} = 11\,M_\odot$ produces a burst of intense wave heating that transmits $\sim 10^{47}$ erg of energy at 10 years before core collapse, whereas other masses experience smaller levels of wave heating. Wave heating does not hydrodynamically drive mass loss in any of our models and is unlikely to produce a very massive CSM on its own. However, wave heating can cause large radial expansion (by more than an order of magnitude), photospheric cooling, and luminosity brightening by up to $\sim 10^6\,L_\odot$ in hydrogen-poor stripped star models. Some type Ib/c progenitors could drastically change their appearance in the final years of their lives, with brightness in visual bands increasing by nearly 3 mags. Moreover, interaction with a close binary companion could drive intense mass loss, with implications for type Ibn and other interaction-powered SNe.

4.2 Introduction

A subset of core-collapse supernovae (SNe) across nearly all spectroscopic classes exhibit signatures of early interaction with circumstellar material (CSM). In such SNe, the CSM interaction is observed through fast-rising, bright early-time light curves; featureless, blue early spectra that signify a shock-heated envelope or CSM;

or narrow emission lines in early spectra that appear when nearby CSM is flash-ionized by the SN breakout. A few recent examples of SNe that demonstrate evidence for early interaction with CSM include the type II events SN2018zd (Zhang et al., 2020), SN2013fs (Yaron et al., 2017), and several type II events detected by ZTF (Bruch et al., 2021), as well as the type I events LSQ13ddu (Clark et al., 2020), SN2018gep (Ho et al., 2019), SN2019dge (Yao et al., 2020), SN2019uo (Gangopadhyay et al., 2020), and SN2019yvr (Kilpatrick et al., 2021). The CSM observed in these events is usually attributed to elevated mass loss from the progenitor stars that precedes the SN. For type II SNe with early peaks in the light curve, the CSM signatures may also be explained by roughly one solar mass of material in an optically thin stellar chromosphere or corona (Dessart, Hillier, and Audit, 2017; Hillier and Dessart, 2019).

Other events present late-time interaction and narrow emission lines, indicating mass loss occurring decades before the SN. Some recent examples include SN2017dio (Kuncarayakti et al., 2018), SN2017ens (Chen et al., 2018), SN2013L (Taddia et al., 2020), iPTF16eh (Lunnan et al., 2018), and SN2004dk (Mauerhan et al., 2018; Pooley et al., 2019). Many other events with both early- and late-time interaction are listed in Wu and Fuller (2021), Fuller and Ro (2018), and Fuller (2017).

While pre-SN outbursts have been observed directly in several SN progenitors (Ofek et al., 2014), the majority of SN progenitors may not experience pre-SN outbursts or amplified variability at all. Kochanek et al. (2017) found that progenitor constraints on nearby, well studied SNe do not support evidence for outbursts, and Johnson, Kochanek, and Adams (2017) found no significant variability in the progenitor for type Ic SN2012fh. Johnson, Kochanek, and Adams (2018) constrained variability amplitudes to less than $\sim$ 10% in four type II-P progenitors. As a result, the mechanisms behind pre-SN mass loss must operate such that they manifest a range in behavior, from elevated mass loss and bright pre-SN outbursts to no unusual variations at all.

One promising explanation for pre-SN outbursts is the wave heating model proposed by Quataert and Shiode (2012). Internal gravity waves (IGW) are excited as a routine consequence of convection, and the vigorous convection that occurs during late burning stages in massive stars may generate waves carrying more than $10^7\ L_\odot$ of power. These IGW couple with acoustic waves to deposit some of their power in the outer layers of the star, which may be able eject mass or drive outbursts. Shiode and Quataert (2014) found that more massive stars produced larger wave heating rates,

but ensuing outbursts occurred closer to core-collapse. Modeling the wave heating in a 15 $M_\odot$ red supergiant, Fuller (2017) found that waves could inflate the envelope and drive a mild outburst, potentially causing mass loss through a secondary shock. Fuller and Ro (2018) examined hydrogen-poor stars in which they found that wave heating could launch a dense, super-Eddington wind of $\dot{M} \sim 10^{-2}\, M_\odot/\mathrm{yr}$. These studies also predicted large variations in luminosity and temperature as a result of wave heating.

In Wu and Fuller (2021), we updated the physical model used for wave generation and propagation in Fuller (2017) and Fuller and Ro (2018) to include non-linear wave breaking effects and to more realistically model the wave spectrum excited by convection. By simultaneously accounting for these effects throughout the evolution of core convective shells in a suite of stars with $M_{\mathrm{ZAMS}} = 11$–$50\, M_\odot$, Wu and Fuller (2021) found that wave heating rates were an order of magnitude lower than adopted in prior work. While most models were unlikely to produce observable pre-SN outbursts, the lowest- and highest-mass stars experienced the highest levels of wave heating and were favored to drive outbursts. Leung, Wu, and Fuller (2021) surveyed the upper end of this mass range with the updated physics, extending up to $M_{\mathrm{ZAMS}} = 70\, M_\odot$ and including hydrogen-poor stars, and likewise predicted less energy deposited in the envelope and less mass loss than prior work. Their hydrodynamical simulations of the most energetic high-mass model ejected at most $0.01\, M_\odot$ of material close to core collapse, forming quite confined CSM.

In this paper, we study the low-mass end of models in Wu and Fuller (2021), where outbursts are promising due to semi-degenerate central neon ignition, and we now deposit the wave heat in our models as they evolve. We extend our scope down to $M = 10\, M_\odot$ stars to capture the physics of waves generated by semi-degenerate, off-center neon ignition. Additionally, we apply the same wave heating physics to hydrogen-poor models for stripped progenitors. In all our models, we add the wave heat and explore their hydrodynamical response. We find that our updated wave heating rates are not able to drive significant mass loss in either supergiant or stripped-star models and that wave heating only causes small-amplitude surface variability in our supergiant models. However, in our stripped star models we predict large outbursts in luminosity as well as large changes in the photospheric radius and surface temperature, which may be detectable in progenitors of type Ib SNe.

4.3 Implementation of wave physics in stellar models

Wave generation and propagation

To implement wave energy transport, we follow the procedure of Wu and Fuller (2021). We summarize the physics of wave generation and propagation here and refer the reader to Section 2 of Wu and Fuller (2021) for more details.

Gravity waves are excited at the interface between convective and radiative zones and carry a fraction of the kinetic energy of turbulent convection. While our understanding of this process remains incomplete, the power put into waves, $L_{\rm wave}$, is at least (Lecoanet and Quataert, 2013)

$$L_{\rm wave} = \mathcal{M}_{\rm con} L_{\rm con} \tag{4.1}$$

where $\mathcal{M}_{\rm con}$ is the MLT (mixing-length theory) convective Mach number and $L_{\rm con}$ is the convective luminosity (Goldreich and Kumar, 1990). We define the convective velocity $v_{\rm con}$ as

$$v_{\rm con} = \left(\frac{L_{\rm con}}{4\pi\rho r^2}\right)^{1/3}, \tag{4.2}$$

and we define the associated MLT convective turnover frequency as

$$\omega_{\rm con} = 2\pi \frac{v_{\rm con}}{2\alpha_{\rm MLT} H}, \tag{4.3}$$

where $\alpha_{\rm MLT} H$ is the mixing length and H is the scale height.

As in Wu and Fuller (2021), we use the power spectrum of waves over angular wavenumber ℓ from Goldreich and Kumar (1990) and Shiode et al. (2013) to calculate the proportion of wave energy generation per ℓ value, $\dot{E}_\ell / L_{\rm wave}$:

$$\frac{d\dot{E}_g}{d\ln\omega d\ln\ell} \sim L_{\rm wave} \left(\frac{\omega}{\omega_{\rm con}}\right)^{-a} \left(\frac{\ell}{\ell_{\rm con}}\right)^{b+1} \left(1 + \frac{\ell}{\ell_{\rm con}}\right) \times \exp\left[-\left(\frac{\ell}{\ell_{\rm con}}\right)^2 \left(\frac{\omega}{\omega_{\rm con}}\right)^{-3}\right]. \tag{4.4}$$

Here, $\ell_{\rm con} = r/\min(H, \Delta r)$ is evaluated at the edge of the convective zone and the predicted exponents are $a = 13/2$ and $b = 2$. This spectrum peaks near the value of $\ell_{\rm con}$ (see Figure 1 in Wu and Fuller 2021). As Equation 4.4 shows, the wave power drops off steeply for $\omega > \omega_{\rm con}$, and we do not expect low-frequency waves with $\omega < \omega_{\rm con}$ to contribute much wave power due to tunneling and damping effects described below. We therefore simplify the calculation by setting $\omega = \omega_{\rm con}$ for all ℓ values, and we normalize the power spectrum to $L_{\rm wave}$ so that $\sum \dot{E}_\ell = L_{\rm wave}$.

In the WKB limit, linear waves have the dispersion relation

$$k_r^2 = \frac{(N^2 - \omega^2)(L_\ell^2 - \omega^2)}{\omega^2 c_s^2}, \tag{4.5}$$

where N^2 is the squared Brunt-Väisälä frequency, k_r is the radial wavenumber, and $L_\ell^2 = \ell(\ell+1)c_s^2/r^2$ is the Lamb frequency squared. In the limit that $\omega \ll N, L_\ell$, this reduces to the gravity wave dispersion relation

$$k_r^2 = \frac{\ell(\ell+1)N^2}{\omega^2 r^2} \tag{4.6}$$

with group velocity

$$v_g = \omega^2 r / \sqrt{\ell(\ell+1)N^2}. \tag{4.7}$$

The limit $\omega \gg N, L_\ell$ gives acoustic waves, with dispersion relation

$$k_r^2 = \frac{\omega^2}{c_s^2} \tag{4.8}$$

and group velocity $v_g = c_s$. In either of these limits, linear waves propagate freely and approximately conserve their luminosity, apart from damping effects discussed below.

If $\omega > N$ and $\omega < L_\ell$ or vice versa, then the radial wavenumber is imaginary and waves are evanescent. The probability of tunneling through this evanescent zone, or the fraction of transmitted wave energy, is approximately given by the transmission coefficient

$$T^2 = \exp\left(-2\int_{r_0}^{r_1} |k_r| dr\right), \tag{4.9}$$

where the integral is taken over the evanescent zone. As the thickest evanescent zone dominates the wave reflection (see Appendix B2 of Fuller 2017), we take the minimum value of T^2 out of all evanescent zones, $T^2_{\rm min}$, to calculate the wave flux tunneling into the envelope. The remaining fraction $1 - T^2_{\rm min}$ of wave energy that encounters the evanescent region is reflected from the boundary of the evanescent zone.

In addition, after traveling to the upper edge of the core and back, a wave's energy is attenuated by the factor

$$f_\nu = \exp\left[2\int_{r_-}^{r_+} \frac{\gamma_\nu + \gamma_{\rm rad}}{v_g} dr\right] \tag{4.10}$$

where γ_ν and $\gamma_{\rm rad}$ are the neutrino and thermal wave energy damping rates, respectively, v_g is the gravity wave group velocity (Equation 4.7), and the integral is

taken over the upper and lower boundaries of the gravity wave cavity. Note that the definition of f_ν assumes the weak damping limit, where the majority of wave energy escapes only after traversing the core multiple times; in the limit of strong damping, where most of the wave energy escapes after traveling to the upper edge of the core once, it is appropriate to use $\sqrt{f_\nu}$ instead. We find that our models are almost always in the weak damping limit, especially when significant wave heating occurs, justifying our approximation for f_ν.

The fraction of wave energy that escapes the core, $f_{\mathrm{esc},\ell}$, is then determined by the transmission coefficient (Equation 4.9) and energy losses within the core,

$$f_{\mathrm{esc},\ell} = \left(1 + \frac{f_\nu - 1}{T_{\mathrm{min}}^2}\right)^{-1} . \tag{4.11}$$

Given the escape fraction, the ℓ-dependent power that escapes to heat the envelope is

$$L_{\mathrm{heat},\ell} = f_{\mathrm{esc},\ell} \dot{E}_\ell . \tag{4.12}$$

Equation 4.12 holds for waves that remain linear, but waves that experience non-linear wave breaking will experience another source of energy loss before escaping to heat the envelope. A measure of the gravity wave non-linearity as a function of ℓ is

$$|k_r \xi_r| = \left[\frac{2}{T_{\mathrm{min}}^2} \frac{f_{\mathrm{esc},\ell} \dot{E}_\ell N [\ell(\ell+1)]^{3/2}}{4\pi\rho r^5 \omega^4}\right]^{1/2} . \tag{4.13}$$

Where $|k_r \xi_r| \geq 1$, waves are non-linear, whereas linear waves have $|k_r \xi_r| \leq 1$. Such non-linear waves will break and experience an energy cascade to small scales, where their energy dissipates (Barker and Ogilvie, 2010). This effectively caps the wave amplitude ξ_r so that $|k_r \xi_r| \lesssim 1$, therefore reducing the wave power by a factor $|k_r \xi_r|^2$ when $|k_r \xi_r| \geq 1$. Thus for non-linear waves, the power that escapes to heat the envelope is effectively

$$\begin{aligned} L_{\mathrm{heat},\ell} &= f_{\mathrm{esc},\ell} \dot{E}_\ell / |k_r \xi_r|^2 \\ &= \frac{T_{\mathrm{min}}^2}{2} \frac{4\pi\rho r^5 \omega^4}{N [\ell(\ell+1)]^{3/2}} . \end{aligned} \tag{4.14}$$

We use the maximum value of $|k_r \xi_r|$ (i.e., the minimum value of the second line in Equation 4.14) in the g-mode cavity to compute the above reduction of wave power due to non-linear damping.

Wave dissipation

To model the wave damping and energy deposition in the envelope, we follow the methods of Fuller and Ro (2018), accounting for background flows as explained in their Section 3.4. We summarize the approach here.

Wave dissipation in the envelope can be understood by considering the damping mass, which is the mass through which a wave must pass to dissipate all its energy, given by

$$M_{\rm damp} = L_{\rm ac}\left(\frac{dL_{\rm heat,co}}{dm}\right)^{-1}. \tag{4.15}$$

in the presence of flows. Here $dL_{\rm heat,co}/dm$ is the wave heating rate per unit mass and $L_{\rm heat,co}$ is the wave energy flux measured in the comoving frame. The conserved quantity (in the absence of damping) in the inertial frame is the wave action $L_{\rm ac} = 2\pi r^2 \rho c_s u^2 (1 + v_r/c_s)$, where u is the radial velocity amplitude of the wave.

Fuller and Ro (2018) find that the damping mass due to radiative diffusion is

$$M_{\rm damp,rad} = \frac{2L_{\rm max}}{\omega^2 K}\left(1 + \frac{v_r}{c_s}\right)^2 \tag{4.16}$$

where the maximum possible wave flux in the linear regime is $L_{\rm max} = 2\pi r^2 \rho c_s^3$. Fuller and Ro (2018) find that the damping mass due to weak shock dissipation is

$$\begin{aligned} M_{\rm damp,shock} = &\frac{3\pi}{\gamma+1}\frac{L_{\rm max}}{\omega c_s^2} \\ &\times \left(\frac{L_{\rm max}\,(1+v_r/c_s)^5}{L_{\rm ac}}\right)^{1/2}. \end{aligned} \tag{4.17}$$

Thus the effective damping mass is

$$M_{\rm damp} = \left[M_{\rm damp,shock}^{-1} + M_{\rm damp,rad}^{-1}\right]^{-1}, \tag{4.18}$$

so that the energy deposited per unit time per unit mass in our models is

$$\epsilon_{\rm wave} = \frac{dL_{\rm heat,co}}{dm} = \frac{L_{\rm ac}}{M_{\rm damp}}. \tag{4.19}$$

Since $L_{\rm ac}$ is the quantity conserved in the absence of damping, we compute the energy deposited from escaping waves (with initial $L_{\rm ac} = L_{{\rm heat},\ell}$) as

$$\epsilon_{\rm wave} = L_{{\rm heat},\ell}/M_{\rm damp}. \tag{4.20}$$

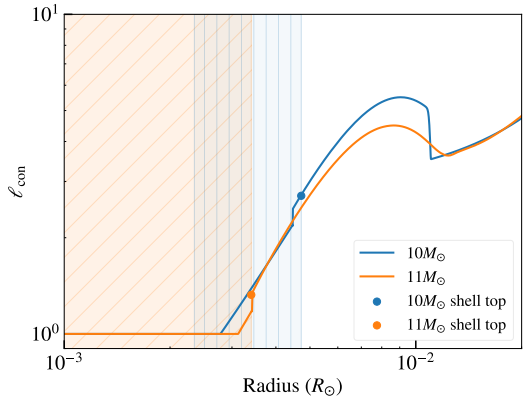

Figure 4.1: The value of $\ell_{\rm con} = r/\min(H, \Delta r)$ as a function of radius for the Ne burning convective region in the $10\,M_\odot$ (blue) and $11\,M_\odot$ (orange) supergiant models. The radial extent of the $10\,M_\odot$ burning shell is indicated by the blue shaded vertically hatched region, and the radial extent of the $11\,M_\odot$ core burning is shaded in orange with diagonal hatching. The radius of the top of the burning region, where $\ell_{\rm con}$ is evaluated, is marked with a circle for each model. Since the $10\,M_\odot$ model burns Ne off-center, the top of its Ne burning shell occurs at larger radius, increasing its $\ell_{\rm con}$ value. This also applies to the stripped star models.

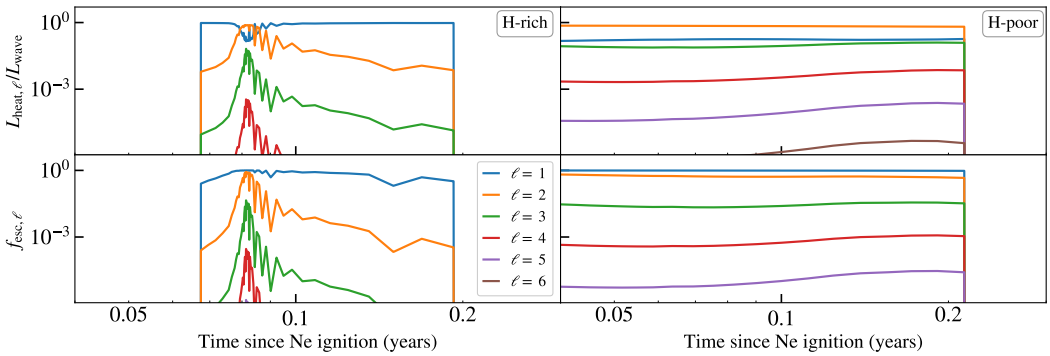

Figure 4.2: Fraction of envelope wave heating caused by each angular number ℓ (top), and the wave escape probability for each ℓ (bottom), as a function of time since Ne ignition in the $M_{\rm ZAMS} = 10\,M_\odot$ models. The left figure shows the supergiant model and the right figure shows the stripped star model. Results are only shown for waves where $L_{{\rm heat},\ell} > 10^3\,L_\odot$.

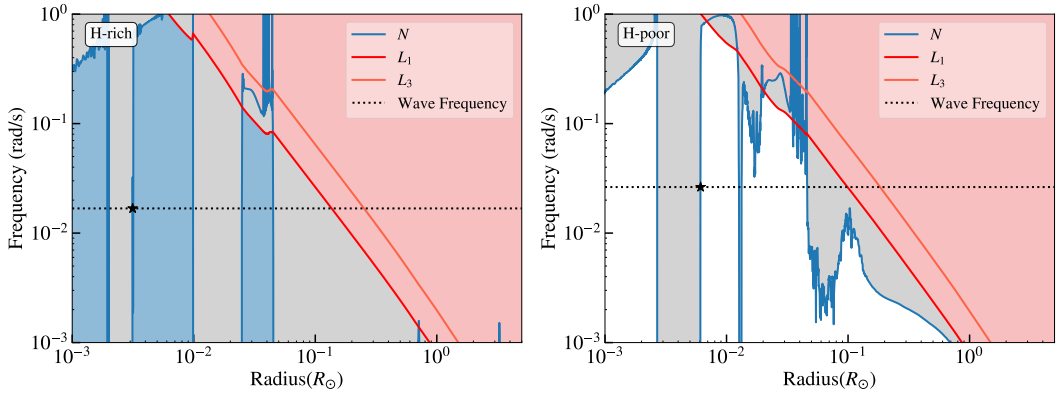

Figure 4.3: Propagation diagrams for the $M_{\rm ZAMS} = 10\,M_\odot$ supergiant model (top) and stripped star model (bottom), each during Ne burning. Shown are the Brunt-Väisälä frequency N (blue) and the Lamb frequency L_ℓ for $\ell = 1, 3$ (shades of red). Waves propagate through the gravity wave cavity (blue region) and into the envelope as acoustic waves (red region, shaded for $\ell = 1$), tunneling through evanescent zones (gray region) along the way. Off-center Ne ignition in the core excites waves with $\omega \sim 10^{-2}$ rad/s (dotted line) at the top of the convective zone (star). The stripped star model has higher ω, which allows the waves to tunnel through a thinner evanescent zone and causes the escape fraction to be higher for waves of all ℓ (Figure 4.2.)

Methods

We run a suite of MESA simulations (Paxton et al., 2011; Paxton et al., 2013; Paxton et al., 2015; Paxton et al., 2018; Paxton et al., 2019) for zero-age main sequence (ZAMS) masses 10, 10.5, 11, 12, and 13 $M_\odot$ and evolve the stars from the main sequence to at least five years after neon (Ne) ignition. For the 11–13 $M_\odot$ models, we evolve the stars until core collapse; however, the 10 and 10.5 $M_\odot$ models experience off-center Ne burning that makes these stars prohibitively computationally expensive to run until core collapse, so we simulate these models through Ne ignition and at least five years of Ne burning flame propagation. In addition, we create hydrogen-poor (H-poor) stellar models following the methods of Fuller and Ro (2018), Appendix A[1]. Starting with models of the same initial masses ($M_{\rm ZAMS}$) as the aforementioned hydrogen-rich (H-rich) supergiant models, we remove the hydrogen envelope after core helium (He) burning so that the resulting H-poor, stripped star models have nearly the same He core masses as the H-rich models. Accordingly, the stripped star models with initial mass 10 and 10.5 $M_\odot$ experience the same off-center Ne ignition as their supergiant counterparts, while all other

[1]Model parameters are available on Zenodo at 10.5281/zenodo.6147842.

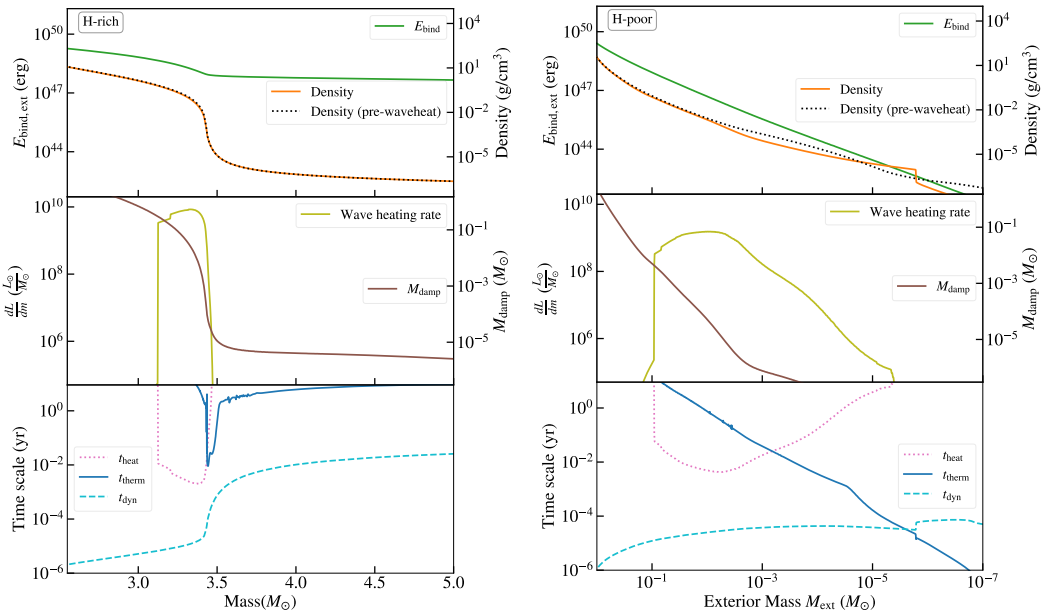

Figure 4.4: **Left panel**: Wave heating diagnostics for an 11 $M_\odot$ red supergiant model during Ne burning as a function of mass coordinate. **Top**: Binding energy integrated inward from the surface of the model and the star's density profile, before and after wave heating due to Ne burning. **Middle**: Wave energy deposition rate per unit mass and the damping mass (i.e., $4\pi\rho r^2$ times the damping length, Equation 4.18). **Bottom**: Wave heating timescale ($t_{\rm heat}$), local thermal timescale ($t_{\rm therm}$), and local dynamical timescale ($t_{\rm dyn}$). **Right panel**: Same as left for the $M_{\rm ZAMS} = 11\,M_\odot$ stripped star during Ne burning, but as a function of exterior mass coordinate.

stripped star models are evolved until core collapse.

Beginning at core carbon burning, we capture the wave-driven mass loss as in Fuller and Ro (2018) by setting the outer boundary at an optical depth of $\tau = 10^{-2}$. Material that flows past this outer boundary is removed from the grid, and we define mass loss rates in the paper as the mass flux through this outer boundary. At each timestep, we perform the same calculations described in Section 2.2 of Wu and Fuller (2021) and above for the convective burning regions in each model. This gives us the amount of wave heat transmitted, including possible non-linear effects. We then add the wave heat in each cell of the model using Equation 4.19.

4.4 Results

Wave heating rates

In all our models, the most important contribution to wave heating occurs during Ne burning roughly 5 – 20 years before core collapse. The next major contribution

to wave heating from Si burning is energetic, but occurs too near core collapse for waves excited by Si burning to reach the surface of our supergiant progenitors. We do not simulate Si burning in our $M < 11\,M_\odot$ models.

The $M < 11\,M_\odot$ models in this work extend our wave heating study down to lower-mass stars in which Ne ignites off-center. This difference greatly affects the amount of wave power produced by the 10–10.5 $M_\odot$ supergiant models, bringing the wave energy deposition rate down by 1–2 orders of magnitude compared to the less degenerate and centrally burning 11 $M_\odot$ model (see Figure 4.6, top left panel). The main reduction in wave heating arises from lower wave escape fractions from the core occurs because the excited wave spectrum peaks at higher angular wavenumber than the central burning models. As described in Section 4.3 and in more detail in Wu and Fuller (2021), the peak of the wave spectrum in angular wavenumber ℓ occurs for $\ell \gtrsim \ell_{\rm con} = r/\min(H, \Delta r)$, which is evaluated at the top of the burning shell. Figure 4.1 shows how the decrease in scale height H with radius causes the value of $\ell_{\rm con}$ to increase rapidly as a function of radius in both a centrally burning (11 $M_\odot$) and off-center burning (10 $M_\odot$) model. Since the off-center burning shell extends to larger radii than a core burning region, waves excited due to Ne burning in a 10 $M_\odot$ model peak at higher ℓ. For the snapshot shown, $\ell_{\rm con} \sim 3$ for the 10 $M_\odot$ model so its wave spectrum typically peaks at around $\ell \sim 4$, while $\ell_{\rm con} \sim 1.5$ for the 11 $M_\odot$ model so its wave spectrum typically peaks around $\ell \sim 2$–3.

The bottom left panel of Figure 4.2 demonstrates that the escape fraction is many orders of magnitude smaller for high-ℓ waves, shown here for a 10 $M_\odot$ supergiant model but also generally true in all our models. Hence, when the wave spectrum peaks at higher ℓ, more of the initial wave power $L_{\rm wave}$ is distributed to waves that can only escape with a tiny fraction of their original power. The ultimate heating rate $L_{{\rm heat},\ell}$ is dominated by low ℓ waves which only carry $\dot{E}_\ell \lesssim 0.1\,L_{\rm wave}$ (top left panel of Figure 4.2). Since off-center burning excites a wave spectrum that peaks at higher ℓ, wave heating is thus strongly reduced.

For the most part, convective excitation of waves in the stripped star models matches that of the supergiant stars, as expected given their nearly equal He core masses. Nevertheless, subtle structural differences in the stripped star models can modify their wave heating rates. In our stripped star models, Ne ignites at a different temperature $T_{\rm burn,Ne}$ than in the supergiant models. Though both the $M_{\rm ZAMS} = 10\,M_\odot$ stripped star and supergiant models ignite off-center at similar radii, the stripped star model is a little denser and hotter at the center compared to the

supergiant when Ne burning begins. Given slightly higher $T_{\rm burn,Ne}$, convection in the temperature-sensitive Ne burning shell is more energetic, which raises $L_{\rm con}$, $\mathcal{M}_{\rm con}$ and consequently $L_{\rm wave}$ by a factor of a few in the stripped star.

More vigorous core convection also produces higher ω, which affects the escape fraction of the $M_{\rm ZAMS} = 10\,M_\odot$ stripped star. Comparing the left and right panels of Figure 4.2, we see that $f_{{\rm esc},\ell}$ is generally higher during Ne burning for the $M_{\rm ZAMS} = 10\,M_\odot$ stripped star. Figure 4.3 shows propagation diagrams for the $M_{\rm ZAMS} = 10\,M_\odot$ supergiant and stripped star models during Ne burning for typical wave frequencies. The stripped star model tends to excite higher ω by a factor of two, and as demonstrated in the figure, these waves encounter smaller evanescent zones. Thus waves have a larger transmission coefficient $T^2_{\rm min}$ and a larger escape fraction in the stripped star. The combination of increasing both $f_{{\rm esc},\ell}$ and $L_{\rm wave}$ accordingly raises the wave energy deposited in the envelope by an order of magnitude in the $M_{\rm ZAMS} = 10\,M_\odot$ stripped star (see Figure 4.6) relative to the H-rich model. For other masses, the difference in wave heating rates between H-rich and H-poor models is much smaller and stems mainly from slight differences in the core structure that affect $T_{\rm burn,Ne}$ and consequently $L_{\rm wave}$ as discussed above.

As discussed in Wu and Fuller (2021), our updated implementation of wave physics tends to reduce our wave heating rates by an order of magnitude compared to earlier results such as Fuller (2017) and Fuller and Ro (2018). Prior work did not model non-linear wave dissipation and assumed that wave power was mainly excited in $\ell = 1$ waves. In particular, the wave heating history of our models is now dominated by a brief burst of very high $L_{{\rm heat},\ell}$ waves excited during Ne burning. We do not produce high wave power sustained for longer periods, such as that during core O burning sustained for ~ 1 yr in Fuller (2017) and Fuller and Ro (2018).

Wave dissipation

Both the lower energy scale and sudden, short-duration nature of wave heating influence the hydrodynamical response of our models' interior structures. In the left column of Figure 4.4, the density and exterior binding energy of the $11\,M_\odot$ supergiant star are plotted as a function of mass coordinate for a model during Ne burning where the instantaneous wave power is $\sim 10^9\,L_\odot$. The density and effective $M_{\rm damp}$ (middle panel) drop at the core-envelope transition in the star, so that most of the waves damp their energy at the base of the supergiant envelope at around $M \sim 3.4 M_\odot$. Wave energy is therefore deposited where the binding

energy of overlying material is still high, $E_{\rm bind} \sim 10^{48}$ erg $> E_{\rm waves}$ (see Figure 4.6, top panel for $E_{\rm waves}$). The density profile of the supergiant star experiences only minuscule changes due to wave heating, and the deposited wave energy is unable to unbind the overlying envelope mass. Waves in the other supergiant models, which carry much less energy into the envelope than the 11 $M_\odot$ model, likewise deposit their energy without unbinding any material or greatly affecting the density profile of the star.

Our stripped star models lack an overlying hydrogen envelope, so the binding energy is smaller at the edge of the core, as shown in the right panel of Figure 4.4. Waves again damp most of their energy where the damping mass drops outside the core, which for a stripped star is very close to the surface with only $M_{\rm ext} \sim 10^{-2}\,M_\odot$ of overlying mass. For the $M_{\rm ZAMS} = 11\,M_\odot$ model shown in Figure 4.4, waves with a typical heating rate of $L_{{\rm heat},\ell} \gtrsim 10^9\,L_\odot$ still damp out where $E_{\rm bind} \sim 10^{48}$ erg $> E_{\rm waves}$ since $M_{\rm damp}$ is smaller for such large $L_{{\rm heat},\ell} = L_{\rm ac}$ (Equation 4.17). Thus the waves excited by Ne burning are not able to unbind the $M_{\rm ext} \sim 10^{-3}$–$10^{-2}\,M_\odot$ of exterior material. Unlike the supergiant models, however, the envelope of this stripped star model inflates above the heating region, flattening the density profile. In the other stripped star models, where the wave energy deposited is at least a few times lower (Figure 4.6), smaller $L_{{\rm heat},\ell}$ leads to larger $M_{\rm damp}$, so waves damp further out where $E_{\rm bind} \sim 10^{47}$ erg. Again, $E_{\rm wave} \lesssim E_{\rm bind}$ where the waves damp, so waves are also not able to unbind the overlying envelope in the other stripped star models.

The bottom panels of Figure 4.4 show the following timescales for the $M_{\rm ZAMS} = 11\,M_\odot$ supergiant (left) and stripped star (right): the local wave heating timescale,

$$t_{\rm heat} = \frac{c_s^2}{\epsilon_{\rm wave}} \tag{4.21}$$

where $\epsilon_{\rm wave}$ is defined in Equation 4.19; the thermal cooling timescale,

$$t_{\rm therm} = \frac{4\pi\rho r^2 H c_s^2}{L} \tag{4.22}$$

where L is the local luminosity; and the local dynamical timescale,

$$t_{\rm dyn} = \frac{H}{c_s}. \tag{4.23}$$

Both the supergiant and stripped star models lie in the moderate heating regime where $t_{\rm dyn} < t_{\rm heat} < t_{\rm therm}$. Wave heat is not transported outward thermally, but the local pressure will gradually increase and the star will expand quasi-hydrostatically

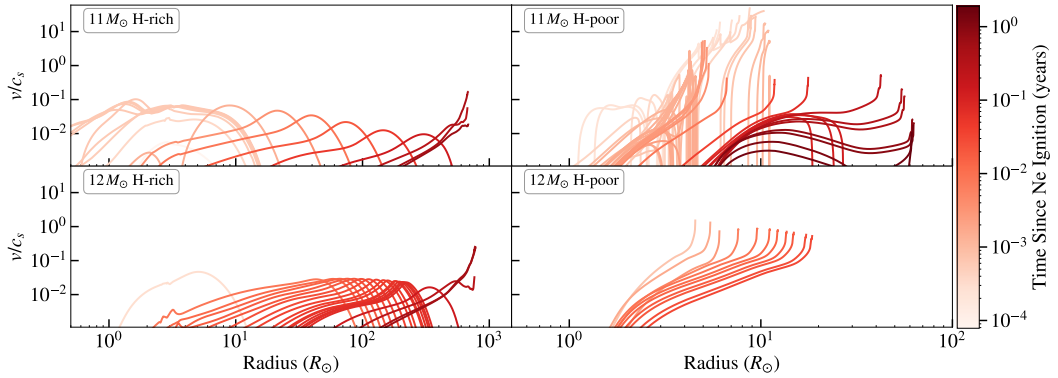

Figure 4.5: Velocity pulse propagation due to first wave heating phase from Ne ignition in the following models, clockwise from top left: $M_{\rm ZAMS} = 11\,M_\odot$ supergiant model, $M_{\rm ZAMS} = 11\,M_\odot$ stripped star model, $M_{\rm ZAMS} = 12\,M_\odot$ stripped star model, $M_{\rm ZAMS} = 12\,M_\odot$ supergiant model. Shading corresponds to the time since Ne ignition.

in response. This result differs from Fuller (2017), which also treated wave heating in a supergiant model. Fuller (2017) found $t_{\rm heat}$ could become shorter than both $t_{\rm therm}$ and $t_{\rm dyn}$ during Ne burning, so that wave heating entered a dynamical regime and launched a pressure wave propagating at the sound speed. The difference arises because Fuller (2017) do not include the weak shock dissipation introduced in Fuller and Ro (2018). For our supergiant models with weak shock dissipation, this reduces the effective $M_{\rm damp}$ of our models compared to Fuller (2017) and causes the waves to damp at smaller mass coordinates with smaller values of $t_{\rm dyn}$. As a result, the supergiant models now lie in the moderate heating regime. Our stripped star models remain consistent with Fuller and Ro (2018), who also find that $t_{\rm dyn} < t_{\rm heat} < t_{\rm therm}$ in the wave heating region.

Pre-supernova evolution

Once wave heat is deposited in our supergiant models, a small fraction of the energy is put into the kinetic energy of a velocity pulse (i.e., a pressure wave) that travels across the envelope of the star. The left column of Figure 4.5 shows the propagation of the velocity pulse due to wave heating from Ne burning in the 11 $M_\odot$ and 12 $M_\odot$ supergiant models. The pulse does not exceed $v/c_s \sim 0.1$ in either model until it steepens at the surface of the supergiants to $v/c_s \sim 0.2$. The stars otherwise expand quasi-hydrostatically in response to this velocity pulse. As the surface velocities are quite small, with $v < v_{\rm esc}$ in all the supergiant models, the surfaces of these stars expand slightly but remain bound.

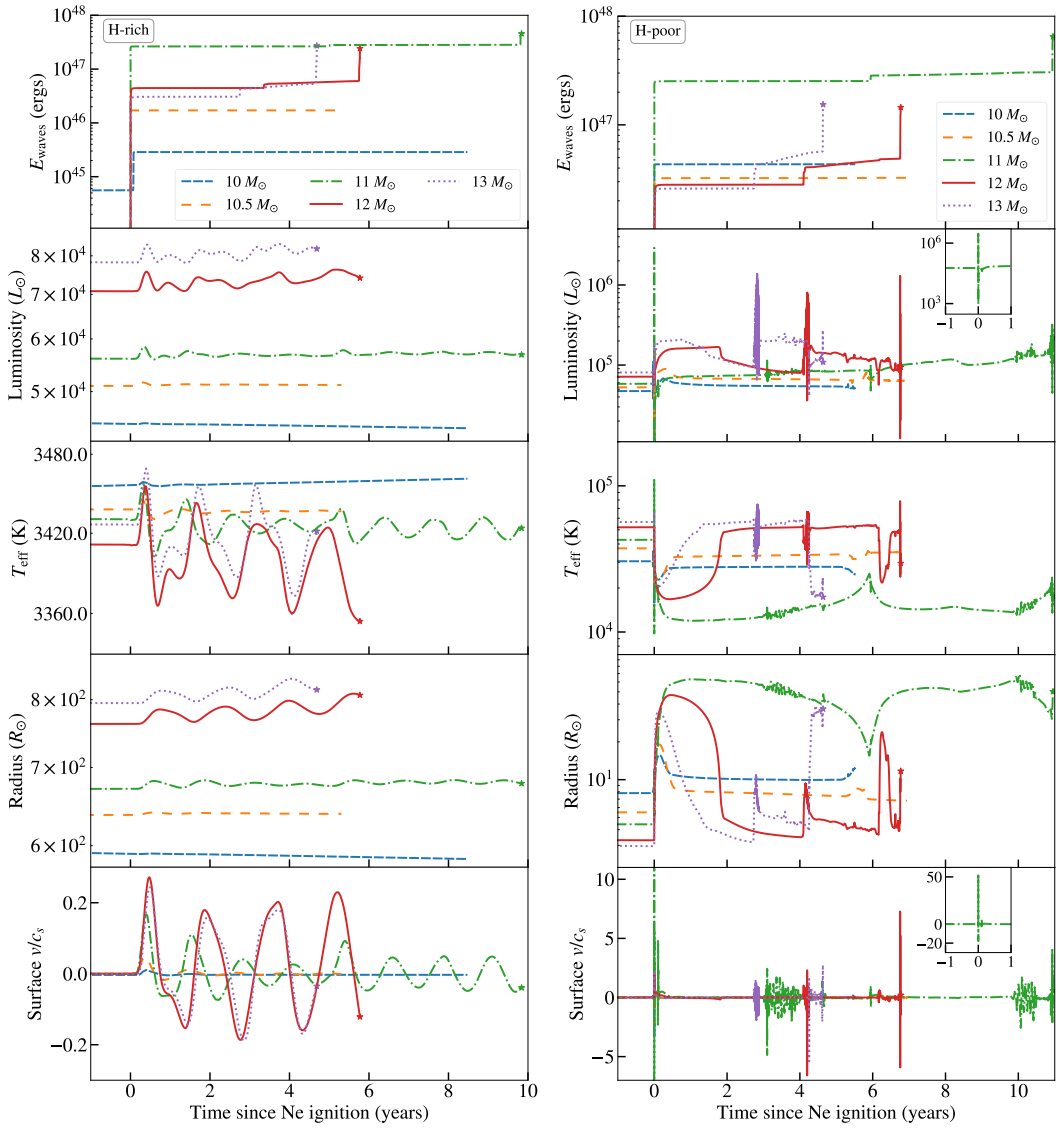

Figure 4.6: **Left**: Integrated wave energy deposited, surface luminosity, effective temperature, star radius, and surface velocity as a function of time since Ne ignition for the supergiant models shown in the legend. **Right**: Same as left panel for the stripped star models with initial masses as shown in the legend. For models that reach core collapse, indicated by the star symbol at the end of each curve, the evolution is shown until 3 days before core collapse.

Note that in our supergiant models, although more wave heat is deposited in the envelope of the 11 $M_\odot$ model and its pressure pulse initially has more kinetic energy, peaking at $v/c_s \sim 0.1$, the kinetic energy in the pulse decreases greatly as it propagates so that the surface velocity of the 11 $M_\odot$ model is smaller than that of the 12 $M_\odot$ model. In contrast, the pulse in the 12 $M_\odot$ supergiant model begins with a lower peak value because a few times less wave energy was deposited, but it only experiences a very shallow decline before it steepens at the surface. We attribute this counter-intuitive result to the different profiles of $t_{\rm therm}$ in the models. As seen in the bottom panel of Figure 4.4, $t_{\rm therm}$ decreases by a few orders of magnitude at $m \sim 3.5\,M_\odot$, just above the wave heating region at the base of the convective envelope. This dip occurs where the convective flux increases in response to the extra deposited energy (see Section 4.5 for a discussion of this phenomenon). In the 11 $M_\odot$ model, the small $t_{\rm therm}$ in this location may allow the convective flux to carry away some energy from the pulse, causing the velocity to decline as in Figure 4.5. The value of $t_{\rm therm}$ drops less steeply in the 12 $M_\odot$ model, so the local luminosity is not as efficient in carrying energy away from the pressure pulse. As the other models all deposit less wave energy, their velocity pulses emulate the 12 $M_\odot$ model in this respect.

In the $M_{\rm ZAMS} = 11\,M_\odot$ stripped star model shown in the top right of Figure 4.5, the heating generates a rapid expansion with Mach number $\mathcal{M} \sim 50$ near the surface of the star. The response of convection to wave-heating as described above for the supergiants does not apply for the stripped stars, since they lack a convective hydrogen envelope. In the $M_{\rm ZAMS} = 12\,M_\odot$ model (shown in the bottom right of Figure 4.5), less wave heat is deposited and the velocity pulse accelerates to lower values of $\mathcal{M} \sim 2$. This is representative of the other stripped star models, which deposit comparable amounts of wave energy. Each pressure wave breakout corresponds to spikes in luminosity and effective temperature and initiates rapid envelope expansion of the stripped stars. However, only the expansion driven by the most energetic $M_{\rm ZAMS} = 11\,M_\odot$ model directly after Ne ignition accelerates any stellar material to $v_{\rm esc} \sim 400$ km/s, and only a very small amount of mass ($M \sim 10^{-6} M_\odot$) achieves that velocity. The other stripped star models expand without ejecting any mass.

Figure 4.6 shows the evolution of the surface properties of our models, in parallel with the integrated wave energy deposition as a function of time since Ne ignition. In the supergiant models, the surface luminosity L, effective temperature $T_{\rm eff}$, radius R,

and surface velocity oscillate from Ne ignition onward. Wave heating from Ne ignition initiates these oscillations, which persist until core collapse for the 11–13 $M_\odot$ models. The amplitude of these fluctuations is small, ranging from almost no variation in the 10 $M_\odot$ model where $E_{\rm wave} \sim 10^{45}$ erg to oscillation amplitudes of a few percent in the 10.5–13 $M_\odot$ models with 10–100 times more wave heating.

Though our stripped star models mostly deposit comparable amounts of energy in the envelope, the surface properties of these models behave extremely differently from their supergiant counterparts. The initial pressure pulse breakout originating from wave heating due to Ne ignition generates upward spikes in L by a factor of a few for most models, although the luminosity of the most energetic $M_{\rm ZAMS} = 11\ M_\odot$ model temporarily jumps by over an order of magnitude. The luminosity in each model also tends to spike downward briefly before becoming brighter than before wave heating began. Overall, the stripped star models exhibit significant photospheric cooling and expansion, where $T_{\rm eff}$ drops by up to a factor of a few and the radius of the star rapidly increases by up to an order of magnitude. The properties of the lowest-mass $M_{\rm ZAMS} = 10$–$10.5\ M_\odot$ models change less dramatically; for instance, these models expand only by a factor of 2–3.

After Ne ignition, a second step-like increase in $E_{\rm waves}$ occurs for the $M_{\rm ZAMS} = 11$–$13\ M_\odot$ models at a few years after Ne ignition. This is due to a second surge of wave heating from core Ne burning, since the burning fuel is replenished when some Ne is mixed downward into the core. This tends to initiate another cooling and expansion phase in the stripped stars, so that over the period between Ne ignition and core collapse, the models exhibit two bumps in radius and dips in $T_{\rm eff}$. In the $M_{\rm ZAMS} = 12$–$13\ M_\odot$ models, the first cool, expanded phase lasts $\sim$ 1–2 years before returning to near pre-wave heating values; meanwhile, the second Ne burning phase causes the stars to expand less dramatically for a brief period of months. However, these phases last for ~ 5 years each in the $M_{\rm ZAMS} = 11\ M_\odot$ model, attaining a similar peak radius and $T_{\rm eff}$ each time.

Note that this second burning phase also causes spikes in L and $T_{\rm eff}$ for the $M_{\rm ZAMS} = 12$–$13\ M_\odot$ stripped star models at around 5 and 3 years since Ne ignition, respectively. The models oscillate in L and $T_{\rm eff}$ because the Ne abundance in the core is fluctuating. This drives oscillations in the burning rate and $L_{\rm con}$, which in turn causes the wave heating rate and surface properties to fluctuate. Increasing the resolution of our models did not consistently remove this effect, so it is unclear whether this effect is physical or numerical in nature. Different treatments of convective

overshoot could affect the core Ne abundance as well.

Although we predict little hydrodynamically driven mass loss, the large changes in surface luminosity exhibited by the stripped star models affects the wind mass loss rates of these stars. Using the following wind mass loss rate from Nugis and Lamers (2000),

$$\begin{aligned}\log \dot{M}_{\rm wind} = &-11 + 1.29 \log L \\ &+ 1.73 \log Y + 0.47 \log Z,\end{aligned} \tag{4.24}$$

we calculate the expected mass loss rate from winds in each of the stripped star models due to their elevated luminosity after Ne burning. We find that the increased mass loss from winds is an order of magnitude larger than directly ejected material, but still very small. The wind mass loss rates in our models peak at $\dot{M} \sim 10^{-5}\, M_\odot$/yr, and the models lose a few$\times 10^{-5}\, M_\odot$ between Ne ignition and core collapse.

4.5 Discussion

Parameter testing

To investigate how our results may vary if our assumptions about wave power and frequency do not accurately represent the true values, we ran simulations with different values for $L_{\rm wave}$ (Equation 4.1) and ω (Equation 4.3). For each model in Figure 4.6, we repeated the methods of Section 4.3, each time making one of the four following changes:

1. $\omega = 3\omega_{\rm con}$
2. $\omega = 0.3\omega_{\rm con}$
3. $L_{\rm wave} = 3\mathcal{M}_{\rm con} L_{\rm con}$
4. $L_{\rm wave} = 0.3\mathcal{M}_{\rm con} L_{\rm con}$.

These variations allow us to test how our results would change if our initial assumptions for the power and frequency of the excited waves either overestimate or underestimate reality. With these simulations along with our original models, we span an order of magnitude of uncertainty in these initial assumptions. Note that we do not change our assumed wave spectrum for these tests, so changes in ω only affect the dispersion relation and related quantities outlined in Section 4.3.

Figure 4.7 shows how the wave energy that escapes to heat the envelope changes as we vary these parameters in each model. We omit $M_{\rm ZAMS} = 10.5\, M_\odot$ as its

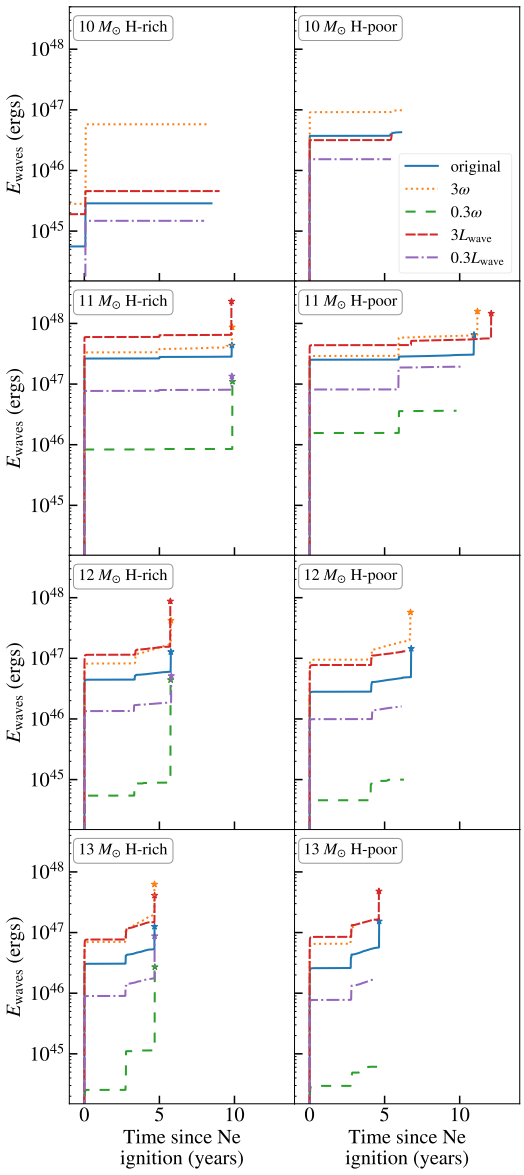

Figure 4.7: Integrated wave energy deposited as a function of time since neon ignition for supergiant (left column) and stripped star (right column) models with the initial masses shown in each panel. Each panel shows the variation in wave energy deposition for each model as either the wave frequency (Equation 4.3) or the power put into waves (Equation 4.1) is increased and decreased by a factor of 3. As in Figure 4.6, models that reach core collapse are indicated by the star symbol at the end of each curve.

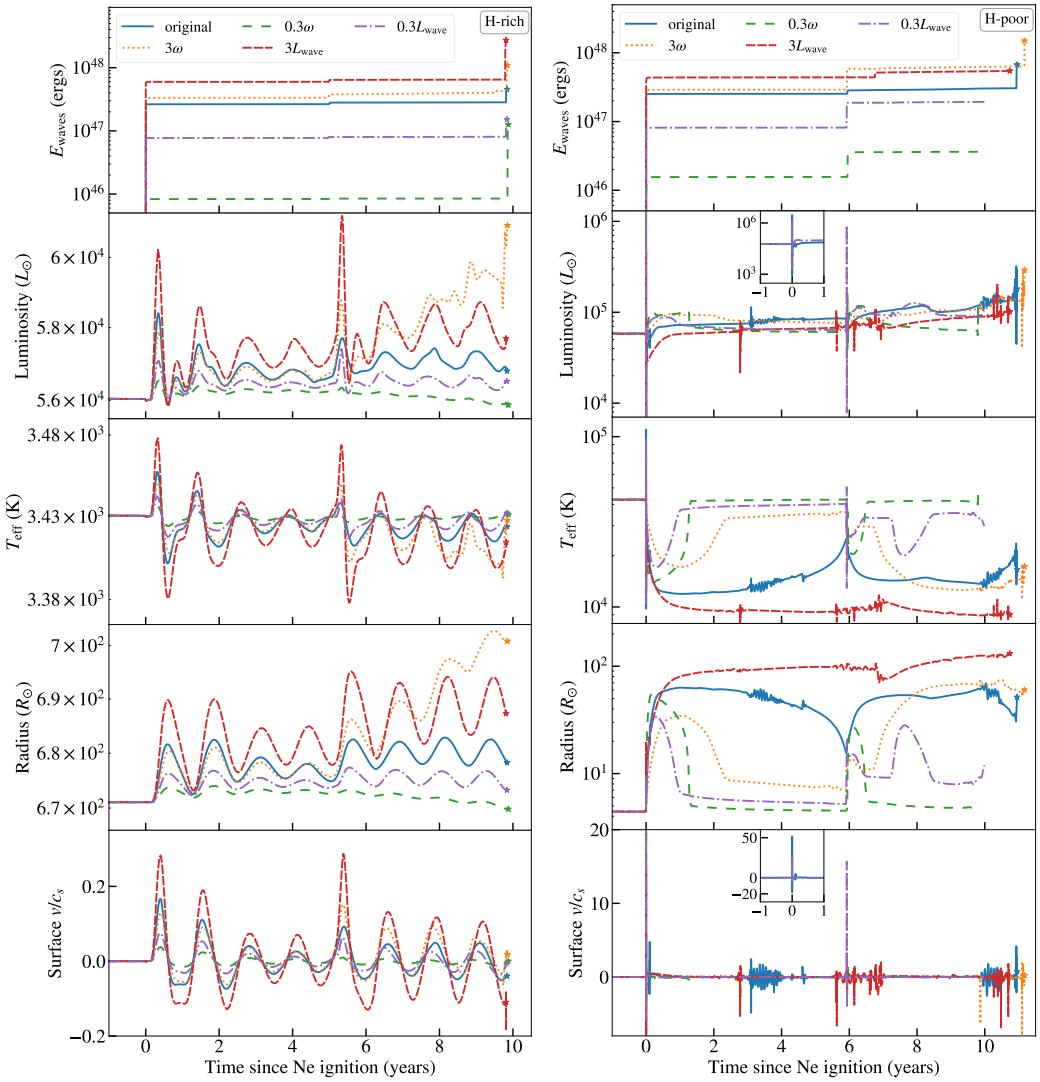

Figure 4.8: **Left**: Same quantities as in Figure 4.6 are shown for an 11 $M_\odot$ supergiant model. As in Figure 4.7, each panel plots the different evolution of each model as either the wave frequency or power is varied (see Section 4.5 for details). **Right**: Same as left for the $M_{\rm ZAMS}$ = 11 $M_\odot$ stripped star model. As in Figure 4.6, models that reach core collapse are indicated by the star symbol at the end of each curve.

evolution due to off-center Ne ignition proceeds similarly to $M_{\rm ZAMS} = 10\,M_\odot$. For all models, the wave heating history remains the same–jumps in $E_{\rm waves}$ occur at the same times, as changing $L_{\rm wave}$ or ω has no bearing on when the model develops convective regions. As noted in Wu and Fuller (2021), wave energy transmission in the mass range 11–15 $M_\odot$ is not significantly altered by non-linear effects, so for these models the wave energy escape generally increases (decreases) by a factor of three as we increase (decrease) $L_{\rm wave}$ by a factor of three. However, the $3L_{\rm wave}$ variations upon each of the $M_{\rm ZAMS} = 10\,M_\odot$ models and the $M_{\rm ZAMS} = 11\,M_\odot$ stripped star model do not show as large of an increase in wave energy; in fact, slightly less wave energy escapes for the $M_{\rm ZAMS} = 10\,M_\odot$, $3L_{\rm wave}$ variation than the original run. This is due to non-linear effects in these models–increasing $L_{\rm wave}$ also increases the wave non-linearity $|k_r\xi_r|^2$ by the same factor, which for non-linear waves effectively reduces the wave power back to that of the original run.

Changing ω affects the escape fraction and wave non-linearity. In the core, higher frequency waves will experience less attenuation due to neutrino and thermal losses in the g-mode cavity, and they have larger escape fractions. The non-linearity factor goes as $|k_r\xi_r|^2 \propto \omega^{-4}$, so higher frequency waves are much less non-linear. Thus, we ultimately find that increasing (decreasing) wave frequency increases (decreases) the wave energy escape, in some models more drastically than others depending on the magnitude of the change in $f_{{\rm esc},\ell}$ and whether non-linear effects are important for those waves.

The variation in surface properties as we vary ω and $L_{\rm wave}$ is shown for an 11 $M_\odot$ supergiant model in the left panel of Figure 4.8. All the models exhibit oscillations of varying amplitude which persist until core collapse, with larger jumps occurring soon after wave heating episodes. The amplitude of the oscillation tends to be larger for variations with more wave heating such as $3L_{\rm wave}$ and 3ω and much smaller for less energetic models like $0.3L_{\rm wave}$ and 0.3ω. Moreover, the more energetic runs tend towards larger L and R and smaller $T_{\rm eff}$ than the original run, whereas the surface properties of the less energetic variations deviate less from the quiescent values than the original run.

In contrast, the stripped star with $M_{\rm ZAMS} = 11 M_\odot$ exhibits much larger changes in its surface properties due to the variations in ω and $L_{\rm wave}$ (Figure 4.8, right panel). The luminosity may vary by a factor of ∼2 in either direction compared to the original run, but more energetic models (larger $L_{\rm wave}$ or ω) are generally brighter, with larger photospheric radii and lower temperatures. The $3L_{\rm wave}$ run cools and expands

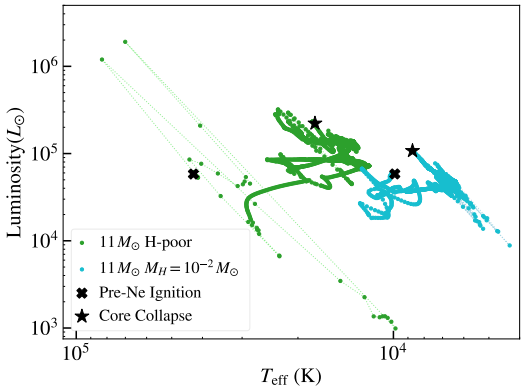

Figure 4.9: Evolution on the Hertzsprung-Russell diagram for the H-poor $M_{\rm ZAMS}$ = 11 $M_\odot$ model (green) and a $M_{\rm ZAMS}$ = 11 $M_\odot$ stripped star model with M_H = 10^{-2} $M_\odot$ (cyan) from just before Ne ignition (cross) until core collapse (star). Each dot is separated by an interval of 1 hour.

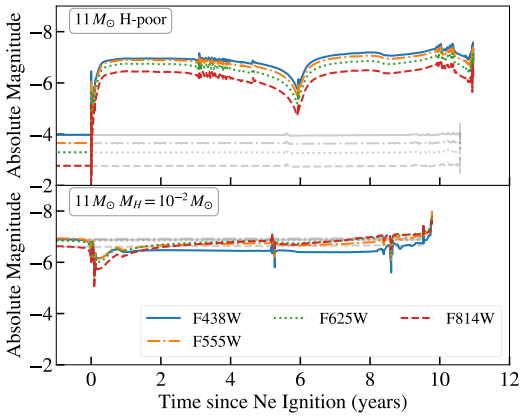

Figure 4.10: **Top**: Evolution of absolute magnitude (AB mag) in four HST bandpasses as a function of time since Ne ignition for the H-poor $M_{\rm ZAMS}$ = 11 $M_\odot$ model. The absolute magnitudes of the same model with no wave heating are plotted in gray, with line styles corresponding to the same line styles of each bandpass in the legend. **Bottom**: Same for a $M_{\rm ZAMS}$ = 11 $M_\odot$ stripped star model with M_H = 10^{-2} $M_\odot$.

more than the original run right after Ne ignition, remaining larger and cooler than all other runs until core collapse. In the least energetic $0.3L_{\rm wave}$ and 0.3ω runs, wave heating causes the star to initially cool by a factor of $\sim$ 2–2.5 and expand to tens of $R_\odot$ before returning to radii and temperatures near that of quiescence after about a year. The behavior of the 11 $M_\odot$ models shown in Figure 4.8 qualitatively represents that of the other masses, though variations in the 10 $M_\odot$, 10.5 $M_\odot$, 12 $M_\odot$, and 13 $M_\odot$ models are on somewhat smaller scales since less wave heat is deposited in the envelopes of those models.

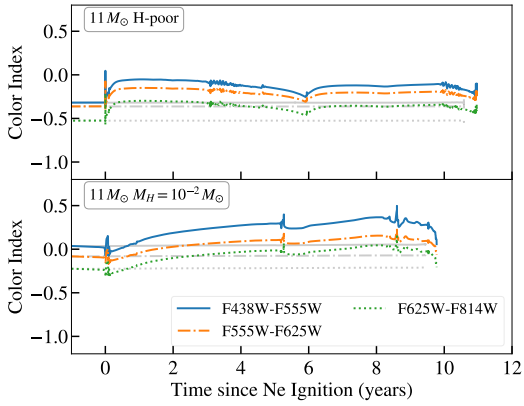

Figure 4.11: **Top**: Evolution of several color indices (AB mag) as a function of time since Ne ignition for the H-poor $M_{\rm ZAMS} = 11\ M_\odot$ model. The colors of the same model with no wave heating are plotted in gray, with line styles corresponding to the same line styles of each bandpass in the legend. **Bottom**: Same for a $M_{\rm ZAMS} = 11\ M_\odot$ stripped star model with $M_H = 10^{-2}\ M_\odot$.

Comparison with progenitor observations

Since the changes in the surface properties of our supergiant models are quite small, we do not expect a large observational signature of wave heating in these stars. However, our stripped star models start out as hot, compact He stars, but expand greatly and become cooler for years due to wave heating. Figure 4.9 shows the evolution of the $M_{\rm ZAMS} = 11\ M_\odot$ stripped star model on the HR diagram from just before Ne ignition until core collapse. A model without wave heat would remain at the point labeled "Pre-Ne Ignition" on the green curve in Figure 4.9 until core collapse. In contrast, the star initially moves to large L and $T_{\rm eff}$, then to small L and $T_{\rm eff}$, over a few hours when the shock launched by wave heating breaks out. It then spends months moving to a more luminous but cooler state. The star remains in that region of the HR diagram for years, with some continued variability due to fluctuating amounts of wave heat emerging from the core.

The top panel of Figure 4.10 shows lightcurves in four *Hubble Space Telescope* WFC3/UVIS bands as a function of time since Ne ignition for this model. Each absolute magnitude was calculated by integrating over a blackbody at $T_{\rm eff}$ convolved with the transmission function for each bandpass filter and is reported in AB magnitudes. The brightness in all bands jumps once wave heating begins at Ne ignition. Note that the bolometric absolute magnitude will only decrease by $\sim$1, but the visual band magnitudes decrease by $\sim$3 magnitudes. This is a consequence of the star cooling from $\approx$40,000 K to $\approx$15,000 K, causing a much larger fraction of its flux

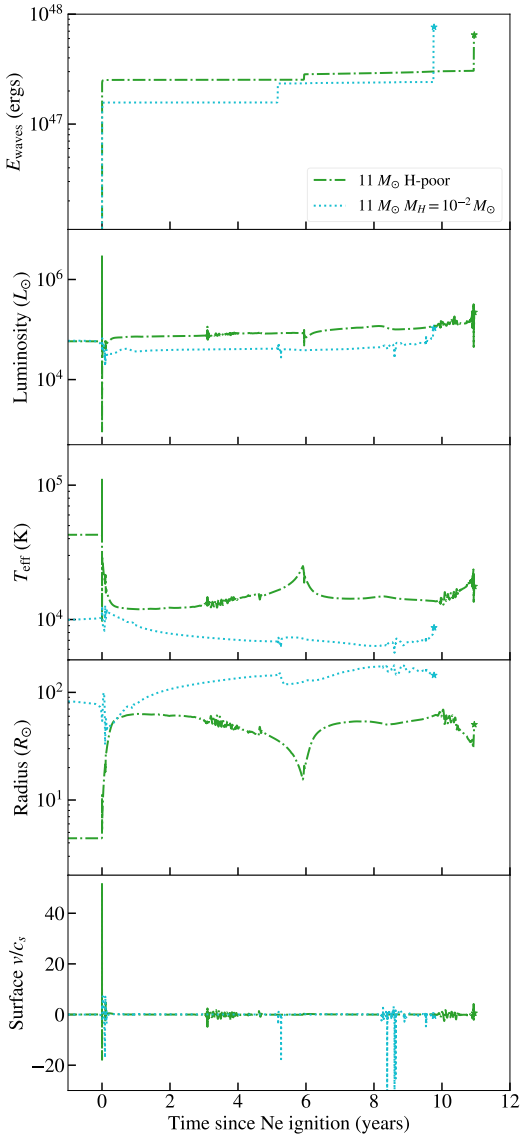

Figure 4.12: Same quantities as in Figure 4.6 are shown for the H-poor $M_{\rm ZAMS}$ = 11 $M_\odot$ model and a $M_{\rm ZAMS}$ = 11 $M_\odot$ stripped star model with $M_H = 10^{-2}$ $M_\odot$. The star symbol at the end of each curve indicates that both models reach core collapse.

to be emitted in optical bands rather than the UV. Like its brightness, the color of our $M_{\rm ZAMS} = 11\,M_\odot$ H-poor model varies over the last few years of its lifetime. The top panel of Figure 4.11 shows the evolution of some color indices for this star, again in AB mags. Before Ne ignition the star is brightest in UV, but due to wave heating the star reddens (but remains fairly blue) with F438W−F555W rising to near zero.

A few potential type Ib/c supernova progenitors have been observed and are indeed bluer than type II SN progenitors, but in some cases they are cooler or more extended than a typical massive helium star (Cao et al., 2013; Xiang et al., 2019; Kilpatrick et al., 2021). Among our stripped-star models, which represent type Ib SN progenitors, certain periods of evolution could reproduce these characteristics. For example, Eldridge et al. (2015) find that the progenitor candidate of iPTF13bvn has brightness between $\rm M_{F435W} = -6.15$ to -6.67 mag, $\rm M_{F555W} = -6.1$ to -6.49 mag, and $\rm M_{F814W} = -5.95$ to -6.13 mag. Our $M_{\rm ZAMS} = 11\,M_\odot$ H-poor model can match these ranges at around 6 months–5 years after Ne ignition.

The same $M_{\rm ZAMS} = 11\,M_\odot$ H-poor model can match the brightness of $\rm M_{F555W} \gtrsim -5.5$ mag observed by Kilpatrick et al. (2021) for the progenitor of SN2019yvr during most of the 10 years after Ne ignition. However, Kilpatrick et al., 2021 finds the potential progenitor to be much cooler than what our hydrogen-poor models reach, deriving $T_{\rm eff} = 6800^{+400}_{-200}$ K from models which account for both host and Milky Way extinction. They also report observations of $\rm M_{F555W} - M_{F814W} = 1.065 \pm 0.045$ mag, but this accounts only for Milky Way extinction and not yet host extinction. Nevertheless, based on these values, our $M_{\rm ZAMS} = 11\,M_\odot$ H-poor model would not be able to explain the SN2019yvr progenitor, as it only attains $\rm M_{F555W} - M_{F814W} \sim -0.5$ mag. Sun et al. (2022) find that if the source in Kilpatrick et al. (2021) is a binary system, then the progenitor of SN2019yvr could have $\log(T_{\rm eff}/K) = 4.03$ and $R/R_\odot = 57$ with likely initial mass $\sim 11\,M_\odot$. Our $M_{\rm ZAMS} = 11\,M_\odot$ stripped star model matches these observational constraints fairly well for the last 10 years of its life. Yet in both cases, the small amount of progenitor variability over ∼100 days of HST observations (Kilpatrick et al., 2021) may disfavor the wave-heated progenitor interpretation.

A stripped star model with a very small amount of hydrogen remaining in the envelope might explain cooler progenitors, as even a hundredth of a solar mass of hydrogen in the envelope causes the star to expand more and reach lower temperatures (Laplace et al., 2020). In our fiducial stripped star models, we strip the star of its envelope so that a negligible amount of hydrogen remains in the enve-

lope ($M_H \lesssim 10^{-3}\,M_\odot$) from carbon burning onward. In Figure 4.12, we compare our fiducial $M_{\rm ZAMS} = 11\,M_\odot$ H-poor model with an $M_{\rm ZAMS} = 11\,M_\odot$ stripped star model with $M_H = 10^{-2}\,M_\odot$ of hydrogen in the envelope from carbon burning onward, evolving the hydrodynamic response to wave heating as in the rest of our models. Even before wave heating begins, the $M_{\rm ZAMS} = 11\,M_\odot$ stripped star with $M_H = 10^{-2}\,M_\odot$ expands to $\sim 80\,R_\odot$ just before Ne burning. However, its luminosity just before Ne burning matches that of the H-poor model, and accordingly is a factor of four times cooler before Ne burning. This star would also remain at the point labeled "Pre-Ne Ignition" on the cyan curve in Figure 4.9 until core collapse in the absence of wave heating.

The wave heating history of the two models, shown in the top panel of Figure 4.12, is similar, but the model with $M_H = 10^{-2}\,M_\odot$ cools and expands in response to wave heating from Ne burning so that it is slightly less luminous than the H-poor model until core collapse (Figure 4.9). Since the $M_H = 10^{-2}\,M_\odot$ model expands to more than $100\,R_\odot$, its photospheric cools to the range $T_{\rm eff} = 6800^{+400}_{-200}$ K derived by Kilpatrick et al. (2021) for the progenitor of SN2019yvr. Consequently, the model with $M_H = 10^{-2}\,M_\odot$ is redder than the fiducial model (Figures 4.10 and 4.11), though it can also explain the color of iPTF13bvn's progenitor estimated in Eldridge et al. (2015). The model with more hydrogen exemplifies the varied evolution that can ensue depending on the residual hydrogen content of the stripped progenitor, which depends sensitively on the binary and wind mass loss that created the SN progenitor.

Related mass loss mechanisms

An interesting aspect of the stripped star models is their expansion from a few $R_\odot$ to tens of $R_\odot$. As stripped stars are likely to be in a binary system, this substantial, fast expansion may instigate binary mass transfer. The resulting rapid mass transfer could drive more mass loss from the system, or it could lead to unstable mass transfer that results in a common-envelope event or stellar merger (see also Mcley and Soker 2014). Since the mass loss is triggered in the final years before core-collapse, the ejected mass would still be near the progenitor at the time of core-collapse. Hence, this wave-induced binary interaction is a potential channel for generating larger CSM masses that should be explored in future work.

In our 10 and $10.5\,M_\odot$ models, we investigated only the initial Ne ignition and the progress of the ensuing off-center flame for 6–8 years after Ne ignition, which

encapsulated the majority of wave heating due to Ne burning. Yet this mass range may exhibit interesting behavior beyond this period of its evolution, as degenerate silicon ignition is highly energetic. On the one hand, this silicon burning could excite waves with very high wave power which have greater potential to eject mass. On the other hand, Woosley and Heger (2015) have found that silicon deflagration can occur in stars of this mass range, in which the silicon flash is violent enough to drive a shock and eject mass. Though it is computationally expensive to simulate late-stage nuclear burning this mass range, the period of Si burning should be studied in more detail as a possible mechanism for driving mass loss in these stars.

Time dependent convection

In our supergiant models, the internal luminosity can suddenly spike by a few orders of magnitude at the base of the convective envelope due to wave heating in this region. This manifests in the bottom panel of Figure 4.4, where $t_{\rm therm}$ dips at a mass coordinate of 3.5 $M_{\odot}$–which is due to an associated jump in the luminosity of the model at that location. This is caused by a sudden increase in the convective luminosity on a time scale comparable to the convective turnover time scale, which may not be physical, and calls for a time-dependent treatment of convection. In the results presented in this work, we have tried to partially mitigate unphysically large convective accelerations by using the MESA option `mlt_accel_g_theta = 1` in our supergiant models, which limits convective acceleration to the local gravitational acceleration. However, a more rigorous treatment of time-dependent convection (TDC) could further limit convective acceleration. This will affect whether wave heat is transported outward by convection, or whether it can be used to hydrodynamically drive a pressure pulse through the star.

To try to understand the range of possibilities, we investigated the efficacy of more sophisticated schemes to limit convective acceleration and deceleration. Following Renzo et al. (2020), we tried limiting convective acceleration based on the methods of Wood (1974). This method failed to create a physical model as spurious drops in luminosity at the surface of the convective envelope occurred. We also attempted the second treatment of TDC in Renzo et al. (2020), in which they use MESA v11123 to solve for convective velocity using their Equation 2 instead of using MLT. Unfortunately, a model using this method was unable to evolve through the extremely energetic degenerate Ne ignition.

Finally, we tested the response of a supergiant star's convective envelope to added

heat at the base of the envelope using an implementation of TDC that is available in a recent development version of MESA. A model using this TDC treatment exhibits almost identical behavior in the convective envelope to that of the models presented here, but with more numerical difficulties that make it difficult to apply to many models or to run them until core-collapse. Consequently, we choose to present our models that limit convective acceleration by `mlt_accel_g_theta = 1` and successfully run to core collapse, with the understanding that the convective behavior appears similar with more sophisticated convective acceleration schemes. However, from preliminary tests, the surface properties of the TDC model differed slightly from the results presented here. Moreover, it is possible that TDC could affect the progression of core convection at Ne ignition, which has implications for the wave heating results. We therefore emphasize the need for further work on how TDC affects the evolution of massive stars.

4.6 Conclusion

We have modeled the effect of wave heating in red supergiant and stripped-star SN progenitors with ZAMS masses between 10–13 $M_\odot$ using one-dimensional hydrodynamical simulations in MESA. In our models, we implement the improved wave heating physics of Wu and Fuller (2021) as we evolve to core collapse for $M_{\rm ZAMS} > 11\,M_\odot$, replicating the wave energy results of that work. We additionally study models with $M_{\rm ZAMS} \lesssim 10.5\,M_\odot$ which experience off-center ignition of Ne burning and are evolved to a few years after Ne ignition. These transmit much less wave heat than the centrally burning models because the wave power is carried primarily by $\ell \gtrsim 3$ waves that are mostly damped in the core.

The most energetic model in this study is the $M_{\rm ZAMS} = 11\,M_\odot$ model, which transmits $\sim 10^{47}$ erg of wave energy to its envelope around 10 years before core collapse in a burst of vigorous wave heating during central Ne burning. In our other models, waves are able to carry much less energy to the envelope. The wave energy in all of our supergiant and stripped star models is deposited just outside the core where the binding energy of overlying material is still high, and no mass loss is hydrodynamically driven by wave heating in any model. As a result, we do not predict that any of our models can produce significant CSM masses through wave heating alone.

As wave heat is deposited at the base of the hydrogen envelope in our supergiant models, their photospheric properties respond to wave heating with only small

oscillations in the final years before core-collapse. In our stripped star models, where wave heat is deposited much closer to the surface of the star, wave heating causes significant photospheric cooling and radial expansion in which $T_{\rm eff}$ decreases by a factor of a few and R increases by up to a factor of 10. Wave heating causes the brightness of the hydrogen-poor SN progenitors to increase by up to 3 mags in visual bands in the final ten years of evolution. Furthermore, these Ib/c progenitors appear redder in visual bands than predicted by models without wave heating. Our hydrogen-poor wave heated models are approximately consistent with the colors and absolute magnitudes of the progenitors of type Ib SNe iPTF13bvn and SN2019yvr, but low-mass models with a small amount of hydrogen ($\sim 10^{-2}\,M_\odot$, with or without wave heating) could also be consistent with those progenitor observations.

The large expansion of our hydrogen-poor models could also initiate interaction with a close binary companion, which could drive intense pre-supernova mass loss. Future work should study whether this channel is promising for producing more massive CSM. In addition, subsequent work should simulate the mass range $\sim$ 8–10 $M_\odot$ beyond the propagation of the off-center Ne burning flame and through degenerate silicon ignition, which should be energetic enough to either directly drive a shock (Woosley and Heger, 2015) or excite intense wave heating. Future investigations that are able to model this late-stage nuclear burning will be able to predict whether these stars can eject mass is the final months of their lives.

Acknowledgments

We thank Adam Jermyn for supplying the time-dependent convection modules from a MESA development version, and Charlie Kilpatrick for help with HST filter functions. This work was partially supported by NASA grants HSTAR-15021.001-A and 80NSSC18K1017. J.F. acknowledges support from an Innovator Grant from The Rose Hills Foundation, and the Sloan Foundation through grant FG2018-10515. This material is based upon work supported by the National Science Foundation Graduate Research Fellowship under Grant No. DGE-1745301.

4.7 Appendix: Dissipation in flows

In the presence of inward or outward flows with speed v_r, the wave damping length changes. The quantity of interest in our calculations is the wave heating rate per unit mass,

$$\epsilon = \frac{dL_{\rm heat,co}}{dm} \equiv \frac{L_{\rm ac}}{M_{\rm damp}}\,. \tag{4.25}$$

Here, $L_{\rm heat,co} = L_{\rm ac}/(1 + v_r/c_s)$ is the wave energy flux measured in the comoving frame, while $L_{\rm ac}$ is the wave action that is conserved (in the absence of damping) in the inertial frame. The notation in Fuller and Ro (2018) wrote $L_{\rm heat,co}$ as $L_{\rm wave}$. Note that the relevant energy flux available to dissipate as heat, $L_{\rm heat,co}$, is the wave flux in the co-moving frame, not the wave action $L_{\rm ac}$. However, the quantity $L_{\rm ac}$ is conserved in the absence of damping, so it is this quantity that is tracked in our code and effectively equal to $L_{{\rm heat},\ell}$ for each wave, and which is used to define the damping mass in Equation 4.25.

The wave damping rate in the comoving frame is (equation 17 of Fuller and Ro 2018)

$$\frac{dL_{\rm heat,co}}{dm} = \frac{\gamma+1}{3\pi}\sigma c_s^2 \left(\frac{L_{\rm heat,co}}{L_{\rm max}}\right)^{3/2}, \tag{4.26}$$

where σ is the wave frequency measured in the comoving frame. This is related to the wave frequency in the inertial frame (which is conserved) by $\sigma = \omega/(1+v_r/c_s)$. Substituting this and $L_{\rm heat,co} = L_{\rm ac}/(1 + v_r/c_s)$ into Equation 4.26 yields

$$\frac{dL_{\rm heat,co}}{dm} = \frac{\gamma+1}{3\pi}\omega c_s^2 \left(\frac{L_{\rm ac}}{L_{\rm max}}\right)^{3/2} (1 + v_r/c_s)^{-5/2}. \tag{4.27}$$

Finally, substituting this into Equation 4.25 yields the damping mass of Equation 4.17.

References

Barker, A. J. and G. I. Ogilvie (June 2010). "On internal wave breaking and tidal dissipation near the centre of a solar-type star". In: *MNRAS* 404.4, pp. 1849–1868. DOI: 10.1111/j.1365-2966.2010.16400.x.

Bruch, R. J. et al. (May 2021). "A Large Fraction of Hydrogen-rich Supernova Progenitors Experience Elevated Mass Loss Shortly Prior to Explosion". In: *ApJ* 912.1, p. 46. DOI: 10.3847/1538-4357/abef05.

Cao, Y. et al. (Sept. 2013). "Discovery, Progenitor and Early Evolution of a Stripped Envelope Supernova iPTF13bvn". In: *ApJL* 775.1, p. L7. DOI: 10.1088/2041-8205/775/1/L7.

Chen, T. .-. et al. (Nov. 2018). "SN 2017ens: The Metamorphosis of a Luminous Broadlined Type Ic Supernova into an SN IIn". In: *ApJL* 867.2, p. L31. DOI: 10.3847/2041-8213/aaeb2e.

Clark, P. et al. (Feb. 2020). "LSQ13ddu: a rapidly evolving stripped-envelope supernova with early circumstellar interaction signatures". In: *MNRAS* 492.2, pp. 2208–2228. DOI: 10.1093/mnras/stz3598.

Dessart, L., D. J. Hillier, and E. Audit (Sept. 2017). "Explosion of red-supergiant stars: Influence of the atmospheric structure on shock breakout and early-time supernova radiation". In: *A&A* 605, A83. DOI: 10.1051/0004-6361/201730942.

Eldridge, J. J. et al. (Jan. 2015). "Possible binary progenitors for the Type Ib supernova iPTF13bvn". In: *MNRAS* 446.3, pp. 2689–2695. DOI: 10.1093/mnras/stu2197.

Fuller, J. (Sept. 2017). "Pre-supernova outbursts via wave heating in massive stars - I. Red supergiants". In: *MNRAS* 470.2, pp. 1642–1656. DOI: 10.1093/mnras/stx1314.

Fuller, J. and S. Ro (May 2018). "Pre-supernova outbursts via wave heating in massive stars - II. Hydrogen-poor stars". In: *MNRAS* 476.2, pp. 1853–1868. DOI: 10.1093/mnras/sty369.

Gangopadhyay, A. et al. (Feb. 2020). "Flash Ionization Signatures in the Type Ibn Supernova SN 2019uo". In: *ApJ* 889.2, p. 170. DOI: 10.3847/1538-4357/ab6328.

Goldreich, P. and P. Kumar (Nov. 1990). "Wave Generation by Turbulent Convection". In: *ApJ* 363, p. 694. DOI: 10.1086/169376.

Hillier, D. J. and L. Dessart (Nov. 2019). "Photometric and spectroscopic diversity of Type II supernovae". In: *A&A* 631, A8. DOI: 10.1051/0004-6361/201935100.

Ho, A. Y. Q. et al. (Dec. 2019). "Evidence for Late-stage Eruptive Mass Loss in the Progenitor to SN2018gep, a Broad-lined Ic Supernova: Pre-explosion Emission and a Rapidly Rising Luminous Transient". In: *ApJ* 887.2, p. 169. DOI: 10.3847/1538-4357/ab55ec.

Johnson, S. A., C. S. Kochanek, and S. M. Adams (Dec. 2017). "On the progenitor of the Type Ibc supernova 2012fh". In: *MNRAS* 472.3, pp. 3115–3119. DOI: 10.1093/mnras/stx2170.

Johnson, S. A., C. S. Kochanek, and S. M. Adams (Oct. 2018). "The quiescent progenitors of four Type II-P/L supernovae". In: *MNRAS* 480.2, pp. 1696–1704. DOI: 10.1093/mnras/sty1966.

Kilpatrick, C. D. et al. (June 2021). "A cool and inflated progenitor candidate for the Type Ib supernova 2019yvr at 2.6 yr before explosion". In: *MNRAS* 504.2, pp. 2073–2093. DOI: 10.1093/mnras/stab838.

Kochanek, C. S. et al. (May 2017). "Supernova progenitors, their variability and the Type IIP Supernova ASASSN-16fq in M66". In: *MNRAS* 467.3, pp. 3347–3360. DOI: 10.1093/mnras/stx291.

Kuncarayakti, H. et al. (Feb. 2018). "SN 2017dio: A Type-Ic Supernova Exploding in a Hydrogen-rich Circumstellar Medium". In: *ApJL* 854.1, p. L14. DOI: 10.3847/2041-8213/aaaa1a.

Laplace, E. et al. (May 2020). “The expansion of stripped-envelope stars: Consequences for supernovae and gravitational-wave progenitors”. In: *A&A* 637, A6. DOI: 10.1051/0004-6361/201937300.

Lecoanet, D. and E. Quataert (Apr. 2013). “Internal gravity wave excitation by turbulent convection”. In: *MNRAS* 430.3, pp. 2363–2376. DOI: 10.1093/mnras/stt055.

Leung, S.-C., S. Wu, and J. Fuller (Oct. 2021). “Wave-driven mass loss of stripped envelope massive stars: progenitor-dependence, mass ejection, and supernovae”. In: *arXiv e-prints*, arXiv:2110.01565.

Lunnan, R. et al. (Sept. 2018). “A UV resonance line echo from a shell around a hydrogen-poor superluminous supernova”. In: *Nature Astronomy* 2, pp. 887–895. DOI: 10.1038/s41550-018-0568-z.

Mauerhan, J. C. et al. (Aug. 2018). “Stripped-envelope supernova SN 2004dk is now interacting with hydrogen-rich circumstellar material”. In: *MNRAS* 478.4, pp. 5050–5055. DOI: 10.1093/mnras/sty1307.

Mcley, L. and N. Soker (Dec. 2014). “Wave-driven stellar expansion and binary interaction in pre-supernova outbursts”. In: *MNRAS* 445.3, pp. 2492–2499. DOI: 10.1093/mnras/stu1952.

Nugis, T. and H. J. G. L. M. Lamers (Aug. 2000). “Mass-loss rates of Wolf-Rayet stars as a function of stellar parameters”. In: *A&A* 360, pp. 227–244.

Ofek, E. O. et al. (July 2014). “Precursors Prior to Type IIn Supernova Explosions are Common: Precursor Rates, Properties, and Correlations”. In: *ApJ* 789.2, p. 104. DOI: 10.1088/0004-637X/789/2/104.

Paxton, B. et al. (Jan. 2011). “Modules for Experiments in Stellar Astrophysics (MESA)”. In: *ApJS* 192, p. 3. DOI: 10.1088/0067-0049/192/1/3.

Paxton, B. et al. (Sept. 2013). “Modules for Experiments in Stellar Astrophysics (MESA): Planets, Oscillations, Rotation, and Massive Stars”. In: *ApJS* 208.1, p. 4. DOI: 10.1088/0067-0049/208/1/4.

Paxton, B. et al. (Sept. 2015). “Modules for Experiments in Stellar Astrophysics (MESA): Binaries, Pulsations, and Explosions”. In: *ApJS* 220.1, p. 15. DOI: 10.1088/0067-0049/220/1/15.

Paxton, B. et al. (Feb. 2018). “Modules for Experiments in Stellar Astrophysics (MESA): Convective Boundaries, Element Diffusion, and Massive Star Explosions”. In: *ApJS* 234.2, p. 34. DOI: 10.3847/1538-4365/aaa5a8.

Paxton, B. et al. (July 2019). “Modules for Experiments in Stellar Astrophysics (MESA): Pulsating Variable Stars, Rotation, Convective Boundaries, and Energy Conservation”. In: *ApJS* 243.1, p. 10. DOI: 10.3847/1538-4365/ab2241.

Pooley, D. et al. (Oct. 2019). “Interaction of SN Ib 2004dk with a Previously Expelled Envelope”. In: *ApJ* 883.2, p. 120. DOI: 10.3847/1538-4357/ab3e36.

Quataert, E. and J. Shiode (June 2012). "Wave-driven mass loss in the last year of stellar evolution: setting the stage for the most luminous core-collapse supernovae". In: *MNRAS* 423.1, pp. L92–L96. DOI: 10.1111/j.1745-3933.2012.01264.x.

Renzo, M. et al. (Apr. 2020). "Sensitivity of the lower edge of the pair-instability black hole mass gap to the treatment of time-dependent convection". In: *MNRAS* 493.3, pp. 4333–4341. DOI: 10.1093/mnras/staa549.

Shiode, J. H. and E. Quataert (Jan. 2014). "Setting the Stage for Circumstellar Interaction in Core-Collapse Supernovae. II. Wave-driven Mass Loss in Supernova Progenitors". In: *ApJ* 780.1, p. 96. DOI: 10.1088/0004-637X/780/1/96.

Shiode, J. H. et al. (Apr. 2013). "The observational signatures of convectively excited gravity modes in main-sequence stars". In: *MNRAS* 430.3, pp. 1736–1745. DOI: 10.1093/mnras/sts719.

Sun, N.-C. et al. (Mar. 2022). "An environmental analysis of the Type Ib SN 2019yvr and the possible presence of an inflated binary companion". In: *MNRAS* 510.3, pp. 3701–3715. DOI: 10.1093/mnras/stab3768.

Taddia, F. et al. (June 2020). "The Carnegie Supernova Project II. The shock wave revealed through the fog: The strongly interacting Type IIn SN 2013L". In: *A&A* 638, A92. DOI: 10.1051/0004-6361/201936654.

Wood, P. R. (June 1974). "Models of Asymptotic-Giant Stars". In: *ApJ* 190, pp. 609–630. DOI: 10.1086/152919.

Woosley, S. E. and A. Heger (Sept. 2015). "The Remarkable Deaths of 9-11 Solar Mass Stars". In: *ApJ* 810.1, p. 34. DOI: 10.1088/0004-637X/810/1/34.

Wu, S. C. and J. Fuller (Jan. 2021). "A Diversity of Wave-driven Presupernova Outbursts". In: *The Astrophysical Journal* 906.1, p. 3. DOI: 10.3847/1538-4357/abc87c.

Xiang, D. et al. (Feb. 2019). "Observations of SN 2017ein Reveal Shock Breakout Emission and a Massive Progenitor Star for a Type Ic Supernova". In: *ApJ* 871.2, p. 176. DOI: 10.3847/1538-4357/aaf8b0.

Yao, Y. et al. (Sept. 2020). "SN2019dge: A Helium-rich Ultra-stripped Envelope Supernova". In: *ApJ* 900.1, p. 46. DOI: 10.3847/1538-4357/abaa3d.

Yaron, O. et al. (Feb. 2017). "Confined dense circumstellar material surrounding a regular type II supernova". In: *Nature Physics* 13.5, pp. 510–517. DOI: 10.1038/nphys4025.

Zhang, J. et al. (Oct. 2020). "SN 2018zd: an unusual stellar explosion as part of the diverse Type II Supernova landscape". In: *MNRAS* 498.1, pp. 84–100. DOI: 10.1093/mnras/staa2273.

Chapter 5

EXTREME MASS LOSS IN LOW-MASS TYPE IB/C SUPERNOVA PROGENITORS

Wu, S. C. and J. Fuller (Nov. 2022). "Extreme Mass Loss in Low-mass Type Ib/c Supernova Progenitors". In: *The Astrophysical Journal, Letters* 940.1, p. L27. DOI: 10.3847/2041-8213/ac9b3d.

5.1 Abstract

Many core collapse supernovae (SNe) with hydrogen-poor and low-mass ejecta, such as ultra-stripped SNe and type Ibn SNe, are observed to interact with dense circumstellar material (CSM). These events likely arise from the core-collapse of helium stars which have been heavily stripped by a binary companion and ejected significant mass during the last weeks to years of their lives. In helium star models run to days before core-collapse, we identify a range of helium core masses $\approx$ 2.5–3 $M_\odot$ whose envelopes expand substantially due to helium shell burning while the core undergoes neon and oxygen burning. When modeled in binary systems, the rapid expansion of these helium stars induces extremely high rates of late-stage mass transfer ($\dot{M} \gtrsim 10^{-2}\, M_\odot/\mathrm{yr}$) beginning weeks to decades before core-collapse. We consider two scenarios for producing CSM in these systems: either mass transfer remains stable and mass loss is driven from the system in the vicinity of the accreting companion, or mass transfer becomes unstable and causes a common-envelope event (CEE) through which the helium envelope is unbound. The ensuing CSM properties are consistent with the CSM masses ($\sim 10^{-2} - 1\, M_\odot$) and radii ($\sim 10^{13} - 10^{16}$ cm) inferred for ultra-stripped SNe and several type Ibn SNe. Furthermore, systems that undergo a CEE could produce short-period NS binaries that merge in less than 100 Myr.

5.2 Introduction

Many types of core-collapse supernovae (SNe) show signs of interaction with dense circumstellar material (CSM), likely created by extreme mass loss at the end of the SN progenitor's life. Type Ibn SNe are characterized by interaction with hydrogen-poor and helium-rich CSM, which produces spectra dominated by narrow helium (He) lines and powers early-time light curves that often rise and decay quickly.

Typical rise times of $\lesssim$ 15 days and peak magnitudes of $M_R \sim -19$ to -20 mag in these events indicate ejecta masses $M_{\rm ej}$ = 1–5 $M_\odot$ and ^{56}Ni masses $M_{\rm Ni} \lesssim 0.1\,M_\odot$ (Gangopadhyay et al., 2022; Maeda and Moriya, 2022; Ho et al., 2021). These SNe are thought to originate from massive stars that have previously lost their hydrogen envelopes, then expelled helium-rich CSM just before core-collapse.

A few events have been discovered with even lower $M_{\rm ej}$ and $M_{\rm Ni}$, classified as ultra-stripped SNe (USSNe). For example, the short decline time of type Ic SN iPTF 14gqr indicates a small ejecta mass of $M_{\rm ej} \sim 0.2\,M_\odot$ (De et al., 2018), and consequently a low pre-collapse mass of $M_{\rm He} \sim 1.6\,M_\odot$ (assuming a baryonic NS mass of $M_{\rm NS} = 1.4\,M_\odot$). The type Ib SN 2019dge has $M_{\rm ej} = 0.4\,M_\odot$, implying pre-collapse mass $M_{\rm He} \sim 1.8\,M_\odot$ (Yao et al., 2020). Bright, rapidly rising early-time light curves and flash-ionized He emission in early spectra indicate extended CSM in SN iPTF 14gqr and SN 2019dge. Another type of interacting SNe, type Icn SNe, exhibit narrow emission lines from recombination of ionized carbon and oxygen instead of He. With comparable peak luminosities to type Ibn SNe but low $M_{\rm Ni}$ and $M_{\rm ej}$, type Icn SNe have been proposed to arise from similar channels to USSNe (Pellegrino et al., 2022b).

Highly stripped helium stars are the probable progenitors of USSNe. Stars that have lost their hydrogen envelopes after hydrogen burning through case B mass transfer form stripped stars from their He cores. Stripped stars with $M_{\rm He} \lesssim 4\,M_\odot$ expand again and initiate so-called case BB mass transfer in systems with final separations of less than a few 100 $R_\odot$ after case B mass transfer (Habets, 1986b; Habets, 1986a), thereby losing a significant amount of their He envelope as well. At core-collapse, their low pre-collapse masses can explain the requisite $M_{\rm ej}$ of USSNe (Tauris et al., 2013; Tauris, Langer, and Podsiadlowski, 2015). When the USSNe is formed from the initially less massive star in the binary, such systems are likely the most common progenitors of compact NS binaries (Dewi and Pols, 2003; Tauris et al., 2013; Tauris, Langer, and Podsiadlowski, 2015).

Previous work (Tauris et al., 2013; Tauris, Langer, and Podsiadlowski, 2015; Yoon, Woosley, and Langer, 2010; Zapartas et al., 2017; Laplace et al., 2020) has modeled case BB mass transfer (MT) in detail to make predictions for mass loss and the final fate of the progenitor. Thus far, most stellar models do not predict large amounts of CSM near the progenitor system as detected in several USSNe and type Ibn SNe. Yet the vast majority of stripped progenitor models omit the evolution onward from oxygen/neon (O/Ne) burning, and they miss crucial physics that transpires during

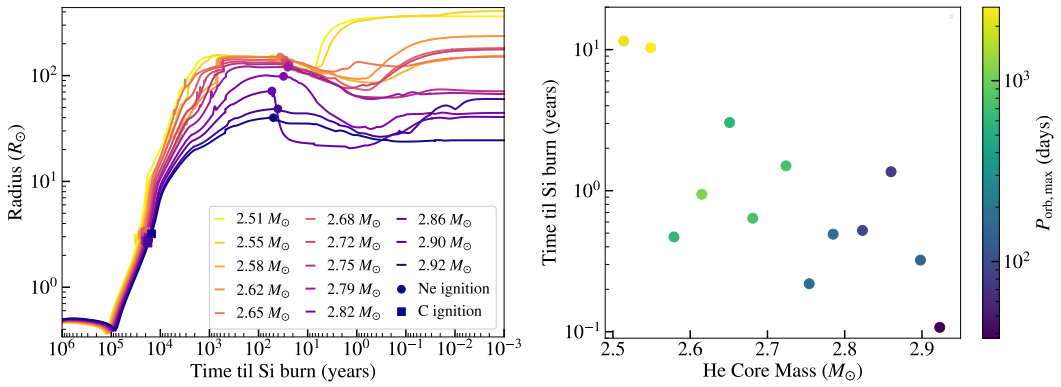

Figure 5.1: **Left**: Evolution of the radius of single stripped stars as a function of time until Si burning. The legend labels the initial He core mass of each stripped star. Each star expands after He burning and throughout C burning, then contracts and re-expands during O/Ne burning. **Right**: Time before Si burning of the stripped stars' second expansion. Points are colored by the maximum orbital period at which the star will fill its Roche lobe in a binary with a 1.4 $M_\odot$ companion star.

these final years of the star's lifetime that may explain such SN observations. We find that helium stars of masses $\approx 2.5 - 3\,M_\odot$ rapidly re-expand while the core burns O/Ne, which initiates high rates of late-stage MT weeks to decades before core-collapse that may produce CSM.

5.3 Methods

We use MESA (version r15140, Paxton et al., 2011; Paxton et al., 2013; Paxton et al., 2015; Paxton et al., 2018; Paxton et al., 2019) to model 1d stellar evolution up to silicon (Si) burning of single, stripped stars at $Z = 0.02$ with $2.5\,M_\odot \lesssim M_{\rm He} \lesssim 3\,M_\odot$ [1]. The timing of removing surface hydrogen, the amount of hydrogen remaining, and the inclusion of stellar winds each affect how initial mass $M_{\rm ZAMS}$ maps to He core mass $M_{\rm He}$ after core He burning. In this work, we remove the entire hydrogen envelope of stars with initial masses $M_{\rm ZAMS} = 13.8$–$15\,M_\odot$ once core hydrogen burning ends and evolve without wind mass loss. Ultimately, the relation between initial and helium star mass is not central to the result, and we find that the behavior of our models depends primarily on the He core mass after core He burning. Throughout, we label our models by these initial He core masses $M_{\rm He}$.

We also model the stripped stars in binaries at a range of orbital periods from 1 to 100 days to estimate the ensuing mass transfer rates. For our binary models, we consider the fiducial scenario where the stripped star formed from the initially

[1] The data is available on Zenodo at 10.5281/zenodo.7106182.

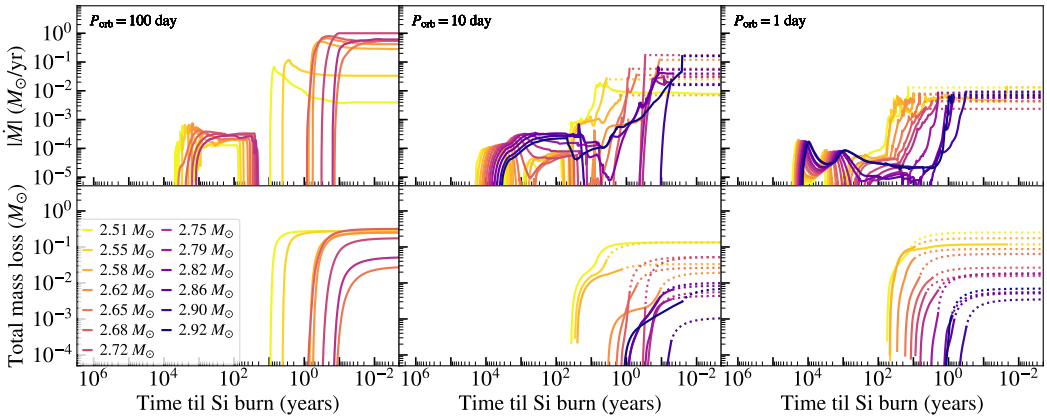

Figure 5.2: The mass loss rates and accumulated mass loss of the helium star models, each of which is placed in a binary with a 1.4 $M_\odot$ compact companion at the initial orbital periods listed in the top panels. The legend indicates the initial mass of each helium star. For simulations that end before Si burning, we assume that $\dot{M}$ remains steady until Si burning and extrapolate the accumulated mass loss until Si burning, shown as dotted lines.

less massive star in the binary, so its companion is a $M_c = 1.4\,M_\odot$ neutron star, represented by a point mass. We use a modified version of the implicit MT scheme of Kolb and Ritter (1990) for Roche lobe overflow. Since this prescription assumes an ideal gas EOS, it underestimates mass loss rates for surface layers dominated by radiation pressure; to address this, we revise the scheme to compute the pressure from the stellar model (e.g., Marchant et al., 2021). We assume non-conservative mass transfer where the mass is removed from the system in the vicinity of the accretor as a fast wind. As we find that mass transfer rates during both case BB and late-stage mass loss are many orders of magnitude larger than the Eddington accretion limit of a NS ($\dot{M}_{\rm edd} \sim 4\times10^{-8}\,M_\odot\,{\rm yr}^{-1}$), we expect that nearly 100% of the mass is lost from the system (as in, e.g., Tauris, Langer, and Podsiadlowski 2015), though mass loss out the L2 and/or L3 points could modify the binary's angular momentum loss (see Section 5.5).

5.4 Results

Single star evolution

Stripped stars with initial masses $2.5\,M_\odot \lesssim M_{\rm He} \lesssim 3\,M_\odot$ expand during several phases of their evolution. In the left panel of Figure 5.1, the radii of the stripped stars increase by two orders of magnitude during C burning beginning $\sim 10^5$ years before Si burning, which in a binary system causes case BB MT. Notably, the stars

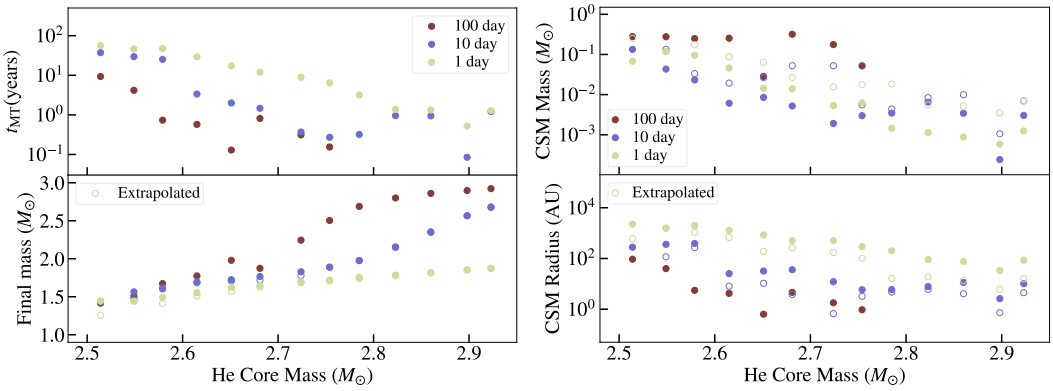

Figure 5.3: Properties of each binary system undergoing late-stage mass loss. Points are plotted as a function of the helium star's initial mass, and colors correspond to the initial orbital period given in the legend. Dots represent mass loss up to the end of the solid lines in Figure 5.2, and open circles include the extrapolated mass loss shown as dotted lines in Figure 5.2. **Top left**: Time before Si burning when late-stage MT ensues, $t_{\rm MT}$, as defined in Section 5.4. **Bottom left**: Final mass of each stripped star after case BB and late-stage MT. **Right**: Predicted mass (top) and radius (bottom) of CSM due to late-stage mass loss.

contract after C-shell burning (a few decades before Si burning) and expand by a factor of a few again during O/Ne burning, which can initiate late-stage MT.

The right panel of Figure 5.1 plots the time before Si burning when this late expansion occurs versus stripped star mass $M_{\rm He}$. For higher masses, expansion occurs months before Si burning during late O burning, but lower masses expand again a decade before Si burning. However, the expansion is driven not by core burning but rather by intense He burning at the base of the helium envelope. This behavior can be understood by the mirror principle (e.g., Kippenhahn, Weigert, and Weiss, 2012; Laplace et al., 2020), in which core contraction after certain burning phases (e.g., C-shell burning) causes the temperature of the He burning shell to increase. As the temperature-sensitive triple-alpha energy generation rate increases significantly, the envelope of the star expands in response to the intensified heating at its base.

From the maximum radius to which each stripped star expands, we estimate the maximum orbital period $P_{\rm orb}$ for the star to fill its Roche lobe during late-stage MT. For a companion mass of $M_{\rm c}$, the mass ratio is $q = M_{\rm c}/M_{\rm He}$. Then the ratio of Roche lobe radius $R_{\rm RL}$ to semi-major axis a is approximately (Eggleton, 1983)

$$\frac{R_{\rm RL}}{a} = 0.49\frac{q^{2/3}}{0.6q^{2/3} + \log(1+q^{1/3})}. \tag{5.1}$$

Setting each star's maximum radius during O/Ne burning to $R_{\rm RL}$ and applying Kepler's third law gives the maximum orbital period for Roche lobe overflow, $P_{\rm orb,max}$. In the right panel of Figure 5.1, points are shaded by the value of $P_{\rm orb,max}$, which tends to decrease with He mass. The stripped stars may initiate late-stage MT up to orbital periods of months to years.

Binary evolution

Figure 5.2 shows the mass transfer rates $\dot{M}$ and accumulated mass loss of our binary models at $P_{\rm orb}$ = 100, 10, and 1 day. Once the models achieve very high mass loss rates $\dot{M} \gtrsim 10^{-3}\,M_\odot$/yr, MESA systematically encounters numerical difficulties at the surface of the star, where mass layers are rapidly stripped. In models where MESA is unable to evolve the mass transfer up to Si burning, we estimate the time until Si burning by comparison with single-star models and also extrapolate further potential mass loss by assuming that $\dot{M}$ plateaus until Si burning. This approximates the behavior of models that do evolve to Si burning (e.g., $P_{\rm orb}$ = 100 day); in practice, the extrapolation may be a lower limit to the true mass loss since mass transfer rates are usually increasing sharply when models terminate. Binary models at larger $P_{\rm orb}$ begin late-stage MT later in the donor's lifetime, and the highest-mass models $M_{\rm He} \gtrsim 2.8\,M_\odot$ do not expand enough to fill their Roche lobes at $P_{\rm orb}$ = 100 day. At $P_{\rm orb}$ = 1 day, models do not fully detach from their Roche lobes after C burning, but late-stage MT clearly manifests as $\dot{M}$ increases by ∼2–3 orders of magnitude during O/Ne burning.

Typical mass loss rates are 10^{-3}–$10^{-1}\,M_\odot$/yr during late-stage MT. Though our binary models at $P_{\rm orb}$ = 100 day rise to $\dot{M} \sim 0.1$–$1\,M_\odot$/yr in the last weeks to months before Si burning, these highly uncertain values occur because the models greatly overfill their Roche lobes during these phases, causing the mass transfer scheme in MESA to break down. We define the time until Si burning when late-stage MT occurs, $t_{\rm MT}$, when $\dot{M} > 5 \times 10^{-4}\,M_\odot$/yr, significantly exceeding the case BB MT rate of $\sim 10^{-4}\,M_\odot$/yr. In the top left panel of Figure 5.3, $t_{\rm MT}$ is shown for each He star. The mass loss rate tends to rise months to years before Si burning for models of larger mass and longer $P_{\rm orb}$, but late-stage MT can occur years to decades before Si burning for lower mass and shorter $P_{\rm orb}$.

The bottom left panel of Figure 5.3 shows the final masses after both case BB and late-stage mass loss, which range between ~ 1.4–$2.9\,M_\odot$. The low pre-collapse masses imply small SN ejecta masses $\lesssim 1.5\,M_\odot$, assuming $M_{\rm NS} = 1.4\,M_\odot$. Com-

pared to similar models in Tauris, Langer, and Podsiadlowski, 2015, our mass transfer rates during C burning and final masses are consistent with their results. Following their argument that models with final CO core masses $\gtrsim 1.43\,M_\odot$ will reach iron core collapse, we expect that our lowest-mass models 2.5–2.55 $M_\odot$ may become electron-capture SNe, while the majority of our models $\gtrsim 2.6\,M_\odot$ will undergo core collapse. The final fate of our models corresponds to slightly different initial He core masses than in Tauris, Langer, and Podsiadlowski (2015), as our stellar evolution implementation produces slightly higher CO core masses for the same initial mass.

CSM properties

To estimate the properties of CSM ensuing from late-stage MT, we treat each donor's mass loss as ejected from the system in the vicinity of the accretor. Stable MT at these high rates may form an advection-dominated, geometrically thick accretion disk around the companion that can drive a large proportion of mass from the outer disk, lost through the L2 point (Lu et al., 2022; Pejcha, Metzger, and Tomida, 2016). Motivated by this scenario, we assume lost mass leaves with the orbital velocity at the L2 point. In reality, the ejection speed may vary due to initial conditions and torquing by the binary, and ejection velocities and CSM radii smaller by a factor of ∼3 may be more realistic (Hubová and Pejcha, 2019).

Shells of expelled material form at a distribution of radii around the system, so we perform a mass-weighted average of these radii to calculate the characteristic CSM radius. The integrated mass loss rate at core collapse equals the total CSM mass in each system. As shown in the right panel of Figure 5.3, we predict CSM masses ranging from $10^{-3}\,M_\odot$ for $\sim 2.9\,M_\odot$ progenitors up to $\sim 3\times10^{-1}\,M_\odot$ for ∼2.5–2.7 $M_\odot$ progenitors. As it originates from stripping of the He envelope, the CSM produced by our models is He-rich, with He mass fractions $\gtrsim 0.7$ for the majority of the CSM mass.

In our models, the orbital velocity at L2 increases from ∼ 100 km/s at $P_{\rm orb} \approx 100$ day to ∼ 500 km/s at $P_{\rm orb} \approx 1$ day. Mass ejected from the system at these velocities reaches radii of ∼ 1–10^4 AU. Lower mass and shorter $P_{\rm orb}$ models tend to produce CSM at larger radii, as late-stage MT begins earlier in the evolution and in the latter case is ejected with larger velocities.

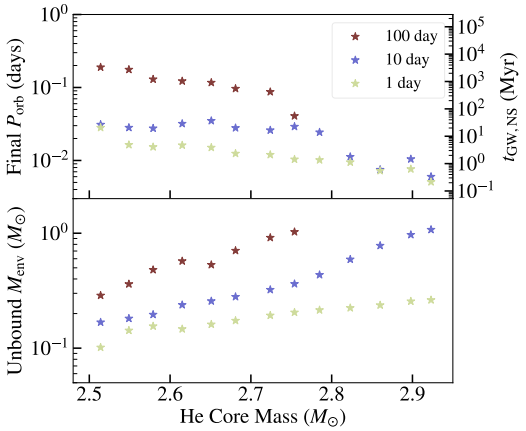

Figure 5.4: Properties of the binary systems after a common-envelope event (CEE), assuming unstable MT begins once $\dot{M} > 5\times10^{-4}\ M_\odot/\mathrm{yr}$ and that inspiral ends once the NS unbinds envelope down to the CO core. Points are plotted as in Figure 5.3 as a function of each stripped star's initial He core mass. **Top**: Values on the left axis show the final orbital period of each system after CEE. The right axis values are the gravitational wave merger timescales for a binary system consisting of two neutron stars orbiting at the periods of the left axis. **Bottom**: Envelope mass unbound by the CEE.

Common-envelope events

The sharply rising mass transfer rates in all our models may indicate the onset of unstable MT, leading to a common-envelope event (CEE). In this case, we would expect the companion to inspiral into the envelope of the ultra-stripped star, with total mass $M_{\rm s}$ at the onset of CEE. We predict the outcome by assuming that unstable MT ensues soon after $\dot{M}$ exceeds $5\times10^{-4}\ M_\odot/\mathrm{yr}$, and that the inspiral will terminate once the change in the orbital energy is sufficient to unbind the entire envelope of mass $M_{\rm s,env}$ exterior to the C/O core of mass $M_{\rm s,core}$. To quantify this, we use the α energy formalism:

$$E_{\rm bind} = \alpha \Delta E_{\rm orb} \tag{5.2}$$

$$= \alpha \left(-\frac{G M_{\rm s} M_{\rm c}}{2 a_{\rm i}} + \frac{G M_{\rm s,core} M_{\rm c}}{2 a_{\rm f}} \right) \tag{5.3}$$

where $E_{\rm bind} = \int_{\rm core}^{\rm surface} -\frac{Gm}{r} + \epsilon(m)\, dm$, where ϵ is the specific internal energy. Here, the CE efficiency α parameterizes the fraction of orbital energy used to eject the envelope, $M_{\rm c}$ is the companion mass, and $a_{\rm i}$ is the initial orbital separation, determined by Equation 5.1 with $R_{\rm RL}$ equal to the stellar radius at CE onset. We

solve for the final orbital separation a_f which satisfies thisequation for each binary model assuming $\alpha = 0.3$, consistent with observational constraints (Zorotovic et al., 2010; Zorotovic and Schreiber, 2022). Though defining the final mass after the CEE is uncertain, we find that our results are not sensitive to this choice; here, we set the final mass to be the CO core mass at the onset of CEE.

Figure 5.4 shows final orbital periods of our models after the CEE. In the vast majority of systems, the binary exits the CEE at orbital periods $\lesssim 4$ hours, which can merge within a Hubble time. This orbital separation is too small to admit a main sequence star, so unstable mass transfer with a main sequence companion will likely result in a stellar merger followed by an unusual supernova. White dwarf or neutron star companions, however, can likely eject the envelope before merging with the CO core. The gravitational wave orbital decay timescale for a binary of two neutron stars $M_{NS} = 1.4\,M_\odot$ at each orbital period, $t_{GW,NS}$, is shown for comparison on the right axis. Models with larger M_{He} and shorter initial P_{orb} can reach final P_{orb} of under thirty minutes, corresponding to $t_{GW,NS} \lesssim 10$ Myr.

The bottom panel of Figure 5.4 shows the mass of the unbound envelope due to the CEE, which increases with M_{He} from $\sim 10^{-1}\,M_\odot$ to $1\,M_\odot$ for more massive progenitors. These CSM masses typically exceed our estimates for the stable mass transfer scenario by a factor of ~10, though we reiterate that those values are likely to be lower limits in many cases. We estimate the CSM radii produced by a CEE by assuming the envelope is ejected with a terminal velocity equal to the star's pre-CE surface escape velocity (consistent with $\alpha \sim 1/3$).

Comparisons to USSNe and type Ibn/Icn SNe

Figure 5.5 compares CSM masses and radii inferred for several interacting SNe with our model predictions. We include our estimates for stable late-stage mass loss (Section 5.4) and from mass ejected due to a CEE (Section 5.4). In general, methods of observationally constraining the mass and radius of CSM are likely uncertain by a factor of a few (De et al., 2018; Chatzopoulos et al., 2013; Chatzopoulos, Wheeler, and Vinko, 2012), so we show inferred values with error bars of at least a factor of two in each direction.

In the vast majority of our models, the predicted CSM is H-poor and He-rich, so interaction with the CSM during a SN would likely produce spectra classified as type Ibn. Several type Ibn SNe are shown in Figure 5.5 as thin diamonds. SN 2006jc (Anupama et al., 2009) may be matched by a range of $P_{orb} = 1$ and 10

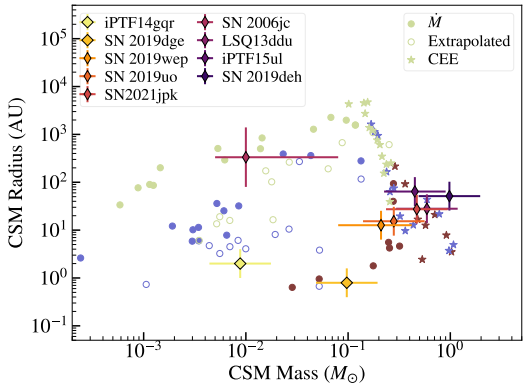

Figure 5.5: Dots and open circles are predicted mass versus radius of CSM due to late-stage mass loss (Figure 5.3, Section 5.4). Star symbols are predicted mass and radius of material unbound during CEE (Figure 5.4, Section 5.4). Colors indicate initial $P_{\rm orb}$ as in Figure 5.3. Points with error bars are estimated CSM properties of USSNe (square diamonds) and type Ibn SNe (thin diamonds). All are given error bars of at least a factor of two in each direction to account for systematic uncertainties in the modeling.

day models for late-stage MT, whereas CSM estimates for iPTF15ul, SN 2019wep, and SN 2019uo (Pellegrino et al., 2022a) fall within the late-stage MT estimates for initial $P_{\rm orb} = 100$ day. All type Ibn events shown, including SN 2019deh, SN 2021jpk, and LSQ13ddu (Pellegrino et al., 2022a; Clark et al., 2020), can be explained by CSM produced in a CEE in several $P_{\rm orb} = 1$, 10, and 100 day models.

Estimates from modeling shock-cooling emission of extended material around the progenitors in USSNe iPTF14gqr and SN 2019dge, shown as the blue and orange diamonds, are consistent only with our smallest CSM radii predictions. Our models for late-stage MT with initial $P_{\rm orb} = 10$ day and $M_{\rm He} = 2.6$–$2.9\,M_\odot$ can explain the envelope mass $M_e \approx 0.01\,M_\odot$ and radius $R_e \gtrsim 2$ AU derived for iPTF 14gqr (De et al., 2018). Similar-mass late-stage MT models with initial $P_{\rm orb} = 100$ day can explain observed material at ~ 1 AU for SN 2019dge (Yao et al., 2020).

In addition, outer CSM regions located beyond a few to tens of AU have been detected in iPTF14gqr and SN 2019dge. Estimates from He II line emission of the mass of helium in this outer CSM provide lower limits of $\gtrsim 3 \times 10^{-5}\,M_\odot$ for SN 2019dge and $\gtrsim 10^{-2}\,M_\odot$ for iPTF14gqr. CSM produced from late-stage mass transfer fits well with the properties of outer regions of CSM in both USSNe. In addition, our models routinely attain the inferred pre-supernova mass loss rates of $\gtrsim 10^{-2}\,M_\odot$/yr and $\gtrsim 10^{-4}\,M_\odot$/yr, respectively, for iPTF14gqr and SN 2019dge.

Interaction with CSM has been detected in several type Icn SNe (Pellegrino et al., 2022b; Gal-Yam et al., 2022). These events mainly show narrow C/O emission lines, though none are conclusively devoid of He, and the type Icn SN 2019jc in particular has an He II feature. With the exception of the values derived for SN 2019hgp by Gal-Yam et al. 2022, the type Icn SNe tend to produce more massive CSM than our models predict. Most importantly, these events likely require lower He mass fractions than ejected by our models (Dessart, John Hillier, and Kuncarayakti, 2022), which typically have $X_{\rm He} \sim 0.8$ and $X_{\rm CO} \sim 0.2$.

5.5 Discussion and conclusions

The fiducial scenario addressed by our binary models describes a He star, formed from the initially less massive star (the secondary) in a binary, with a NS companion evolved from the initially more massive star (the primary). However, primary stars within our modeled mass range will exhibit the same behavior. If the primary has a low-mass main sequence (MS) companion, case B MT is expected to be dynamically unstable leading to CEE. The low-mass MS star could survive the inspiral and exit CEE in a close orbit with the He star–these are likely the progenitors of low-mass X-ray binaries (e.g., Verbunt, 1993; Kalogera and Webbink, 1998). If the companion is massive, case B MT is likely stable and may widen the orbit, but for post-MT separations less than a few 100 $R_\odot$ the He star can still overfill its Roche lobe during late-stage expansion. Thus the late-stage mass transfer displayed by our stripped star models may affect the appearance of a type Ib/c SN coming from either primary or secondary stars with $M_{\rm He} \sim 2.5$–$3\ M_\odot$.

At the extreme mass transfer rates predicted, the dynamics of the ejected mass are uncertain. Since the donor may greatly overfill its Roche lobe, mass may also flow out of the donor's outer Lagrange point (L3 if the donor is more massive; Linial and Sari 2017; Marchant et al. 2021). Even if the companion is not a compact object, the high mass transfer rates, if stable, may form a geometrically thick accretion disk around the companion. The disk will be super-Eddington even at large radii, such that L2 mass loss is predicted (Lu et al., 2022). The ensuing circumbinary outflow may cause appreciable additional angular momentum loss given the larger lever arm of the L2 point. This effect may shrink the orbital separation more rapidly, increasing and potentially destabilizing the mass transfer rates. In preliminary tests, we have noticed a $\sim 20\%$ increase in the MT rate if we change the specific angular momentum of the mass lost to that of the L2 point.

However, the ejection velocities of ~ 200 km/s predicted in this framework tend to be lower than estimated from line widths in observed SNe. In the case of accretion onto a compact object, the disk around the accretor may launch a super-Eddington wind that sweeps up the slower outflow from the L2 point. It is also unclear how the ejected mass will be distributed. Though we report only a single CSM radius, the material will certainly cover a large radial extent and may not have a smooth or spherically symmetric profile.

If the mass transfer becomes dynamically unstable, the accretion disk scenario is superseded by a common-envelope event, as explored in Section 5.4. Our models with $P_{\rm orb} = 100$ day appear highly susceptible to CEE, as they reach very high mass transfer rates $\dot{M} \sim 1\,M_\odot/{\rm yr}$ which approach the dynamical regime of mass transfer. They also have fully convective envelopes at the onset of late stage MT and therefore are more inclined to lose MT stability. Once $P_{\rm orb}$ decreases to 1 day, models instead host only a very thin surface convective region. Hence, late-stage MT in binaries at long $P_{\rm orb}$ may result in CEE events that eject $\sim 1\,M_\odot$, while binaries at shorter $P_{\rm orb}$ may remain stable due to their mostly radiative envelopes. The former may account for many of the observed type Ibn SNe, while the latter may account for USSNe with He-rich CSM. Both scenarios may contribute to NS mergers, depending on the degree of orbital decay during CEE or late stage MT.

We roughly estimate the birth rate of progenitor systems that exhibit late-stage MT in order to compare with the rate of type Ibn SNe that they may produce. The volumetric rate of type Ib/c SNe is $\sim 2.5 \times 10^{-5}\,{\rm Mpc}^{-3}\,{\rm yr}^{-1}$ (Li et al., 2011; Frohmaier et al., 2021). Given that type Ib/c SNe are thought to arise from binaries with a stripped star component, the type Ib/c rate approximates the birth rate of such systems, regardless of whether the primary or secondary star produces the SN. Our He star models could produce late-stage MT as either the primary or secondary star, and they represent the low-mass subset of type Ib/c SN progenitors. Binaries producing late-stage MT include at least one star with $M_{\rm ZAMS} \sim 13$–$15\,M_\odot$, whereas we assume systems contributing to the ordinary type Ib/c rate contain at least one star with $M_{\rm ZAMS} \gtrsim 15\,M_\odot$. By integrating the IMF (Kroupa, 2001), we find that systems with late-stage MT constitute $\sim 11\%$ of type Ib/c SN progenitors. Thus we estimate a birth rate for systems that exhibit late-stage MT of $\sim 3 \times 10^{-6}\,{\rm Mpc}^{-3}\,{\rm yr}^{-1}$. To compare to the rates of type Ibn SNe, we note that the ZTF catalog estimates $\sim$10 type Ibn SNe per $\sim$900 CCSNe (Perley et al., 2020). Maeda and Moriya (2022) estimate $\sim 1\%$ of CCSNe are type Ibn SNe, giving a volumetric rate of $\sim 10^{-6}\,{\rm Mpc}^{-3}$,

though these rates may be underestimates since such brief transients can be missed by surveys. Moreover, the calculation above likely overestimates the birth rate, as some massive star binaries may evolve to wide separations where late-stage mass transfer does not occur, and some type Ib/c SNe may originate from merging systems. Thus the birth rate of our progenitor systems appears to be roughly compatible with the type Ibn SN rate.

At the high mass transfer rates seen in all our models, there is a very high degree of Roche lobe overflow that the MESA mass transfer schemes do not capture well. More detailed modeling will be necessary to quantify more accurate late-stage mass transfer rates. Nevertheless, the values presented here are conservative estimates for models where we see the mass transfer rates increasing towards the end of our simulations. Additional sources of angular momentum loss not modeled here will serve only to exacerbate Roche lobe overflow through faster orbital decay. Ultimately, late-stage mass transfer initiated during O/Ne burning will unavoidably lead to extremely high mass transfer rates that can considerably influence the properties of these binary systems in the final years before core collapse.

Acknowledgments

We thank Thomas Tauris for helpful discussion, and Pablo Marchant for guidance in implementing the corrected mass transfer prescription. This material is based upon work supported by the National Science Foundation Graduate Research Fellowship under Grant No. DGE-1745301.

References

Anupama, G. C. et al. (Jan. 2009). "Optical photometry and spectroscopy of the Type Ibn supernova SN 2006jc until the onset of dust formation". In: *MNRAS* 392.2, pp. 894–903. DOI: 10.1111/j.1365-2966.2008.14129.x.

Chatzopoulos, E., J. C. Wheeler, and J. Vinko (Feb. 2012). "Generalized Semi-analytical Models of Supernova Light Curves". In: *ApJ* 746.2, p. 121. DOI: 10.1088/0004-637X/746/2/121.

Chatzopoulos, E. et al. (Aug. 2013). "Analytical Light Curve Models of Superluminous Supernovae: χ^2-minimization of Parameter Fits". In: *ApJ* 773.1, p. 76. DOI: 10.1088/0004-637X/773/1/76.

Clark, P. et al. (Feb. 2020). "LSQ13ddu: a rapidly evolving stripped-envelope supernova with early circumstellar interaction signatures". In: *MNRAS* 492.2, pp. 2208–2228. DOI: 10.1093/mnras/stz3598.

De, K. et al. (Oct. 2018). “A hot and fast ultra-stripped supernova that likely formed a compact neutron star binary”. In: *Science* 362.6411, pp. 201–206. DOI: 10.1126/science.aas8693.

Dessart, L., D. John Hillier, and H. Kuncarayakti (Feb. 2022). “Helium stars exploding in circumstellar material and the origin of Type Ibn supernovae”. In: *A&A* 658, A130. DOI: 10.1051/0004-6361/202142436.

Dewi, J. D. M. and O. R. Pols (Sept. 2003). “The late stages of evolution of helium star-neutron star binaries and the formation of double neutron star systems”. In: *MNRAS* 344.2, pp. 629–643. DOI: 10.1046/j.1365-8711.2003.06844.x.

Eggleton, P. P. (May 1983). “Approximations to the radii of Roche lobes.” In: *ApJ* 268, pp. 368–369. DOI: 10.1086/160960.

Frohmaier, C. et al. (Jan. 2021). “From core collapse to superluminous: the rates of massive stellar explosions from the Palomar Transient Factory”. In: *MNRAS* 500.4, pp. 5142–5158. DOI: 10.1093/mnras/staa3607.

Gal-Yam, A. et al. (Jan. 2022). “A WC/WO star exploding within an expanding carbon-oxygen-neon nebula”. In: *Nature* 601.7892, pp. 201–204. DOI: 10.1038/s41586-021-04155-1.

Gangopadhyay, A. et al. (May 2022). “Evolution of a Peculiar Type Ibn Supernova SN 2019wep”. In: *ApJ* 930.2, p. 127. DOI: 10.3847/1538-4357/ac6187.

Habets, G. M. H. J. (Sept. 1986). “The evolution of a single and a binary helium star of 2.5 solar mass up to neon ignition.” In: *A&A* 165, pp. 95–109.

Habets, G. M. H. J. (Oct. 1986). “The evolution of helium stars in the mass range 2.0 to 4.0 solar masses”. In: *A&A* 167.1, pp. 61–76.

Ho, A. Y. Q. et al. (May 2021). “The Photometric and Spectroscopic Evolution of Rapidly Evolving Extragalactic Transients in ZTF”. In: *arXiv e-prints*, arXiv:2105.08811.

Hubová, D. and O. Pejcha (Oct. 2019). “Kinematics of mass-loss from the outer Lagrange point L2”. In: *MNRAS* 489.1, pp. 891–899. DOI: 10.1093/mnras/stz2208.

Kalogera, V. and R. F. Webbink (Jan. 1998). “Formation of Low-Mass X-Ray Binaries. II. Common Envelope Evolution of Primordial Binaries with Extreme Mass Ratios”. In: *ApJ* 493.1, pp. 351–367. DOI: 10.1086/305085.

Kippenhahn, R., A. Weigert, and A. Weiss (2012). *Stellar Structure and Evolution*. DOI: 10.1007/978-3-642-30304-3.

Kolb, U. and H. Ritter (Sept. 1990). “A comparative study of the evolution of a close binary using a standard and an improved technique for computing mass transfer.” In: *A&A* 236, pp. 385–392.

Kroupa, P. (Apr. 2001). “On the variation of the initial mass function”. In: *MNRAS* 322.2, pp. 231–246. DOI: 10.1046/j.1365-8711.2001.04022.x.

Laplace, E. et al. (May 2020). “The expansion of stripped-envelope stars: Consequences for supernovae and gravitational-wave progenitors”. In: *A&A* 637, A6. DOI: 10.1051/0004-6361/201937300.

Li, W. et al. (Apr. 2011). “Nearby supernova rates from the Lick Observatory Supernova Search - III. The rate-size relation, and the rates as a function of galaxy Hubble type and colour”. In: *MNRAS* 412.3, pp. 1473–1507. DOI: 10.1111/j.1365-2966.2011.18162.x.

Linial, I. and R. Sari (Aug. 2017). “Mass-loss through the L2 Lagrange point - application to main-sequence EMRI”. In: *MNRAS* 469.2, pp. 2441–2454. DOI: 10.1093/mnras/stx1041.

Lu, W. et al. (Apr. 2022). “On rapid binary mass transfer – I. Physical model”. In: *arXiv e-prints*, arXiv:2204.00847.

Maeda, K. and T. J. Moriya (Mar. 2022). “Properties of Type Ibn Supernovae: Implications for the Progenitor Evolution and the Origin of a Population of Rapid Transients”. In: *ApJ* 927.1, p. 25. DOI: 10.3847/1538-4357/ac4672.

Marchant, P. et al. (June 2021). “The role of mass transfer and common envelope evolution in the formation of merging binary black holes”. In: *A&A* 650, A107. DOI: 10.1051/0004-6361/202039992.

Paxton, B. et al. (Jan. 2011). “Modules for Experiments in Stellar Astrophysics (MESA)”. In: *ApJS* 192, p. 3. DOI: 10.1088/0067-0049/192/1/3.

Paxton, B. et al. (Sept. 2013). “Modules for Experiments in Stellar Astrophysics (MESA): Planets, Oscillations, Rotation, and Massive Stars”. In: *ApJS* 208.1, p. 4. DOI: 10.1088/0067-0049/208/1/4.

Paxton, B. et al. (Sept. 2015). “Modules for Experiments in Stellar Astrophysics (MESA): Binaries, Pulsations, and Explosions”. In: *ApJS* 220.1, p. 15. DOI: 10.1088/0067-0049/220/1/15.

Paxton, B. et al. (Feb. 2018). “Modules for Experiments in Stellar Astrophysics (MESA): Convective Boundaries, Element Diffusion, and Massive Star Explosions”. In: *ApJS* 234.2, p. 34. DOI: 10.3847/1538-4365/aaa5a8.

Paxton, B. et al. (July 2019). “Modules for Experiments in Stellar Astrophysics (MESA): Pulsating Variable Stars, Rotation, Convective Boundaries, and Energy Conservation”. In: *ApJS* 243.1, p. 10. DOI: 10.3847/1538-4365/ab2241.

Pejcha, O., B. D. Metzger, and K. Tomida (Sept. 2016). “Binary stellar mergers with marginally bound ejecta: excretion discs, inflated envelopes, outflows, and their luminous transients”. In: *MNRAS* 461.3, pp. 2527–2539. DOI: 10.1093/mnras/stw1481.

Pellegrino, C. et al. (Feb. 2022). “Circumstellar Interaction Powers the Light Curves of Luminous Rapidly Evolving Optical Transients”. In: *ApJ* 926.2, p. 125. DOI: 10.3847/1538-4357/ac3e63.

Pellegrino, C. et al. (May 2022). “The Diverse Properties of Type Icn Supernovae Point to Multiple Progenitor Channels”. In: *arXiv e-prints*, arXiv:2205.07894.

Perley, D. A. et al. (Nov. 2020). “The Zwicky Transient Facility Bright Transient Survey. II. A Public Statistical Sample for Exploring Supernova Demographics”. In: *ApJ* 904.1, p. 35. DOI: 10.3847/1538-4357/abbd98.

Tauris, T. M., N. Langer, and P. Podsiadlowski (Aug. 2015). “Ultra-stripped supernovae: progenitors and fate”. In: *MNRAS* 451.2, pp. 2123–2144. DOI: 10.1093/mnras/stv990.

Tauris, T. M. et al. (Nov. 2013). “Ultra-stripped Type Ic supernovae from close binary evolution”. In: *The Astrophysical Journal* 778.2, p. L23. DOI: 10.1088/2041-8205/778/2/l23.

Verbunt, F. (Jan. 1993). “Origin and evolution of X-ray binaries and binary radio pulsars.” In: *ARA&A* 31, pp. 93–127. DOI: 10.1146/annurev.aa.31.090193.000521.

Yao, Y. et al. (Sept. 2020). “SN2019dge: A Helium-rich Ultra-stripped Envelope Supernova”. In: *ApJ* 900.1, p. 46. DOI: 10.3847/1538-4357/abaa3d.

Yoon, S. .-., S. E. Woosley, and N. Langer (Dec. 2010). “Type Ib/c Supernovae in Binary Systems. I. Evolution and Properties of the Progenitor Stars”. In: *ApJ* 725.1, pp. 940–954. DOI: 10.1088/0004-637X/725/1/940.

Zapartas, E. et al. (June 2017). “Predicting the Presence of Companions for Stripped-envelope Supernovae: The Case of the Broad-lined Type Ic SN 2002ap”. In: *ApJ* 842.2, p. 125. DOI: 10.3847/1538-4357/aa7467.

Zorotovic, M. et al. (Sept. 2010). “Post-common-envelope binaries from SDSS. IX: Constraining the common-envelope efficiency”. en. In: *A&A* 520, A86. ISSN: 0004-6361. DOI: 10.1051/0004-6361/200913658.

Zorotovic, M. and M. R. Schreiber (Apr. 2022). “Close detached white dwarf + brown dwarf binaries: Further evidence for low values of the common envelope efficiency”. In: *MNRAS*, stac1137. ISSN: 0035-8711. DOI: 10.1093/mnras/stac1137.

Chapter 6

FUTURE DIRECTIONS

6.1 Interacting supernovae: wave heating in massive stars

One of the largest sources of uncertainty in the model for wave-driven pre-SN outbursts is the response of the convective envelope to wave energy deposition. Since the envelope's reaction to wave heating directly impacts mass loss and the pre-SN progenitor structure, quantifying this behavior is essential to understanding the subsequent SN attributes and observable pre-SN variation. In addition, wave excitation in the core depends on the evolution of convective shells over time, which for massive stars near core-collapse remains unconstrained. As shells undergo convective mixing and energetic nuclear burning, the wave energy may vary significantly over the last years of stellar evolution (Wu and Fuller, 2021; Wu and Fuller, 2022b). Detailed numerical experiments of wave deposition in the envelope and simulations of evolving shell structures in the core would allow major strides toward clarifying the efficacy of wave-driven pre-SN outbursts. Furthermore, to develop comprehensive models of wave heating across the vast diversity of SN progenitors, we should move towards integrating the thorough analyses enabled by hydrodynamical simulations with 1D stellar evolution models, which are the tools best suited for resolving long-term evolutionary processes.

Efficiency of wave energy deposition in convective stellar envelopes

For the mass range of 10–20 $M_\odot$ stars, our 1D models of wave excitation and propagation have ascertained the magnitude and time dependence of wave energy deposition in the stellar envelope, but face challenges in representing the envelope's response to this additional energy (Wu and Fuller, 2021; Wu and Fuller, 2022b). One fundamental obstacle is that the response of the convective flux to energy deposition is not well understood, which introduces significant uncertainty in the predicted expansion velocity of the perturbed envelope. Moreover, the amplitude evolution of the sound waves as they propagate as weak shocks has not been adequately represented in existing work. The crux of both these issues is the ability to transport wave energy from the base of a massive, extended stellar envelope to the surface, where the binding energy is lower than the scale of wave energy.

The response of convection to wave energy is an inherently dynamical, 3D problem, which our 1D stellar evolution models fall short of describing fully. In 1D wave heating models, I find that rapid wave deposition timescales challenge the equilibrium assumptions of MLT in the convective regions where waves are deposited (Wu and Fuller, 2022b). Simulations of supergiant envelopes have also shown that 3D convective plume structures can open channels for wave energy to reach the surface (Tsang, Kasen, and Bildsten, 2022). To further develop our understanding of how convection realistically responds to energy deposited by waves, one improvement would be to model the wave deposition region at the base of the stellar envelope using time-dependent convection (TDC). This feature has been implemented in MESA and refined over the last few years as an alternative formulation of convection. Unlike MLT, TDC allows MESA to model convection on timescales short enough that properties such as the convective velocity and flux are varying. This is the case for wave deposition regions, where an influx of wave power likely accelerates local convective plumes. Furthermore, 3D hydrodynamical simulations of energy deposition in a convective region could help determine how much wave energy we expect to be carried by the convective flux and how much energy goes into accelerating the expansion of the stellar envelope.

In addition to the behavior of the convective flux, the problem of wave energy deposition in a stellar envelope hinges upon the dynamical evolution of the wave amplitude as multiple acoustic waves exit the core throughout the late burning phases of the star. Since the density drops steeply outside the core, waves are expected to form weak shocks near the base of the stellar envelope, after which they must propagate through the envelope towards the surface. Weak shock damping in stellar envelopes has been implemented analytically in models, but they so far indicate that weak shocks are not able to sustain their amplitudes until the stellar surface (Wu and Fuller, 2022b). Nevertheless, hydrodynamical studies of weak shocks indicate that the energy scales we find in Wu and Fuller, 2021; Wu and Fuller, 2022b are capable of producing mass loss when a weak shock transitions to a strong shock near the stellar surface (Linial, Fuller, and Sari, 2021). Wave heating also proceeds continuously so that a train of weak shocks is transmitted into the envelope, but the dynamics of multiple shocks interacting has been omitted thus far. As successive shocks propagate, they may alter the entropy and thus the background sound speed, which will cause the acoustic wave speeds to vary. Collisions between waves of different speeds may build up wave amplitudes, potentially allowing weak shocks to survive out to larger radii. Through more advanced simulations that

resolve interactions among a train of weak shocks, we hope to establish in the future whether weak shocks can strengthen in the stellar envelope. If weak shocks do steepen significantly near the surface of the star, they may deposit enough energy to potentially eject mass and explain the population of luminous pre-SN outbursts.

To summarize, future research on the wave heating model to produce pre-SN outbursts should focus on ascertaining whether the available wave energy generated in the core can be efficiently transported to the surface. Given high enough energies and efficient deposition of wave energy in the envelope, waves may unbind 0.01–1 $M_\odot$ of material and explain luminous outbursts from hydrogen-rich type IIn SNe (Fuller, 2017; Linial, Fuller, and Sari, 2021; Strotjohann et al., 2021). In stripped stars that only retain a diffuse hydrogen or perhaps helium envelope due to previous episodes of binary mass transfer, wave heating that successfully ejects CSM will address observations of type IIb or type Ibn SNe (Gal-Yam et al., 2014; Hosseinzadeh et al., 2017; Fuller and Ro, 2018).

Core convective boundary mixing in massive stars

Another crucial, yet unconstrained, aspect of the wave heating model relates to the generation of waves by core convection. The behavior of convective shells in the cores of massive stars is governed by intense nuclear fusion that occurs in layers of different abundances. As the burning proceeds, convective shells may extend beyond their initial boundaries through overshoot processes and mix into layers of different composition. Shell mergers may ensue, igniting fresh nuclear reactions in the affected shells and increasing convective shell widths. These changes in the convective shell properties greatly impact the nature of the convectively excited waves that underlie wave-driven pre-SN outbursts.

Though similar shell mergers have been observed in several 1D stellar evolution studies (Wu and Fuller, 2021; Laplace et al., 2021) and 3D simulations (Collins, Müller, and Heger, 2018; Andrassy et al., 2020; Yadav et al., 2020), uncertainties in the treatment of convective overshoot in 1D models using mixing-length theory (MLT) limit our ability to derive robust predictions for the properties of the shells near core-collapse. Formulations of overshoot in conjunction with MLT assume convection to be in equilibrium, but late-stage nuclear burning proceeds so quickly that entrainment is not equilibrated on such short timescales in 3D simulations (Collins, Müller, and Heger, 2018). This implies that MLT imposes inaccurate composition profiles during these phases. In addition, the functional form of 1D

overshoot prescriptions in most MESA models of massive stars have rarely been motivated by observations or 3D hydrodynamical simulations.

Available constraints on the form of convective overshoot have recently been inferred from asteroseismic observations of massive main-sequence stars (Pedersen et al., 2018; Pedersen et al., 2021; Pedersen, 2022), and simulations of a two-layer radiative and convective domain have clarified the physical conditions for overshoot in main-sequence stars (Anders et al., 2022). These studies provide prescriptions that can be readily implemented in MESA. However, there has yet to be a study appropriate for massive stellar cores near core-collapse, which contain complicated shell structures with alternating layers of radiative and convective zones, composition gradients that may have a stabilizing effect on mixing, and strong temperature fluxes. The convective fluxes are correspondingly large during this time period, which is promising for generating energetic waves, but the uncertainty in how the convective shells evolve introduces major difficulties in making concrete predictions for how much wave energy should actually escape the core.

In the pursuit of more accurate models of convective shells in massive stars, different types of convective boundary mixing come into consideration. Anders et al., 2022 examine overshoot in the form of convective penetration, which describes the mixing of the entropy gradient in a Schwarzschild-stable region by convective motions. Erosion of the convective boundary can also proceed through entrainment (Meakin and Arnett, 2007b; Rizzuti et al., 2023). To capture the conditions for shell mergers in 1D stellar evolution models, we would like to enhance our understanding of these convective boundary mixing processes to the point where we can formulate physically motivated overshoot prescriptions in stellar evolution models.

Vigorous convective boundary mixing is anticipated to affect shell widths, nucleosynthetic reactions, and wave luminosities. For example, we observe in Wu and Fuller (2021) that convective mixing widens the helium shell, driving vigorous alpha capture reactions as helium is mixed downward that increases the convective flux and thus the wave power. This behavior recurs throughout $\gtrsim 30\,M_\odot$ progenitors, thereby producing energetic waves that could transmit up to 10^{48} erg into the stellar envelope. At such high energy scales, previous studies find that waves can accelerate ~ 0.1–$1\,M_\odot$ of material to 100 km/s in supergiants and even unbind $0.1\,M_\odot$ in hydrogen-poor progenitors (Fuller, 2017; Fuller and Ro, 2018). It is important to evaluate whether realistic mixing corroborates the prevalence of the shell merger phenomenon, or whether it only rarely causes convective shells to merge. If the

latter, more pessimistic, prediction prevails, the wave heating mechanism may operate less efficiently in $\gtrsim 30\,M_\odot$ progenitors than predicted in Wu and Fuller, 2021. Yet if the cores of massive stars prove to be conducive environments for convective mixing to produce shell mergers, the ensuing waves excited can potentially facilitate luminous pre-SN outbursts in $\gtrsim 30\,M_\odot$ progenitors.

6.2 Interacting supernovae: binary interaction

Observed interacting SNe show substantial diversity in the inferred duration of interaction, CSM mass, composition, and velocities. Among the potential mechanisms to produce CSM in interacting SNe, pre-SN binary evolution has strong theoretical potential to address the issue, as the various outcomes that proceed from the huge variety of initial conditions in binary evolution likely span the observed range in these outburst properties. Stellar expansion may be triggered by core contraction at the end of a nuclear burning phase (Laplace et al., 2020; Wu and Fuller, 2022a), or internal energy deposition such as from waves excited by core convection during vigorous nuclear burning (Wu and Fuller, 2022b; Fuller, 2017; Fuller and Ro, 2018). Thus, mass transfer in binaries is expected given a nearby companion and naturally associated with the timescales of nuclear burning phases. The timing and amount of mass loss depends on the binary separation and the initial masses of the binary. For instance, lower mass stars will expand more than higher mass stars, and the amount of hydrogen envelope left over from previous mass transfer phases will also influence the maximum radial extent (Laplace et al., 2020). Systematic studies to investigate when mass transfer leads to timely outbursts could provide direct connections between this promising theory for pre-SN mass loss and the multitude of observed interacting SNe.

Bright SN precursors, observed as optical flares months to years before core collapse, are often linked to the production of the dense CSM detected in interacting supernovae (Pastorello et al., 2007; Margutti et al., 2014; Strotjohann et al., 2021). With luminosities of 10^{40}–10^{42} erg/s, the precursors exceed the Eddington limit of massive stars by many orders of magnitude. This prediction is difficult to reproduce with single-star evolution, as it is unclear what mechanism can drive such a powerful outburst. Recent work has shown that super-Eddington accretion onto and subsequent outflows from a compact companion can enhance the luminosity of outbursts from red supergiants and stripped stars (Tsuna et al., 2024). By appealing to the binary scenario, this study is able to match the brightness of observed precursors for both type IIn and type Ibn SNe (Tsuna et al., 2024).

The vast parameter space is daunting to cover. It is important to examine, among other things, a variety of binary mass ratios, which relates strongly to the orbital angular momentum and mass transfer stability; a range of initial helium core masses, which determine the timing and extent of expansion; and different initial orbital separations. Furthermore, the details of the binary stellar evolution cannot be omitted as in parametric binary population synthesis codes, which succeed at exploring parameter space at the expense of incorporating the relevant interior physics for stars in binaries. Strides towards accommodating both detailed binary evolution and the flexibility of parametric binary population synthesis are underway (Fragos et al., 2023), which hopefully will extend to later evolutionary stages in the future. Moving in this direction will promote future investigations into the flexibility of the binary evolution scenario towards interpreting diverse observations of interacting SNe.

6.3 Shaping planetary orbital architectures with tidal dissipation

The methods introduced in Chapter 2 allow us to compute the frequency-dependent dissipation of normal modes in realistic stellar structures self-consistently throughout the system evolution. In the future, I plan to apply these methods to partially convective stars $\gtrsim 0.5\,M_\odot$. Compared to low-mass fully convective stars, not only the i-modes, but also the g-modes in these higher-mass stars contribute a dense spectrum of resonant frequencies. With our methods, we are poised to produce the first coupled stellar and planetary orbital evolution calculations that use the full frequency-dependent spectrum of tidally excited gravito-inertial and i-modes. With these calculations in hand, we would be able to address how dynamical tidal dissipation in FGKM stars influences migration of hot Jupiters. Hot Jupiters, found on short-period ($\lesssim 10$ day) orbits, are younger than average field stars (Hamer and Schlaufman, 2019), evidencing plunge-in and destruction of the planets on short timescales. Furthermore, the orbits of planets such as WASP-12b are observed to decay rapidly with measured $Q \sim 2 \times 10^5$ (Maciejewski et al., 2016; Yee et al., 2020), which is too small to be explained by equilibrium tides. Instead, such rapid migration may occur because of nonlinear wave breaking from internal stellar oscillations (Weinberg et al., 2017). In anticipation of future similar detections, models of dynamical tidal dissipation are important components to understanding some of the most extreme exoplanet systems.

In addition to inducing tidal migration, tidal dissipation in the star may lead to alignment between the star's spin and planet's orbit. Rossiter-McLaughlin measure-

ments of the projected obliquity between the vectors of stellar spin and planetary orbital angular momentum reveal a dichotomy across FGK stars hosting hot Jupiters (Albrecht et al., 2012; Albrecht et al., 2021; Winn et al., 2010; Winn et al., 2017; Spalding and Winn, 2022). A transition from aligned systems to systems with a large spread of obliquities occurs at effective temperature $T_{\rm eff} \sim 6100$K, coinciding with the Kraft break between cooler G/K stars with convective envelopes and hotter F stars with mostly radiative envelopes. If hot Jupiters form with a range of obliquities, then to explain the observations they must realign by a mechanism which acts more efficiently in G/K stars. Yet in lower-mass M-dwarfs with larger convective envelopes, the obliquity trend may indeed reverse: for the two M-dwarf systems with an obliquity measurement, the less massive planet GJ 436 with $M \approx 0.4\,M_\odot$ is highly misaligned, while the more massive Kepler-45b with $M \approx 0.6\,M_\odot$ is aligned (Bourrier et al., 2018; Dai et al., 2018). Dynamical tidal dissipation has been proposed to explain the misalignment trend across FGKM stars (Lai, 2012; Lin and Ogilvie, 2017; Spalding and Winn, 2022), but most existing studies face shortcomings: either tidal dissipation is treated via frequency-independent parameterizations, or sophisticated calculations of tidal dissipation are performed in isolation from the full stellar and orbital evolution. Another future goal is to apply our methods towards this question of obliquity in star-planet systems as well (see also recent work by Zanazzi, Dewberry, and Chiang, 2024).

6.4 Connection to ongoing and future missions

The Astro2020 Decadal survey identified probing the nature of stellar explosions and understanding the connections between stars and the planets they host as key scientific challenges in the next decade (National Academies of Sciences and Medicine, 2023). Through the launches of new telescopes in the next decade, these priority areas will be supported through ambitious surveys of the night sky. The Vera Rubin Observatory will conduct the Legacy Survey of Space and Time (LSST) in the southern hemisphere over ten years, imaging the entire visible sky every 3–4 nights. Out of the millions of type II SNe and over five hundred thousand type Ibc SNe that LSST is anticipated to discover, thousands will be nearby enough to conduct more detailed photometric analyses that can be used to constrain the ejecta properties and capture CSM late-onset interaction (Dessart et al., 2022). In 2030, UVEX, the new NASA mission to explore the ultraviolet sky, will be able to detect far more early emission lines than current optical spectroscopic observations. These UV spectra, obtained as soon as 3 hours after a supernova event trigger, will reveal the kine-

matic evolution and chemical composition of shocked CSM around core-collapse supernovae. In addition, the currently operational James Webb Space Telescope (JWST) will execute programs investigating potential outbursts and mass loss from red supergiants (RSGs) through efforts to study dusty RSGs and SNe. Towards the goal of understanding planetary population statistics, the Nancy Grace Roman Space Telescope will use microlensing, direct imaging, and transit techniques to compile a census of exoplanets in our galaxy, extending the stream of discoveries already made by TESS, Kepler/K2, and ground-based telescopes. As these undertakings amass a wealth of data that paint an ever more detailed picture of the dynamic universe, they inspire new, fascinating questions to answer and give material purpose to our theoretical models of stellar evolution and oscillations. It is a privilege to work as a theoretical astrophysicist amidst the advent of these pioneering missions.

BIBLIOGRAPHY

Agüeros, M. A. et al. (Oct. 2011). "The Factory and the Beehive. I. Rotation Periods for Low-mass Stars in Praesepe". In: *ApJ* 740.2, p. 110. DOI: 10.1088/0004-637X/740/2/110.

Albrecht, S. et al. (Sept. 2012). "Obliquities of Hot Jupiter Host Stars: Evidence for Tidal Interactions and Primordial Misalignments". In: *ApJ* 757.1, p. 18. DOI: 10.1088/0004-637X/757/1/18.

Albrecht, S. H. et al. (July 2021). "A Preponderance of Perpendicular Planets". In: *ApJL* 916.1, p. L1. DOI: 10.3847/2041-8213/ac0f03.

Anders, E. H. et al. (Feb. 2022). "Stellar Convective Penetration: Parameterized Theory and Dynamical Simulations". In: *The Astrophysical Journal* 926.2, p. 169. DOI: 10.3847/1538-4357/ac408d.

Andrassy, R. et al. (Jan. 2020). "3D hydrodynamic simulations of C ingestion into a convective O shell". In: *MNRAS* 491.1, pp. 972–992. DOI: 10.1093/mnras/stz2952.

Arnett, W. D. and C. Meakin (June 2011). "Toward Realistic Progenitors of Core-collapse Supernovae". In: *ApJ* 733.2, p. 78. DOI: 10.1088/0004-637X/733/2/78.

El-Badry, K. et al. (Dec. 2022). "Magnetic braking saturates: evidence from the orbital period distribution of low-mass detached eclipsing binaries from ZTF". In: *MNRAS* 517.4, pp. 4916–4939. DOI: 10.1093/mnras/stac2945.

Blagorodnova, N. et al. (Jan. 2017). "Common Envelope Ejection for a Luminous Red Nova in M101". In: *ApJ* 834.2, p. 107. DOI: 10.3847/1538-4357/834/2/107.

Boccioli, L. et al. (May 2023). "Explosion Mechanism of Core-collapse Supernovae: Role of the Si/Si-O Interface". In: *ApJ* 949.1, p. 17. DOI: 10.3847/1538-4357/acc06a.

Bourrier, V. et al. (Jan. 2018). "Orbital misalignment of the Neptune-mass exoplanet GJ 436b with the spin of its cool star". In: *Nature* 553.7689, pp. 477–480. DOI: 10.1038/nature24677.

Castor, J. I., D. C. Abbott, and R. I. Klein (Jan. 1975). "Radiation-driven winds in Of stars." In: *ApJ* 195, pp. 157–174. DOI: 10.1086/153315.

Christensen-Dalsgaard, J. (May 2003). *Lecture Notes on Stellar Oscillations*. https://users-phys.au.dk/jcd/oscilnotes/.

Christensen-Dalsgaard, J. (Feb. 2016). "Asteroseismology with solar-like oscillations". In: *arXiv e-prints*, arXiv:1602.06838.

Collins, C., B. Müller, and A. Heger (Jan. 2018). "Properties of convective oxygen and silicon burning shells in supernova progenitors". In: *MNRAS* 473.2, pp. 1695–1704. DOI: 10.1093/mnras/stx2470.

Dai, F. et al. (Apr. 2018). "Stellar Obliquity and Magnetic Activity of Planet-hosting Stars and Eclipsing Binaries Based on Transit Chord Correlation". In: *AJ* 155.4, p. 177. DOI: 10.3847/1538-3881/aab618.

Dawson, R. I. and J. A. Johnson (Sept. 2018). "Origins of Hot Jupiters". In: *ARA&A* 56, pp. 175–221. DOI: 10.1146/annurev-astro-081817-051853.

de Mink, S. E. et al. (Feb. 2014). "The Incidence of Stellar Mergers and Mass Gainers among Massive Stars". In: *ApJ* 782.1, p. 7. DOI: 10.1088/0004-637X/782/1/7.

Dessart, L. et al. (Oct. 2022). "Using LSST late-time photometry to constrain Type Ibc supernovae and their progenitors". In: *A&A* 666, p. L14. DOI: 10.1051/0004-6361/202244413.

Dewi, J. D. M. and O. R. Pols (Sept. 2003). "The late stages of evolution of helium star-neutron star binaries and the formation of double neutron star systems". In: *MNRAS* 344.2, pp. 629–643. DOI: 10.1046/j.1365-8711.2003.06844.x.

Donati, J. .-. and J. D. Landstreet (Sept. 2009). "Magnetic Fields of Nondegenerate Stars". In: *ARA&A* 47.1, pp. 333–370. DOI: 10.1146/annurev-astro-082708-101833.

Ebinger, K. et al. (Jan. 2019). "PUSHing Core-collapse Supernovae to Explosions in Spherical Symmetry. II. Explodability and Remnant Properties". In: *ApJ* 870.1, p. 1. DOI: 10.3847/1538-4357/aae7c9.

Fragos, T. et al. (Feb. 2023). "POSYDON: A General-purpose Population Synthesis Code with Detailed Binary-evolution Simulations". In: *ApJS* 264.2, p. 45. DOI: 10.3847/1538-4365/ac90c1.

Fuller, J. (Sept. 2017). "Pre-supernova outbursts via wave heating in massive stars - I. Red supergiants". In: *MNRAS* 470.2, pp. 1642–1656. DOI: 10.1093/mnras/stx1314.

Fuller, J. and S. Ro (May 2018). "Pre-supernova outbursts via wave heating in massive stars - II. Hydrogen-poor stars". In: *MNRAS* 476.2, pp. 1853–1868. DOI: 10.1093/mnras/sty369.

Gal-Yam, A. et al. (Jan. 2022). "A WC/WO star exploding within an expanding carbon-oxygen-neon nebula". In: *Nature* 601.7892, pp. 201–204. DOI: 10.1038/s41586-021-04155-1.

Gal-Yam, A. et al. (May 2014). "A Wolf-Rayet-like progenitor of SN 2013cu from spectral observations of a stellar wind". In: *Nature* 509.7501, pp. 471–474. DOI: 10.1038/nature13304.

Goldreich, P. and P. D. Nicholson (July 1989). "Tidal Friction in Early-Type Stars". In: *ApJ* 342, p. 1079. DOI: 10.1086/167665.

Habets, G. M. H. J. (Oct. 1986). "The evolution of helium stars in the mass range 2.0 to 4.0 solar masses". In: *A&A* 167.1, pp. 61–76.

Hamer, J. H. and K. C. Schlaufman (Nov. 2019). "Hot Jupiters Are Destroyed by Tides While Their Host Stars Are on the Main Sequence". In: *AJ* 158.5, p. 190. DOI: 10.3847/1538-3881/ab3c56.

Hansen, C. J., S. D. Kawaler, and V. Trimble (2004). *Stellar interiors : physical principles, structure, and evolution*.

Hosseinzadeh, G. et al. (Feb. 2017). "Type Ibn Supernovae Show Photometric Homogeneity and Spectral Diversity at Maximum Light". In: *ApJ* 836.2, p. 158. DOI: 10.3847/1538-4357/836/2/158.

Ivanova, N. et al. (Feb. 2013). "Common envelope evolution: where we stand and how we can move forward". In: *A&A Rv* 21, p. 59. DOI: 10.1007/s00159-013-0059-2.

Jacobson-Galán, W. V. et al. (Mar. 2024). "Final Moments II: Observational Properties and Physical Modeling of CSM-Interacting Type II Supernovae". In: *arXiv e-prints*, arXiv:2403.02382. DOI: 10.48550/arXiv.2403.02382.

Justham, S., P. Podsiadlowski, and J. S. Vink (Dec. 2014). "Luminous Blue Variables and Superluminous Supernovae from Binary Mergers". In: *ApJ* 796.2, p. 121. DOI: 10.1088/0004-637X/796/2/121.

Kasliwal, M. M. et al. (Apr. 2017). "SPIRITS: Uncovering Unusual Infrared Transients with Spitzer". In: *ApJ* 839.2, p. 88. DOI: 10.3847/1538-4357/aa6978.

Kawaler, S. D. (Dec. 1987). "Angular momentum in stars - The Kraft curve revisited". In: *Publications of the Astronomical Society of the Pacific* 99, pp. 1322–1228. DOI: 10.1086/132120.

Kippenhahn, R., A. Weigert, and A. Weiss (2013). *Stellar Structure and Evolution*. DOI: 10.1007/978-3-642-30304-3.

Kudritzki, R.-P. and J. Puls (Jan. 2000). "Winds from Hot Stars". In: *ARA&A* 38, pp. 613–666. DOI: 10.1146/annurev.astro.38.1.613.

Lai, D. (June 2012). "Tidal dissipation in planet-hosting stars: damping of spin-orbit misalignment and survival of hot Jupiters". In: *MNRAS* 423.1, pp. 486–492. DOI: 10.1111/j.1365-2966.2012.20893.x.

Laplace, E. et al. (May 2020). "The expansion of stripped-envelope stars: Consequences for supernovae and gravitational-wave progenitors". In: *A&A* 637, A6. DOI: 10.1051/0004-6361/201937300.

Laplace, E. et al. (Dec. 2021). "Different to the core: The pre-supernova structures of massive single and binary-stripped stars". In: *A&A* 656, A58. DOI: 10.1051/0004-6361/202140506.

Lin, Y. and G. I. Ogilvie (June 2017). "Tidal interactions in spin-orbit misaligned systems". In: *MNRAS* 468.2, pp. 1387–1397. DOI: 10.1093/mnras/stx540.

Linial, I., J. Fuller, and R. Sari (Mar. 2021). "Partial stellar explosions - ejected mass and minimal energy". In: *MNRAS* 501.3, pp. 4266–4275. DOI: 10.1093/mnras/staa3969.

Lucy, L. B. and P. M. Solomon (Mar. 1970). "Mass Loss by Hot Stars". In: *ApJ* 159, p. 879. DOI: 10.1086/150365.

Maciejewski, G. et al. (Apr. 2016). "Departure from the constant-period ephemeris for the transiting exoplanet WASP-12". In: *A&A* 588, p. L6. DOI: 10.1051/0004-6361/201628312.

MacLeod, M. et al. (Feb. 2017). "Lessons from the Onset of a Common Envelope Episode: the Remarkable M31 2015 Luminous Red Nova Outburst". In: *ApJ* 835.2, p. 282. DOI: 10.3847/1538-4357/835/2/282.

Margutti, R. et al. (Jan. 2014). "A Panchromatic View of the Restless SN 2009ip Reveals the Explosive Ejection of a Massive Star Envelope". In: *ApJ* 780.1, p. 21. DOI: 10.1088/0004-637X/780/1/21.

Mathis, S. (Nov. 2009). "Transport by gravito-inertial waves in differentially rotating stellar radiation zones. I - Theoretical formulation". In: *A&A* 506.2, pp. 811–828. DOI: 10.1051/0004-6361/200810544.

Mathys, G. (Jan. 2001). "Magnetic Fields of Ap and Bp Stars". In: *Magnetic Fields Across the Hertzsprung-Russell Diagram*. Ed. by G. Mathys, S. K. Solanki, and D. T. Wickramasinghe. Vol. 248. Astronomical Society of the Pacific Conference Series, p. 267.

Matt, S. P. et al. (Jan. 2015). "The Mass-dependence of Angular Momentum Evolution in Sun-like Stars". In: *ApJL* 799.2, p. L23. DOI: 10.1088/2041-8205/799/2/L23.

Meakin, C. A. and D. Arnett (Jan. 2006). "Active Carbon and Oxygen Shell Burning Hydrodynamics". In: *ApJL* 637.1, pp. L53–L56. DOI: 10.1086/500544.

Meakin, C. A. and D. Arnett (Aug. 2007). "Anelastic and Compressible Simulations of Stellar Oxygen Burning". In: *ApJ* 665.1, pp. 690–697. DOI: 10.1086/519372.

Meakin, C. A. and D. Arnett (Sept. 2007). "Turbulent Convection in Stellar Interiors. I. Hydrodynamic Simulation". In: *ApJ* 667.1, pp. 448–475. DOI: 10.1086/520318.

Metzger, B. D. and O. Pejcha (Nov. 2017). "Shock-powered light curves of luminous red novae as signatures of pre-dynamical mass-loss in stellar mergers". In: *MNRAS* 471.3, pp. 3200–3211. DOI: 10.1093/mnras/stx1768.

Moe, M. and R. Di Stefano (June 2017). "Mind Your Ps and Qs: The Interrelation between Period (P) and Mass-ratio (Q) Distributions of Binary Stars". In: *ApJS* 230.2, p. 15. DOI: 10.3847/1538-4365/aa6fb6.

Moriya, T. J. and N. Langer (Jan. 2015). "Pulsations of red supergiant pair-instability supernova progenitors leading to extreme mass loss". In: *A&A* 573, A18. DOI: 10.1051/0004-6361/201424957.

Morton, D. C. (July 1960). "Evolutionary Mass Exchange in Close Binary Systems." In: *ApJ* 132, p. 146. DOI: 10.1086/146908.

Morton, D. C. (Nov. 1967). "Mass Loss from Three OB Supergiants in Orion". In: *ApJ* 150, p. 535. DOI: 10.1086/149356.

Moss, D. (Jan. 2001). "Magnetic Fields in the Ap and Bp Stars: a Theoretical Overview". In: *Magnetic Fields Across the Hertzsprung-Russell Diagram*. Ed. by G. Mathys, S. K. Solanki, and D. T. Wickramasinghe. Vol. 248. Astronomical Society of the Pacific Conference Series, p. 305.

National Academies of Sciences, E. and Medicine (2023). *Pathways to Discovery in Astronomy and Astrophysics for the 2020s*. Washington, DC: The National Academies Press. ISBN: 978-0-309-46734-6. DOI: 10.17226/26141.

Ogilvie, G. I. (Aug. 2014). "Tidal Dissipation in Stars and Giant Planets". In: *ARA&A* 52, pp. 171–210. DOI: 10.1146/annurev-astro-081913-035941.

Owocki, S. P., J. I. Castor, and G. B. Rybicki (Dec. 1988). "Time-dependent Models of Radiatively Driven Stellar Winds. I. Nonlinear Evolution of Instabilities for a Pure Absorption Model". In: *ApJ* 335, p. 914. DOI: 10.1086/166977.

Pastorello, A. et al. (June 2007). "A giant outburst two years before the core-collapse of a massive star". In: *Nature* 447.7146, pp. 829–832. DOI: 10.1038/nature05825.

Pedersen, M. G. et al. (July 2018). "The shape of convective core overshooting from gravity-mode period spacings". In: *A&A* 614, A128. DOI: 10.1051/0004-6361/201732317.

Pedersen, M. G. (May 2022). "On the Diversity of Mixing and Helium Core Masses of B-type Dwarfs from Gravity-mode Asteroseismology". In: *ApJ* 930.1, p. 94. DOI: 10.3847/1538-4357/ac5b05.

Pedersen, M. G. et al. (Jan. 2021). "Internal mixing of rotating stars inferred from dipole gravity modes". In: *Nature Astronomy* 5, pp. 715–722. DOI: 10.1038/s41550-021-01351-x.

Pellegrino, C. et al. (May 2022). "The Diverse Properties of Type Icn Supernovae Point to Multiple Progenitor Channels". In: *arXiv e-prints*, arXiv:2205.07894.

Perley, D. A. et al. (Nov. 2020). "The Zwicky Transient Facility Bright Transient Survey. II. A Public Statistical Sample for Exploring Supernova Demographics". In: *ApJ* 904.1, p. 35. DOI: 10.3847/1538-4357/abbd98.

Podsiadlowski, P., P. C. Joss, and J. J. L. Hsu (May 1992). "Presupernova Evolution in Massive Interacting Binaries". In: *ApJ* 391, p. 246. DOI: 10.1086/171341.

Podsiadlowski, P., T. S. Morris, and N. Ivanova (Dec. 2006). "Massive Binary Mergers: A Unique Scenario for the sgB[e] Phenomenon?" In: *Stars with the B[e] Phenomenon*. Ed. by M. Kraus and A. S. Miroshnichenko. Vol. 355. Astronomical Society of the Pacific Conference Series, p. 259.

Postnov, K. A. and L. R. Yungelson (May 2014). "The Evolution of Compact Binary Star Systems". In: *Living Reviews in Relativity* 17.1, p. 3. DOI: 10.12942/lrr-2014-3.

Press, W. H. and S. A. Teukolsky (Apr. 1977). "On formation of close binaries by two-body tidal capture." In: *ApJ* 213, pp. 183–192. DOI: 10.1086/155143.

Quataert, E. and J. Shiode (June 2012). "Wave-driven mass loss in the last year of stellar evolution: setting the stage for the most luminous core-collapse supernovae". In: *MNRAS* 423.1, pp. L92–L96. DOI: 10.1111/j.1745-3933.2012.01264.x.

Rizzuti, F. et al. (Aug. 2023). "3D stellar evolution: hydrodynamic simulations of a complete burning phase in a massive star". In: *MNRAS* 523.2, pp. 2317–2328. DOI: 10.1093/mnras/stad1572.

Rodríguez-Ledesma, M. V., R. Mundt, and J. Eislöffel (Aug. 2009). "Rotational studies in the Orion Nebula Cluster: from solar mass stars to brown dwarfs". In: *A&A* 502.3, pp. 883–904. DOI: 10.1051/0004-6361/200811427.

Sana, H. et al. (July 2012). "Binary Interaction Dominates the Evolution of Massive Stars". In: *Science* 337.6093, p. 444. DOI: 10.1126/science.1223344.

Schou, J. et al. (Sept. 1998). "Helioseismic Studies of Differential Rotation in the Solar Envelope by the Solar Oscillations Investigation Using the Michelson Doppler Imager". In: *ApJ* 505.1, pp. 390–417. DOI: 10.1086/306146.

Shiode, J. H. and E. Quataert (Jan. 2014). "Setting the Stage for Circumstellar Interaction in Core-Collapse Supernovae. II. Wave-driven Mass Loss in Supernova Progenitors". In: *ApJ* 780.1, p. 96. DOI: 10.1088/0004-637X/780/1/96.

Skumanich, A. (Feb. 1972). "Time Scales for Ca II Emission Decay, Rotational Braking, and Lithium Depletion". In: *ApJ* 171, p. 565. DOI: 10.1086/151310.

Smith, N. (2017). "Interacting Supernovae: Types IIn and Ibn". In: *Handbook of Supernovae*, p. 403. DOI: 10.1007/978-3-319-21846-5_38.

Spalding, C. and J. N. Winn (Mar. 2022). "Tidal Erasure of Stellar Obliquities Constrains the Timing of Hot Jupiter Formation". In: *ApJ* 927.1, p. 22. DOI: 10.3847/1538-4357/ac4993.

Strotjohann, N. L. et al. (Feb. 2021). "Bright, Months-long Stellar Outbursts Announce the Explosion of Interaction-powered Supernovae". In: *ApJ* 907.2, p. 99. DOI: 10.3847/1538-4357/abd032.

Tauris, T. M. et al. (Sept. 2017). "Formation of Double Neutron Star Systems". In: *ApJ* 846.2, p. 170. DOI: 10.3847/1538-4357/aa7e89.

Tsang, B. T., D. Kasen, and L. Bildsten (Sept. 2022). "3D Hydrodynamics of Pre-supernova Outbursts in Convective Red Supergiant Envelopes". In: *ApJ* 936.1, p. 28. DOI: 10.3847/1538-4357/ac83bc.

Tsuna, D. et al. (Jan. 2024). "Bright Supernova Precursors by Outbursts from Massive Stars with Compact Object Companions". In: *arXiv e-prints*, arXiv:2401.02389. DOI: 10.48550/arXiv.2401.02389.

Vidotto, A. A. et al. (July 2014). "Stellar magnetism: empirical trends with age and rotation". In: *MNRAS* 441.3, pp. 2361–2374. DOI: 10.1093/mnras/stu728.

Webbink, R. F. (Jan. 1979). "The Formation of White Dwarfs in Close Binary Systems". In: *IAU Colloq. 53: White Dwarfs and Variable Degenerate Stars*. Ed. by H. M. van Horn, V. Weidemann, and M. P. Savedoff, p. 426.

Weinberg, N. N. et al. (Nov. 2017). "Tidal Dissipation in WASP-12". In: *ApJL* 849.1, p. L11. DOI: 10.3847/2041-8213/aa9113.

Winn, J. N. et al. (Aug. 2010). "Hot Stars with Hot Jupiters Have High Obliquities". In: *ApJL* 718.2, pp. L145–L149. DOI: 10.1088/2041-8205/718/2/L145.

Winn, J. N. et al. (Dec. 2017). "Constraints on the Obliquities of Kepler Planet-hosting Stars". In: *AJ* 154.6, p. 270. DOI: 10.3847/1538-3881/aa93e3.

Witte, M. G. and G. J. Savonije (Jan. 1999). "The dynamical tide in a rotating 10 solar mass main sequence star. A study of g- and r-mode resonances". In: *A&A* 341, pp. 842–852.

Witte, M. G. and G. J. Savonije (Oct. 1999). "Tidal evolution of eccentric orbits in massive binary systems. A study of resonance locking". In: *A&A* 350, pp. 129–147. DOI: 10.48550/arXiv.astro-ph/9909073.

Woosley, S. E. and A. Heger (Sept. 2015). "The Remarkable Deaths of 9-11 Solar Mass Stars". In: *ApJ* 810.1, p. 34. DOI: 10.1088/0004-637X/810/1/34.

Wu, S. C. and J. Fuller (Jan. 2021). "A Diversity of Wave-driven Presupernova Outbursts". In: *The Astrophysical Journal* 906.1, p. 3. DOI: 10.3847/1538-4357/abc87c.

Wu, S. C. and J. Fuller (Nov. 2022). "Extreme Mass Loss in Low-mass Type Ib/c Supernova Progenitors". In: *The Astrophysical Journal, Letters* 940.1, p. L27. DOI: 10.3847/2041-8213/ac9b3d.

Wu, S. C. and J. Fuller (May 2022). "Wave-driven Outbursts and Variability of Low-mass Supernova Progenitors". In: *The Astrophysical Journal* 930.2, p. 119. DOI: 10.3847/1538-4357/ac660c.

Yadav, N. et al. (Feb. 2020). "Large-scale Mixing in a Violent Oxygen-Neon Shell Merger Prior to a Core-collapse Supernova". In: *ApJ* 890.2, p. 94. DOI: 10.3847/1538-4357/ab66bb.

Yee, S. W. et al. (Jan. 2020). "The Orbit of WASP-12b Is Decaying". In: *ApJL* 888.1, p. L5. DOI: 10.3847/2041-8213/ab5c16.

Yoon, S. .-., S. E. Woosley, and N. Langer (Dec. 2010). “Type Ib/c Supernovae in Binary Systems. I. Evolution and Properties of the Progenitor Stars”. In: *ApJ* 725.1, pp. 940–954. DOI: 10.1088/0004-637X/725/1/940.

Zahn, J. P. (Feb. 1966). “Les marées dans une étoile double serrée”. In: *Annales d’Astrophysique* 29, p. 313.

Zanazzi, J. J., J. Dewberry, and E. Chiang (Mar. 2024). “Damping Obliquities of Hot Jupiter Hosts by Resonance Locking”. In: *arXiv e-prints*, arXiv:2403.05616. DOI: 10.48550/arXiv.2403.05616.